Volume 120, October 2017

ISSN 0927-796X

ELSEVIER

MATERIALS SCIENCE & ENGINEERING

R

Reports: A Review Journal

Two-dimensional black phosphorus: Synthesis, modification, properties, and applications

Ya Yi, Xue-Feng Yu, Wenhua Zhou, Jiahong Wang, Paul K. Chu

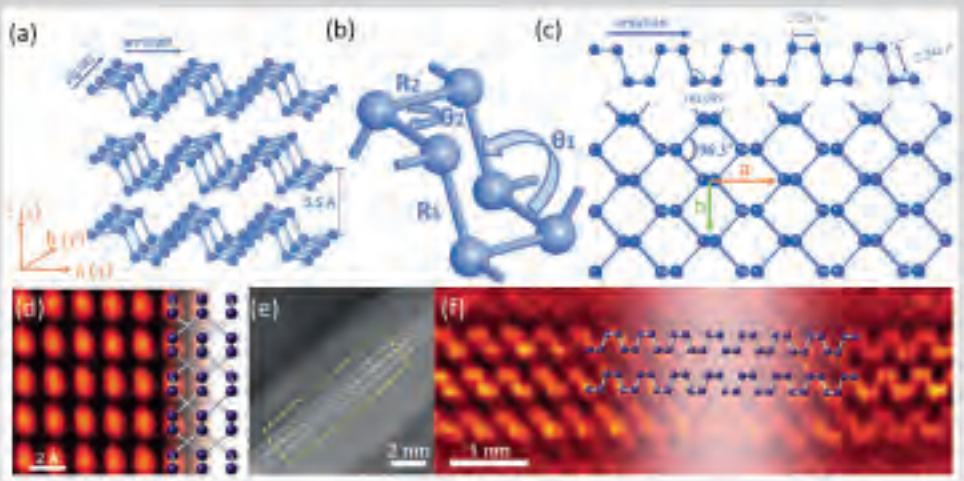

Available online at www.sciencedirect.com

ScienceDirect

Materials Science and Engineering R 120 (2017) 1–33

Contents lists available at ScienceDirect

Materials Science and Engineering R

journal homepage: www.elsevier.com/locate/mser

Two-dimensional black phosphorus: Synthesis, modification, properties, and applications

Ya Yi[a], Xue-Feng Yu[a,*], Wenhua Zhou[a], Jiahong Wang[a], Paul K. Chu[b,*]

[a] Institute of Biomedicine and Biotechnology, Shenzhen Institutes of Advanced Technology, Chinese Academy of Sciences, Shenzhen 518055, PR China
[b] Department of Physics and Materials Science, City University of Hong Kong, Tat Chee Avenue, Kowloon, Hong Kong, PR China

ARTICLE INFO

Article history:
Received 21 June 2017
Accepted 12 August 2017
Available online xxx

Keywords:
Black phosphorus
Two-dimensional materials
In-plane anisotropy
Electronics
Optoelectronics
Biomedicine

ABSTRACT

Black phosphorus (BP) discovered a century ago constitutes a new class of two-dimensional (2D) materials and is intensively studied as a 2D semiconductor. The high carrier mobility and tunable and moderate direct bandgap of BP deliver great promise in electronic and optoelectronic applications and the unique intrinsic anisotropy arising from the puckered structure produces extraordinary electronic, optical, transport, thermal, and mechanical properties that can be exploited in the design of new devices. Furthermore, the biodegradability and biocompatibility of BP bode well for biomedical applications. In this review, we discuss recent advances pertaining to the synthesis, modification, properties, and applications of BP and address some of the challenges and opportunities of BP research.

Contents

* Corresponding authors.
E-mail addresses: xf.yu@siat.ac.cn (X.-F. Yu), paul.chu@cityu.edu.hk (P.K. Chu).

http://dx.doi.org/10.1016/j.mser.2017.08.001
0927-796X/

1. Introduction

In the past decade, two-dimensional (2D) crystals have burgeoned to be one of the most extensively studied class of nanomaterials [1,2]. The atomically thin nature leads to strong quantum confinement effects and large surface-to-volume ratio, which are exceptional and fascinating properties that their bulk counterparts do not possess. These remarkable properties can be exploited in the electronic, optical, thermal, chemical and mechanical fields and the materials have thus attracted tremendous interest from both the scientific and practical standpoints [3–5]. Graphene, the first genuine 2D crystal, continues to be most widely studied materials since its emergence in 2004 [6–8]. However, although graphene possesses unique electrical, optical, and physical properties, the absence of a bandgap severely limits its application to the semiconductor industry. Hence, much effort has been devoted to the search of alternative 2D semiconductors which include graphene-analogous layered materials such as transition metal dichalcogenides (TMDs) [9–12] and black phosphorus (BP) [13–18].

BP, the most stable allotrope of phosphorus, was first synthesized in 1914 by Bridgman [19]. After a century, it was reintroduced to the scientific community as a member of 2D materials. Since it possesses several advantages over graphene and TMDs, it is attractive to future 2D devices [20,21]. For example, in contrast to TMD compounds, BP is an elementary crystal which can be prepared with high purity and unlike few-layer TMDs with indirect bandgaps, BP has a direct bandgap that varies from about 0.3 eV of the bulk to almost 2.0 eV of the monolayered structure [16]. Moreover, the direct bandgap can be tuned by adjusting the layer number, strain engineering, and chemical modification [22–24], thereby allowing broadband absorption from the visible to mid-infrared range rendering it suitable for many optoelectronic applications [25]. Another significant advantage of BP is its relatively high charge carrier mobility of up to 1000 $cm^2/V\,s$ observed from few-layer BP field-effect transistors (FETs) at room temperature and this value surpasses the mobility of TMDs-based FETs significantly [21]. Although the current on-off ratio of BP FETs ($\sim 10^3$–10^5) [13] is smaller than that of TMDs ($\sim 10^8$–10^{10}) [11], it is generally regarded to be a satisfactory trade-off between carrier mobility and current on-off ratio. As a matter of fact, BP bridges the gap in the mobility/on-off ratio between graphene and TMDs [13]. From the perspective of device applications, BP is preferred over TMDs due to its intrinsic ambipolar behavior, which is essential to the construction of logic devices consisting of both *n*- and *p*-type semiconductors [26–28]. The unique in-plane anisotropy of BP stemming from the puckered orthorhombic structure [29,30] produces unique electrical, optical, thermal, and mechanical properties [31–35] and provides more degrees of freedom to the design of novel devices. Another unusual feature that distinguishes BP from graphene and TMDs is its biocompatibility and biodegradability rendering the materials suitable for biomedical applications [36,37].

Despite these favorable properties, there are challenges and obstacles that must be overcome in order to bring the materials and technology to fruition. One of them is the environmental instability of BP thin films [38,39]. When exposed to an ambient environment with moisture and oxygen, phosphorus oxide is formed and degradation of BP adversely affects device performance and hinders research of its fundamental properties [40,41].

In this review, we describe recent research progress on nanoscale BP crystals focusing on the preparation of BP materials in the forms of bulk crystals, thin films, and quantum dots, passivation schemes for high stability, properties, and applications. A prospective on future research directions of the fascinating 2D materials is also presented.

2. Synthesis

2.1. Bulk crystal growth

Synthesis of black phosphorus (BP) crystals dated back to 1914 when Bridgman converted white phosphorus to BP at 200 °C and 1.2 GPa [19] and this high-pressure synthesis method was a common technique to obtain BP in the following 40 years.

Afterwards, Bridgman also converted red phosphorus (RP) to BP at room temperature at 4.5 GPa/8.0 GPa with/without shear stress [42,43]. In 1981, large single-crystal BP crystals (4 mm in diameter and 5 mm in length) were obtained by Shirotani by melting BP at over 500 °C under 2.3 GPa in a wedge-type cubic anvil high-pressure apparatus [44]. Later, Endo et al. increased the crystal size to $5 \times 5 \times 10\,mm^3$ using a large multi-anvil-type high-pressure apparatus in which RP was first converted to polycrystalline BP under 1.0 GPa at 550 °C and then melted at 900 °C. When the materials cooled gradually, solidification yielded high-quality of BP single crystals [45]. In 2012, Rissi et al. showed structural changes in BP at a high pressure of 12 GPa and under these conditions, amorphous RP was converted to rhombohedral BP and then cubic BP [46]. In the 1960s, an atmospheric-pressure process known as the bismuth (or mercury) – flux method was developed to synthesize BP [47,48]. In this technique, the melted bismuth was poured onto white phosphorus which was successively purified with 15% HNO_3 and distillation. The mixture was then heated to 400 °C for 20 h. By dissolving solid bismuth with 30% HNO_3, needle- or rod-like BP single crystals ($5 \times 0.1 \times 0.07\,mm^3$) with the needle direction along the *a*-axis were obtained. This preparation process allowed doping with silicon or germanium in an easy way in spite of its toxic and time-consuming nature.

In 2007, BP was synthesized at a low pressure without the use of toxic catalysts or "dirty" flux [49,50]. Lange et al. produced high-quality BP single crystals under low-pressure conditions at 600 °C from RP by adding small quantities of gold, tin, and tin iodide. In this method, the reaction promoter SnI_4 was prepared by mixing tin and iodine in toluene. After the mixture was refluxed, crystallized SnI_4 was obtained after the solution cooled to room temperature. The starting materials, RP, SnI_4, gold, and tin were heated to 600 °C for 5 to 10 days in an evacuated silica ampule and after cooling to room temperature gradually, BP single crystals were obtained [49]. Nilges accelerated this process by adopting both SnI_4 and AuSn as precursors and the resulting crystal size was larger than 1 cm [50]. To further reduce side-products and improve the BP quality, Köpf et al. optimized the reaction conditions by replacing gold with tin. The modification only not simplified the procedure, but also reduced the cost [51].

2.2. Mechanical exfoliation

BP single crystals are composed of vertically stacked and weakly interacting layers held together by van der Waals (vdW) forces. This layered structure facilitates cleavage of atomically thin BP layers with adhesive tapes. While large-scale production of BP thin films is still in the infancy stage, mechanical exfoliation continues to be one of the most efficient ways to obtain high-quality and small-scale BP flakes or sheets [17]. This technique is also known as "peeling" inherited from graphene cleavage. The BP thin flakes are first peeled from the parent crystal and thinned by repeated adhesion/separation method with the aid of adhesive tapes. After transferring to a substrate such as SiO_2/Si, the BP is cleaned with acetone and isopropyl alcohol to remove tape residues. To optimize the exfoliation process, Castellanos-Gomez et al. employed viscoelastic poly-dimethylsiloxane (PDMS) to exfoliate the BP flakes after using the tape. This process increases the yield and reduces contamination from the sticky tape [39].

Since the cleavage method is neither scalable nor controllable with regard to size and thickness, improved fabrication methods have been proposed. For example, plasma-assisted fabrication [52–54] has been implemented to prepare other 2D materials such as graphene [55] and MoS_2 [56]. Lu et al. reported a combined technique using mechanical cleavage and Ar^+ plasma etching to thin BP thin flakes down to a monolayer [52] (Fig. 1a). To more precisely control the thickness, Pei et al. conducted O_2 plasma treatment [54] in which the surface of BP was first oxidized to P_xO_y which served as a protective layer. During etching, a dynamic equilibrium between oxidation of BP and physical removal of the P_xO_y layer is established and the P_xO_y thickness and etching rate become constant. In this way, any designated number of layers down to a monolayer can be achieved by controlling the etching time [54] (Fig. 1b). Recently, Liu et al. reported a controllable conductive-atomic force microscopy (CAFM) technique for layer-by-layer thinning of BP [57]. This process generates patterned byproducts (phosphorus oxoacids) that can be removed with water rinsing and the remaining locally thinned BP regions retain the structural integrity. The BP FETs with thinned channels varying from 17 to 7 nm (Fig. 1c) show a larger on-off ratio by a factor of ~50 without significantly compromising the on-state current.

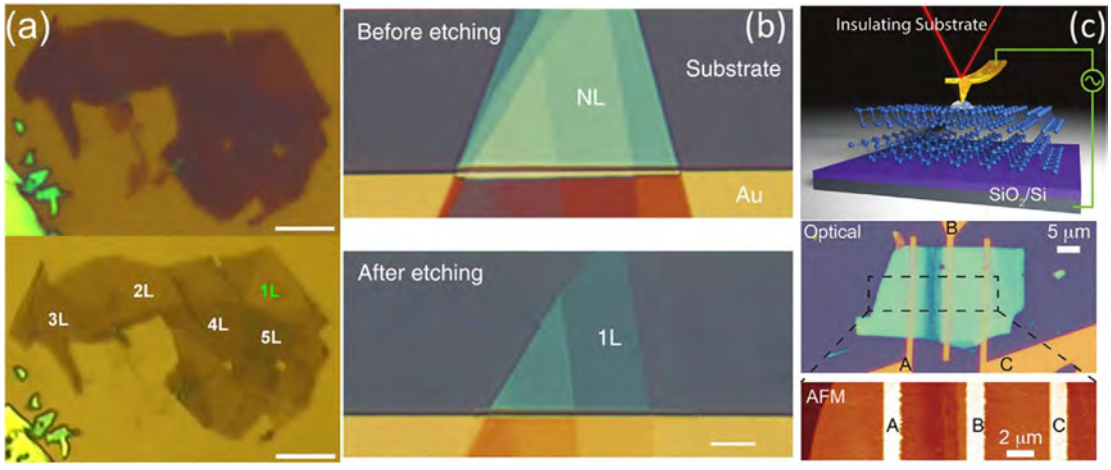

Fig. 1. Improved mechanical exfoliation methods of BP. (a) Optical image of multilayered BP flakes before and after Ar^+ plasma thinning. The scale bar is 5 μm. Reproduced with permission [52]. Copyright 2014, Springer. (b) Optical image of a mono-layer BP before and after etching by O_2 plasma. Reproduced with permission [54]. Copyright 2016, Nature Publishing Group. (c) Top: Schematic illustration of the alternating current (AC) mode CAFM patterning setup of BP on SiO_2/Si substrate. Bottom: Optical and AFM image of BP FETs fabricated with AC patterned (between electrodes A and B) and pristine BP (between electrodes B and C). Reproduced with permission [57]. Copyright 2016, Wiley.

A solid-state mechanochemical method termed ball-milling has been established to exfoliate bulk BP powders into few-layer BP nanosheets under the shear force applied by milling [58]. However, since BP is too reactive and unstable to endure the high-energy milling process, the BP powders are easily converted into RP if no auxiliary compounds are added. In this respect, Zhu et al. employed anhydrous LiOH powders as additives to inhibit this undesirable transformation [58]. The mixture containing bulk BP and LiOH powders was milled for 24 h with ZrO_2 balls and after rinsing with deionized water to remove excess LiOH and drying under vacuum, the milled BP powders were dispersed in an aqueous solution and few-layer BP with a small lateral size of 300–500 nm were collected from the supernatant. This ball-milling technique is a low-cost and eco-friendly means to produce BP nanosheets on a large scale and bridges the gap between research and industrial applications.

2.3. Direct thin film growth

To study the intrinsic properties and possible application of BP, methods that can synthesize wafer-scale crystalline thin films of BP are essential. In 2015, Li et al. reported a scalable approach to produce large-area (up to 4 mm) BP thin films with a thickness of about 40 nm [59]. In this method, the RP powders were evaporated at 400 °C and condensed onto a flexible substrate to form a thin film with controllable thickness by adjusting the time at 400 °C. The RP thin film was converted to BP thin films in a multi-anvil high-pressure cell (10 GPa) at room temperature. The bandgap of the BP thin films is 0.28 eV that is comparable to that of exfoliated BP thin films and the transistors comprising with the films exhibit a mobility of 0.5 $cm^2/V s$ that is much smaller than that of the exfoliated ones [60]. Very recently, Smith et al. mass-produced BP thin films 100 μm^2 in size and tens of nanometers thick [61]. They converted thin films of RP to BP at a low pressure (2.7 MPa) and high temperature (950 °C) with Sn and SnI_4 as the mineralizing agents. Amorphous BP thin films as thin as 1.9 nm were grown on graphene/copper and SiO_2/Si substrates by pulsed laser deposition (PLD) [62] and on a Ti foil by thermal vaporization [63]. In spite of recent advances, these direct growth methods are still not perfect probably due to the chemical instability of BP, but successful growth of wafer-scale monolayered graphene and TMDs by chemical vapor deposition (CVD) [64] may provide insights into large-scale and high-efficiency fabrication of layer-controllable BP.

2.4. Liquid exfoliation

Liquid exfoliation of 2D materials such as graphene, TMDs, and hexagonal boron nitride (*h*-BN or BN in short) offers good reference for large-scale production of BP nanosheets [65]. The key lies in the use of ultrasonic energy to break down the interlayer vdW forces in the appropriate solvents. The ideal solvents should possess the suitable surface energy to facilitate delamination while avoiding aggregation or sedimentation. Considering the chemical activity of BP, the solvents should also form a barrier that isolates the BP nanosheets from the external environment especially oxygen and water. In 2014, Brent et al. conducted liquid exfoliation of BP in N-methyl pyrrolidone (NMP) and after ultrasonication and centrifugation, 3- to 5-layer (5 L) high-purity BP nanosheets with dimensions of 200 × 200 nm^2 were obtained [66]. Since then, considerable efforts have been devoted to developing the liquid exfoliation technique to mass-produce BP with high quality, stability as well as controllable size and thickness. Kang et al. employed a sealed tip ultrasonication system with NMP as the solvent to prepare electronic-grade 2D BP dispersions [67]. The FET device composed of liquid-exfoliated BP nanosheets exhibited an ambipolar behavior with the current on/off ratio and hole mobility of 10^4 and 50 $cm^2/V s$, respectively [67]. Yasaei et al. produced crystalline BP nanosheets in *N*, *N*-dimethylformamide (DMF) and dimethyl sulfoxide (DMSO) solvents with controllable thicknesses. In DMF, more than 20% of the nanosheets were thinner than 5 nm, whereas in DMSO, they are between 15 and 20 nm [68]. Hanlon et al. prepared high-quality BP nanosheets in cumyl hydroperoxide (CHP) and 70% of the probed nanosheets had less than five layers and the lateral size was as large as 3 μm. The BP dispersion was stable for 200 h under ambient conditions since CHP formed a tightly packed shell to protect the BP nanosheets from water and oxygen [69]. To boost the yield of the BP nanosheets, Guo et al. improved the liquid exfoliation method by adding NaOH to NMP to form a saturated solution. In this technique, BP nanosheets with controllable size and thickness and stability in NMP and water were produced [70]. To improve the eco-friendliness, Zhao et al. substituted the conventional organic solvents with ionic liquids. The BP nanosheet dispersion with a high concentration (~0.95 mg/mL) was stable for more than one month under ambient conditions [71]. Other than using different solvents, the shear exfoliation technique using shear force to break down the interlayer vdW forces in the proper solvent was employed to improve the scalability of BP nanosheets. Using this method, ultrathin (~25% monolayer) [72] and thin (~2.8 nm-thick) BP nanosheets as large as 3.1 μm were produced with a high yield [73].

Besides 2D BP nanosheets, the liquid exfoliation technique can be applied to prepare BP quantum dots (BPQDs) which exhibit unique quantum confinement and edge effects. In 2014, Zhang et al. synthesized BPQDs with a size of 4.9 ± 1.6 and thickness of 1.9 ± 0.9 nm (Fig. 2a&b) [74]. The high-resolution transmission electron microscopy (HR-TEM) images of the BPQDs show lattice fringes of 0.34 and 0.52 nm, (Fig. 2a) arising from the (021) and (020) planes of the BP crystal, respectively. Typically, BP powders are added to the NMP solvent and sonicated in an ice-bath for 3 h. After centrifugation for 20 min at 7000 rpm, the supernatant containing the BPQDs was decanted gently. Sun et al. improved this technique by combining probe sonication and bath sonication to facilitate exfoliation [36] and the BPQDs had a lateral size of 2.6 ± 1.8 nm and thickness of 1.5 ± 0.6 nm. Ultra-small BPQDs with an average lateral size of ~2.1 nm were fabricated on a large scale by a solvothermal method and as shown in Fig. 2c. The ground BP powders were added to the saturated NaOH NMP solution under vigorous stirring for 6 h at 140 °C and the mixture was then centrifugated at 7000 rpm for 20 min [75].

Liquid exfoliation enables mass production of different BP nanostructures such as nanosheets and quantum dots and this simple and low-cost technique bodes well for application to printable electronics, solar cells, sensing, bioimaging, and phototherapy.

2.5. Electronic structure

2.5.1. Layer-dependent electronic band structure

The band structure of bulk BP was calculated using a tight-binding method by Takao et al. [95]. The self-consistent pseudopotential method adopted by Asahina et al. [96] in the 1980s revealed a direct gap of 0.3 eV with CBM and valence band maximum (VBM) both located at the Z point. This direct-gap property was confirmed by angle-resolved photoemission spectroscopy (ARPES) and *ab initio* calculation (Fig. 7a) [21]. When BP is thinned to a monolayer, it retains the direct bandgap. This is different from semiconducting TMDs which undergo indirect-to-direct bandgap transition as they are reduced to a single layer [10]. In monolayered BP, the original Z point in the bulk folds back to the Gamma (Γ) point, but the exact top of the valence band deviates from the Γ point with a small value of less than 10 meV. Hence, it can still be regarded as a direct bandgap semiconductor [30].

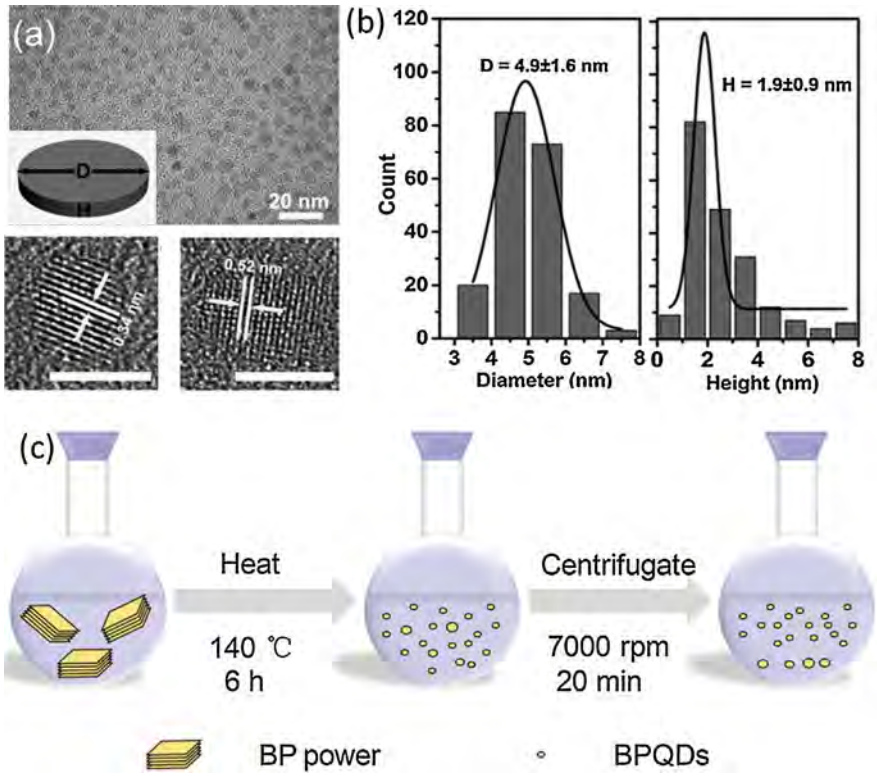

Fig. 2. Liquid exfoliation of BPQDs. (a) Top: TEM image of BPQDs. Bottom: HR-TEM images of BPQDs with different lattice fringes of (left) 0.34 nm and (right) 0.52 nm. (b) Statistical analysis of the (left) diameters (D) and (right) thickness (H) of 200 BPQDs measured from TEM images. (a-b) Reproduced with permission [74]. Copyright 2015, Wiley. (c) Schematic illustration of the synthesis process to produce BPQDs using a solvothermal method in saturated NaOH NMP solution. Reproduced with permission [75]. Copyright 2016, Wiley.

The quasiparticle bandgap of monolayered BP calculated without considering electron-hole interactions has been theoretically predicted to be 1.45 to 2.0 eV by density-functional theory or first-principles calculation. The bandgaps decrease monotonically with increasing thickness reaching a value of about 0.3 eV for the bulk crystal [20,23,30,97]. This layer-dependent bandgap evolution is demonstrated in Fig. 7c, which depicts the band structure of BP from 1 to 5 L derived by the HSE06 method [98]. The bandgap of monolayered BP has been experimentally determined to be 2.05 eV by scanning tunneling microscopy (STM) by only probing the fresh cleaved surface layer of BP crystal (Fig. 7b) [99]. In thicker BP films, the stronger interlayer interactions enlarge the dispersion of VBs and CBs in the direction normal to the layers giving rise to a smaller bandgap [97]. As shown in Fig. 7d, the layer dependent bandgaps calculated by different methods [30] can be fitted with an exponential decay relationship: $A/N^{\alpha}+B$ (N = layer number) and the bulk bandgap can be obtained by extrapolation [22]. The parameter α varies from 0.53 to 0.96, which is smaller than the perpendicular quantum confinement result ($\alpha = 2$), indicating strong vdW forces that isolates electrons between adjacent sheets. Qiao et al. stated that the wave function overlap played a dominant role in the interlayer interactions resulting in steep reduction of the bandgap from mono-layer to multi-layer [30]. It should be noted that photoluminescence (PL) and absorption spectra tend to underestimate the bandgap of BP thin films because of the large exciton binding energy.

Apart from the bandgap, the work function and band alignment are also tunable by varying the layer thickness [98]. According to first-principles calculation adopting the HSE06 approach, the work function decreases rapidly from 1 L (5.16 eV) to 3 L (4.56 eV) by 0.6 eV and then slowly to 5 L (4.5 eV) by only 0.06 eV, showing a similar trend as the bandgap. With regard to band alignment, the VBM and CBM change oppositely with as the thickness is increased from 1 to 5 L. That is, the VBM shifts upwards rapidly while the CBM shows a slow downward shift, as shown in Fig. 7e. The sensitive layer dependent work function and VBM can be utilized to moderate the Schottky barrier height and contact resistance in BP-based devices.

2.5.2. Anisotropic electronic structure

2.5.2.1. Electronic band dispersions and effective mass. As a result of the puckered structure, the electronic band dispersions are highly anisotropic around the direct bandgap (located at the Γ point) in monolayered BP [30]. In particular, as shown in Fig. 8a, along the Γ-Y direction (y-axis in Fig. 6a) which is the armchair direction (AC direction) in real space, both the top of VB and bottom of CB have relative large band curvatures. However, these bands appear to be almost flat along the Γ-X direction (x-axis in Fig. 6a) that corresponds to the zigzag direction (ZZ direction) in real space [100]. The inhomogeneous electron dispersions in BP have been confirmed by STM [99]. Consequently, the effective mass, m^*, is expected to be highly anisotropic since m^* is proportional to the inverse of the band curvature according to the formula $m^* = \hbar^2[\partial^2 E/\partial k^2]^{-1}$, where E is the energy and k is the reciprocal lattice vector (Fig. 8d). Theoretical simulation predicts that in few-layer BP, m^* of the charge carriers [both electrons (m_e^*) and holes (m_h^*)] along ZZ is larger than that along AC by an order. To be specific, m_e^* and m_h^* are 0.17 m_0 and 0.15 m_0 along ZZ (m_0 is the free electron mass), whereas they increase to 6.35 m_0 and 1.12 m_0 along AC, respectively [23,30,98,99]. Liu et al. experimentally demonstrated that in a 10-nm-thick BP flake, $m_e^* \approx m_h^* \approx 0.3\ m_0$ along ZZ and these values are

significantly larger along AC. That is, $m_e^* \approx 2.6\, m_0$ and $m_h^* \approx 8.6\, m_0$ showing the same trends as predicted theoretically [20]. In bulk BP, the anisotropy of m_e^* almost vanishes (0.15 m_0 along AC and 0.12 m_0 along ZZ), whereas the anisotropy of m_h^* is preserved with the value along AC (0.71 m_0) nearly 7 times that along ZZ (0.11 m_0) [30].

2.5.2.2. Strain-engineering of the anisotropic electronic structure of BP. In bulk BP, appreciable anisotropy can be observed along different crystal axes under high pressure. The lattice parameter *b* (ZZ direction) of the BP crystal decreases with increasing pressure, while the lattice parameter *a* (AC direction) is almost unchanged below 2.7 GPa [29]. In monolayered BP, Fei et al. found that besides the lowest-energy CB (first CB, red line in Fig. 8a), there was a nearby upper CB (second CB, blue line in Fig. 8a) with orthogonal anisotropy to that of the first band, *i.e.*, being almost flat along the Γ-Y (AC) direction while highly dispersive along the Γ-X (ZZ) direction [100]. Since the lowest-energy band edge is predominant in electrical transport, switching the energy order between the first and second CBs can rotate the electron anisotropy by 90° thereby changing the electron mobility and electrical properties. By applying 3–4% biaxial strain or 5–6% uniaxial strain along ZZ, band switching can be realized as shown in Fig. 8b&c. The spatial preference of conductance in monolayered BP can thus be rotated by 90° in-plane as shown in Fig. 8d but uniaxial strain along the armchair direction cannot cause such band switching.

3. Surface modification

3.1. Decomposition risk

Despite the promising potential, BP degrades readily under ambient conditions due to chemical reactions with oxygen and water. In 2015, Island et al. studied the environmental instability of mechanically exfoliated few-layer BP. As shown in the selected AFM images (Fig. 3), when a BP flake was placed in air, water droplets formed on the surface in 3 h and completely covered the flake forming a large convex meniscus after 122 h. The volume increased by over 200% due to condensation of moisture from air [76]. The mechanism of BP degradation has recently been investigated. BP has a puckered honeycomb structure in which a phosphorus atom is covalently bonded to three neighboring atoms exposing a lone-electron pair. The lone-pair electrons in BP can react with oxygen to form oxidized BP which is converted to phosphoric acid in the presence of water. The exposed BP undergoes continuous oxidization and degradation [77], which has been shown to be associated with ambient light [78]. As the BP flakes are exposed to air under light irradiation, superoxide anions are formed on the BP and as a result, the oxidation rate of BP flakes is proportional to the oxygen concentration and light intensity [79]. Thinner BP nanosheets degrade more rapidly [79] and the phenomenon can be explained by the energy band theory. The energy band of layered BP depends on the thickness and as the number of layers decreases, the bandgap enlarges introducing more overlap between the BP band edge and oxygen acceptors. Oxidization-induced degradation produces compositional changes and deteriorated electronic and optical properties [76]. Hence, it is crucial to prevent degradation and the main protection schemes are surface encapsulation [53,54,80–84], chemical modification [24,85,86], and doping [87].

3.2. Surface encapsulation

To prevent degradation, aluminum oxide (AlO_x) was used to passivate BP and block oxygen and water molecules [54]. The surface morphology of AlO_x-coated BP did not change significantly after 7 days and the AlO_x-coated BP based FET showed long-term stability in terms of conductivity, switching ratio, and mobility (Fig. 4). However, encapsulation with AlO_x or Al_2O_3 by atomic layer deposition (ALD) might cause minor inconvenience because of rapid oxidation of BP during the process [40]. Pei et al. showed that upon air exposure, a P_xO_y layer formed on the surface of the BP but the deeper layers were intact [54]. Surface oxidization can prevent few-layer BP from deterioration and leave the underneath BP layers with high hole mobility. This offers a great opportunity to use a native oxide layer as the protective layer [54]. In addition, other conventional materials such as Teflon [88], TiO_2 [89], and polymethyl methacrylate (PMMA) [53] have been employed in surface encapsulation to prevent BP from ambient degradation.

Another strategy to mitigate BP degradation is capping with other 2D layered materials such as graphene [82] and BN [83] using vdW epitaxy. The technique produces a distinct layered structure form a functional heterogeneous 2D structure by vertical assembling without restriction by the lattice compatibility and the vdW interfaces can protect BP simultaneously. Zhao et al. proposed another method to encapsulate BP flakes by vdW epitaxy using an organic self-assemble of monolayer as passivation [84]. Multiscale simulation demonstrated that perylenetetracarboxylic dianhydride (PTCDA), 7,7,8,8-tetracyano-*p*-quinodimethane (TCNQ), 1,4,5,8-naphthalenetetracarboxylic dianhydride (NTCDA), and 3,3′,4,4′-benzophenonetetracarboxylic dianhydride (BTDA)-TCNQ could self-assemble into a stable and close-packed herringbone hydrogen bonded network on BP at 400 K. This protection layer not

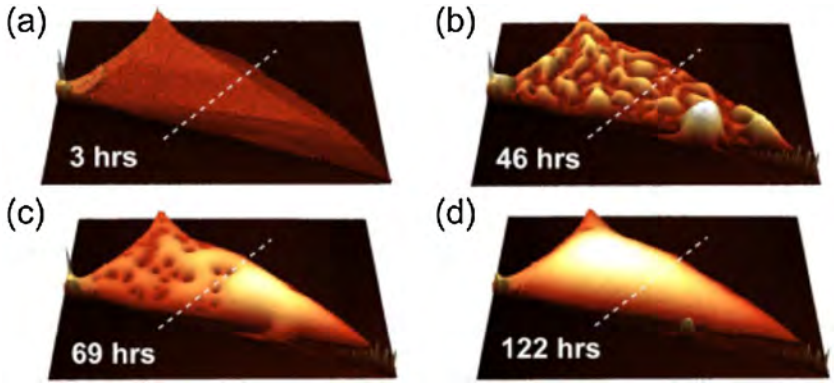

Fig. 3. Decomposition of BP under ambient conditions. AFM images of a BP flake in air taken at (a) 3 h, (b) 46 h, (c) 69 h, and (d) 122 h after exfoliation. Reproduced with permission [76]. Copyright 2015, IOP publishing.

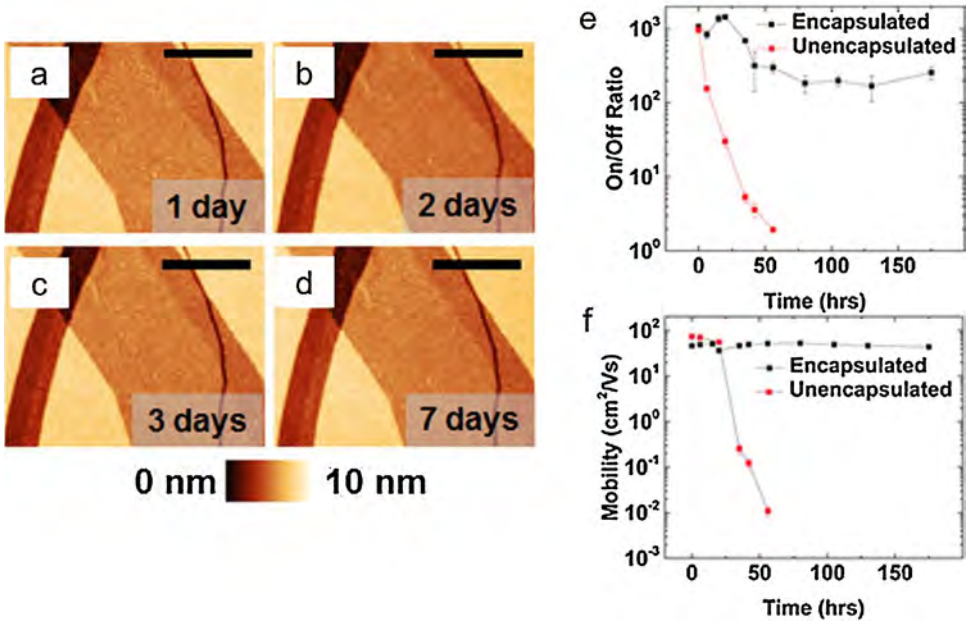

Fig. 4. ALD passivation of BP. AFM height images of Al_2O_3 encapsulated BP in after (a) 1 day, (b) 2 days, (c) 3 days, and (d) 7 days in ambient conditions. Scale bars: 500 nm. (e) Current on-off ratio and (f) hole mobility for encapsulated and non-encapsulated BP FETs versus ambient exposure time. Reproduced with permission [40]. Copyright 2014, American Chemical Society.

only isolates BP from ambient O_2 and H_2O, but also preserve the electronic properties of BP.

Shao et al. fabricated polylactic acid-glycolic acid copolymer (PLGA) encapsulated BPQDs using an emulsified solvent evaporation method [37]. The hydrophobic biopolymer PLGA forms internal hollow nano-microbubbles in which the BPQDs are packed. The absorption curve and photothermal properties of the PLGA/BPQDs are maintained for more than 8 days, while the untreated ones degrade with time.

3.3. Chemical modification

Another effective method to protect BP is coordination and covalent modification [24,85,86]. Zhao et al. synthesized a titanium benzenesulfonate ligand (TiL_4) with the empty orbital of titanium and strong electronic absorption of benzenesulfonate. TiL_4 can coordinate with the BP lone-pair electrons (Fig. 5a&b). In contrast to serious degradation observed from the bare BP nanosheets, the TiL_4@BP nanosheets exhibit excellent stability during long-term

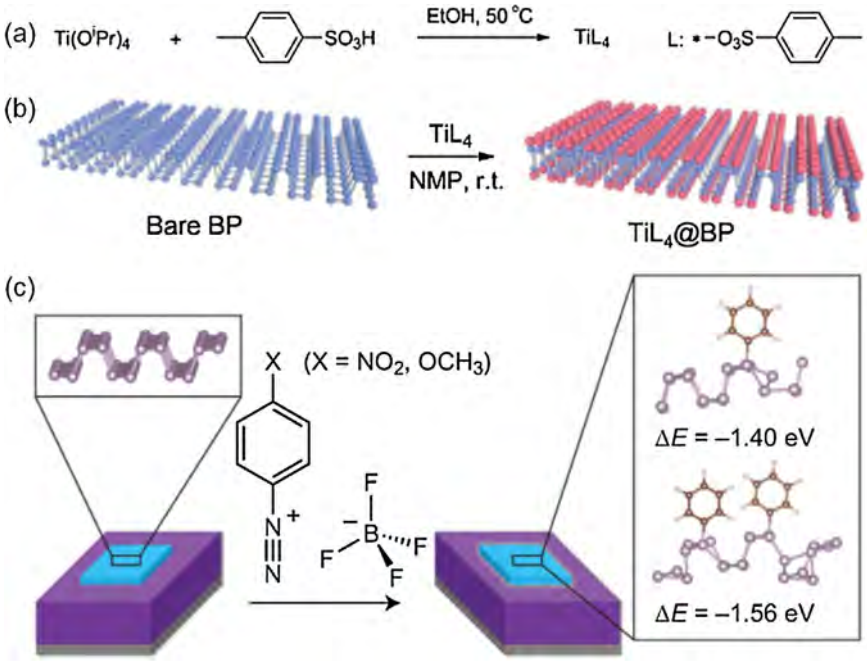

Fig. 5. Coordination and covalent modifications of BP. (a) Synthesis and structural formula of TiL_4; (b) surface coordination of TiL_4 to BP; b) TiL_4@BP sheets on Si/SiO_2 and exposed to the humid air at room temperature for 0 h (left), 12 h (middle), and 24 h (right). (a-b) Reproduced with permission [85]. Copyright 2016, Wiley. (c) Reaction scheme of benzene-diazonium tetrafluoroborate derivatives and mechanically exfoliated few-layer BP (light blue) on a Si (grey)/SiO_2 (purple) substrate. Reproduced with permission [90]. Copyright 2016, Nature Publishing Group. (For interpretation of the references to colour in this figure legend, the reader is referred to the web version of this article.)

dispersion in water as well as exposure to air and degradation in the optical absorbance and photothermal performance is minimal. Ryder et al. demonstrated that the exfoliated BP nanosheets could be stabilized with *p*-methoxybenzene diazonium and *p*-nitrobenzene diazonium salts *via* formation of phosphorus–carbon covalent bonds (Fig. 5c) [90]. The functionalized BP nanosheets show no obvious degradation even after 3 weeks and the benzene ring enhances the electron mobility and switching ratio of the BP FET. In addition to coordination and covalent bonding, non-covalent bonding can be implemented to modify BP nanosheets. Abellán et al. functionalized bulk BP with 7,7,8,8-tetracyano-*p*-quinodimethane (TCNQ) and perylene bisimide (PDI) and the process produced stable hybrids on the surface of the BP flakes and PDI improved the robustness of the BP flakes against oxygen as well [86].

3.4. Doping

As a conventional technique semiconductor processing, elemental doping is a viable means to improve the BP stability. Yang et al. synthesized Te-doped BP with red phosphorus and tellurium at a high temperature of 1000 °C and pressure of 2 GPa. Doping with Te produces resistance to ambient degradation [87]. After exposure for 21 days, the mobility of the FET composed of Te-doped BP was over 200 $cm^2/V\,s$ and the on-off current ratio was about 500. The reason for the improved electronic performance lies in the shift of the conduction band minimum (CBM). Specifically, the CBM of the Te-doped BP is close to or below the redox potential of O_2/O_2^-, whereas the CBM of the undoped BP is above the redox potential of O_2/O_2^-. This band shift reduces the generation of light-induced O_2^- and as a result, for the same thickness, oxidization of the Te-doped BP is abated.

4. Properties

BP has many intriguing properties and in this section, we review recent results about the properties of BP and emphasis on its unique intrinsic in-plane anisotropy.

4.1. Lattice structure

4.1.1. BP bulk crystal

BP has a layered structure similar to that of graphite and the intralayered atoms are strongly covalently bonded, while the adjacent layers are connected by the relatively weak vdW force. The lattice structure of BP was first determined by Hultgren et al. by X-ray powder diffraction [91]. There are eight atoms in a unit cell and the calculated density is 2.69 that is consistent with the experimentally determined value of 2.70. The unit cell consists of two layers and is side-centered orthorhombic with $a = 4.53$ Å, $b = 3.36$ Å, $c = 11.17$ Å [20]. The lattice vectors (a, b, c) are marked with the coordinated axes (x, y, z) for simplicity in Fig. 6a. The relatively large c is associated with the non-planar structure and two AB-stacked layers with a spacing of 5.5 Å in the bulk unit cell (Fig. 6a&b) [16,18]. This AB stacking order and lattice parameter have been verified by annular dark-field scanning transmission electron microscopy (STEM) (Fig. 6d) and *ab initio* simulation [92,93]. Fig. 6e&f shows the low- and high-magnification annular dark-field-STEM images of the edge of BP along the (100) direction providing a cross-sectional view of the layered structure. In the unit cell, each atom is bonded to three nearest neighbors. Two of the bonds are in the same plane with a hinge angle (θ_2) of 96.3° and a covalent P–P bond (R_2) with a length of 2.224 Å. The third bond connects the atoms in adjacent planes with larger dihedral angle (θ_1) of 102.095° and bond length (R_1) of 2.244 Å as shown in Fig. 6b [18].

4.1.2. Phosphorene

Phosphorene, as a phosphorus analogue of graphene, refers to the monolayered BP crystal. After isolation from bulk BP, AFM shows that phosphorene has a thickness of 0.85 nm [20]. As shown in Fig. 6c, the orthogonal lattice parameters of phosphorene are 4.62 and 3.35 Å along the a and b axis, respectively. TEM confirms that the mechanically exfoliated phosphorene layers are crystalline [39]. Owing to sp^3 hybridization, the six atoms are linked to form a puckered hexagonal ring which is different from the

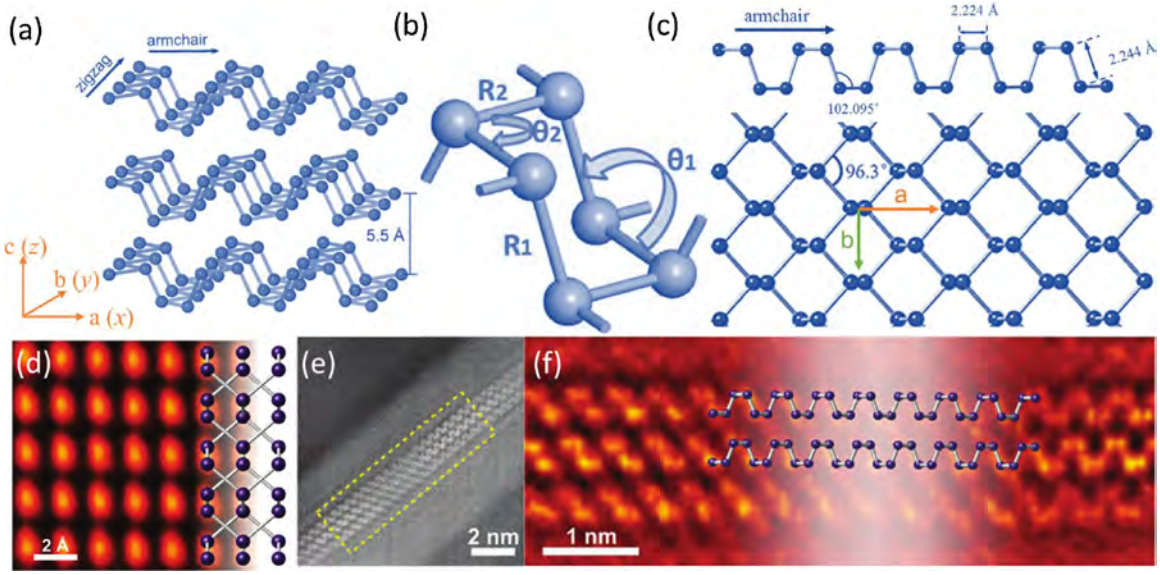

Fig. 6. Lattice structure of BP crystal. (a) Layered crystal structure of BP marked with lattice vectors (a, b, c) and coordinate axes (x, y, z). The layer-to-layer spacing is around 5.5 Å. Reproduced with permission [16]. Copyright 2015, American Chemical Society. (b) Structure parameters (R_1, R_2) and angles (θ_1, θ_2). Reproduced with permission [18]. Copyright 2016, Taylor & Francis Online Publishing. (c) Phosphorene in (top) side and (bottom) top view. The lattice parameters are marked and lattice vectors are indicated by arrows. (a)&(c) Reproduced with permission [60]. Copyright 2015, RSC Publishing. (d) Annular dark field-STEM images of BP viewed along the (001) direction. (e) Annular dark-field STEM image captured at an edge of a BP flakes showing multiple layers stacked together, or along the (100) direction. (f) Magnified image of the region in (e). (d–f) Reproduced with permission [92]. Copyright 2015, American Vacuum Society.

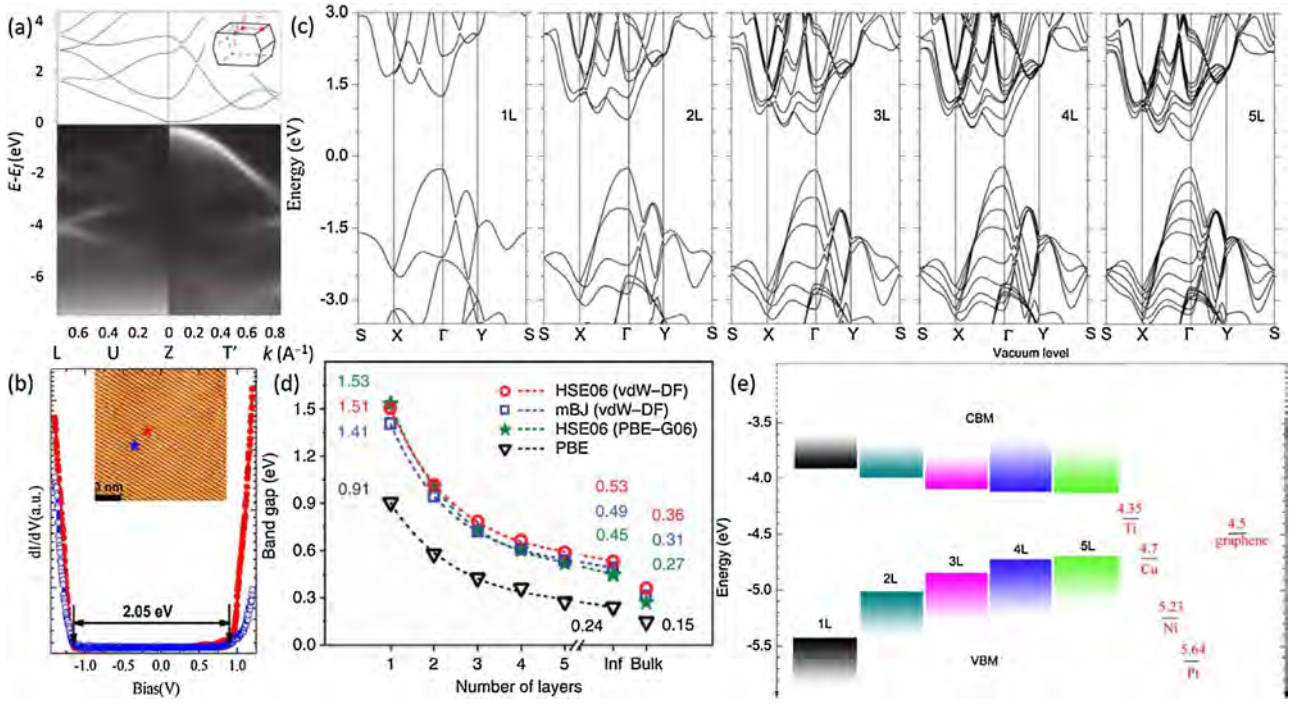

Fig. 7. Electronic structure of BP. (a) Band structure of BP bulk crystal mapped along U (L–Z) and T' directions by ARPES measurements with a clearly observed bandgap. Superimposed on top are calculated empty (blue solid) and filled (red dashed) bands. Inset: first Brillion zone marked with U, L, Z and T' points. Reproduced with permission [21]. Copyright 2014, Nature Publishing Group. (b) STM spectra in the log scale measured on the BP surface show a wide bandgap ~ 2.05 eV. Red and blue dotted curves were measured at different located marked by red and blue stars on the inset figure. Inset: topographic STM image of BP. Reproduced with permission [99]. Copyright 2014, American Chemical Society. (c) Band structure of 1 to 5 L BP obtained from HSE06 hybrid functional calculations. The direct bandgap featured is maintained for all thickness. (d) Evolution of the direct bandgaps as a function of the sample thickness. Functionals used for the structural optimization are shown in parentheses. Bandgaps are marked for the monolayer as well as the extrapolation and real values of bulk BP. Reproduced with permission [30]. Copyright 2014, Nature Publishing Group. (e) Variation of VBM and CBM of 1 to 5 L BP determined from the HSE06 calculation. (c&e) Reproduced with permission [98]. Copyright 2014, Nature Publishing Group. (For interpretation of the references to colour in this figure legend, the reader is referred to the web version of this article.)

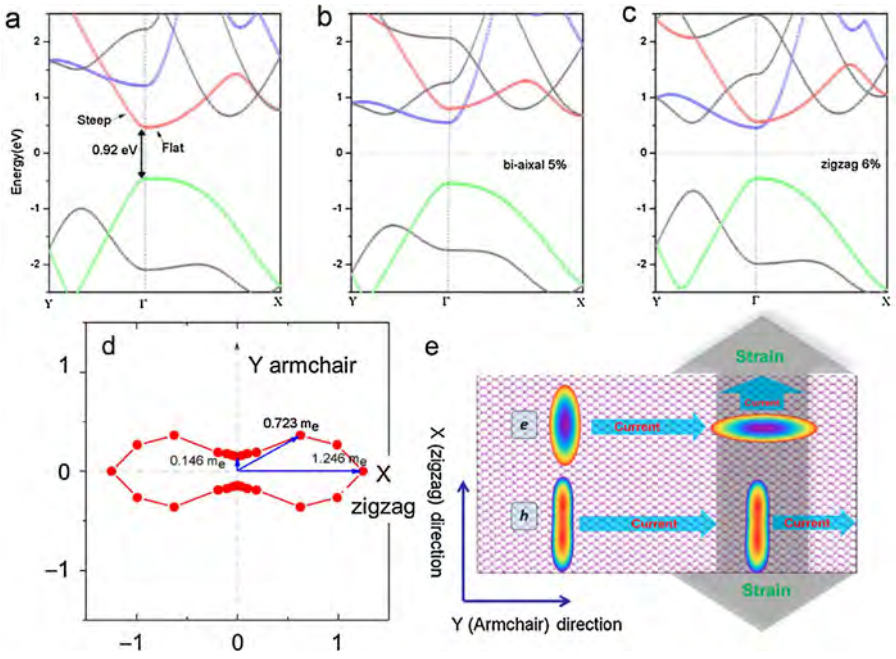

Fig. 8. Intrinsic and strain-engineered electronic band structure of monolayer BP. Band structures of (a) intrinsic monolayer BP, (b) with a 5% biaxial strain, and (c) with a zigzag uniaxial strain. (d) Electron effective mass in spatial distribution. (e) Schematic illustration of strain-induced rotation of electrical conductance in the monolayer BP. The color contours are those of 2D electron and hole band structures according to energy. (a–e) Reproduced with permission [100]. Copyright 2014, American Chemical Society.

perfectly flat graphene. When bulk BP is converted into the monolayered structure, the lattice parameter *a* increases by 0.11 Å and *b* decreases slightly by 0.02 Å [30]. The significant expansion of *a* in the few-layer system is caused by the increase in the bond angle rather than the bond length. The abrupt reduction of *a* from mono-layer to bi-layer results primarily from strong interlayer coupling.

4.1.3. Phase transition under pressure

Early in the 20th century, Bridgman discovered the phase transition of BP under high pressure since hydrostatic pressure was required to synthesize BP crystals [29,43]. Jamieson disclosed that BP crystals underwent reversible sequential phase transformation from the semiconducting orthorhombic phase to the semimetallic rhombohedral phase and then to the metallic simple cubic phase as the pressure is increased [94]. The first transition from arsenic-type orthorhombic to rhombohedral takes place at about 5 GPa at room temperature with a calculated density of 3.56. As the pressure goes up about 10 GPa, BP transforms to simple cubic with $a = 2.377$ Å with a density of 3.83. According to Morita, the transition pressure is essentially not affected by the temperature [29]. The simple cubic phase is robust even when the pressure is increased to 60 GPa but when the pressure is reduced, it will regress to the arsenic-type structure.

4.2. Optical properties

4.2.1. Layer-dependent excitonic bandgap

Linear optical absorption meaurement is a simple and direct way to determine the optical properties of materials. In BP, the electronic structure and bandgap evolution can be assessed by monitoring the thickness-dependent absorption and PL spectra [69,101,102]. Tran et al. simulated the absorption spectra of 1 to 3 L BP and bulk crystal as shown in Fig. 9a [22]. The first absorption peak, which denotes the excitonic bandgap, monotonically red-shifts with increasing thickness. The experimentally measured optical bandgaps vary among different research groups. For exapmle, Li et al. reported that the optical absorption peaks of BN-encapsulated BP on sapphire at 77 K were 1.73 eV for 1 L, 1.15 eV for 2 L, 0.83 eV for 3 L, and less than 0.75 eV for thicker samples. Besides, strong PL signals were detected close to the absorption edge from 1 to 3 L BP, as shown in Fig. 4b indicative of the direct bandgap [101]. Zhang et al. observed strong PL peaks from 2, 3, 4, 5 L BP at 1.29, 0.98, 0.88, and 0.80 eV, respectively (Fig. 9c) and the PL peak intensity increases dramatically with decreasing layer number regardless of the reduced amount of materials [102]. Hanlon et al. conducted PL measurements on liquid-exfoliated BP dispersions and observed clear emission lines at 2.07 and 1.38 eV and weaker features at 1.08, 0.98, and 0.94 eV attributed to optical transitions in 1 to 5 L BP, respectively (Fig. 9d) [69]. These different optical bandgaps exhibit the similar thickness-dependent trend. That is, as the layer number is increased, the bandgap decreases monotonically (Fig. 9b&c), consistent with the theoretical prediction (Fig. 9a) [22,30]. When the materials are uniformly doped, for example, *n*-type, the optical transition shows evident blue-shift due to Pauli blocking in thicker BP (>20 nm) and less abrupt absorption edge in thinner BP (<4 nm) [103].

4.2.2. Exciton binding energy

The optical bandgap measured from the absorption and PL spectra is significantly smaller than the theoretically predicted value, implying an appreciable exciton binding energy [20,22,34,101]. As shown in the photoluminescence excitation

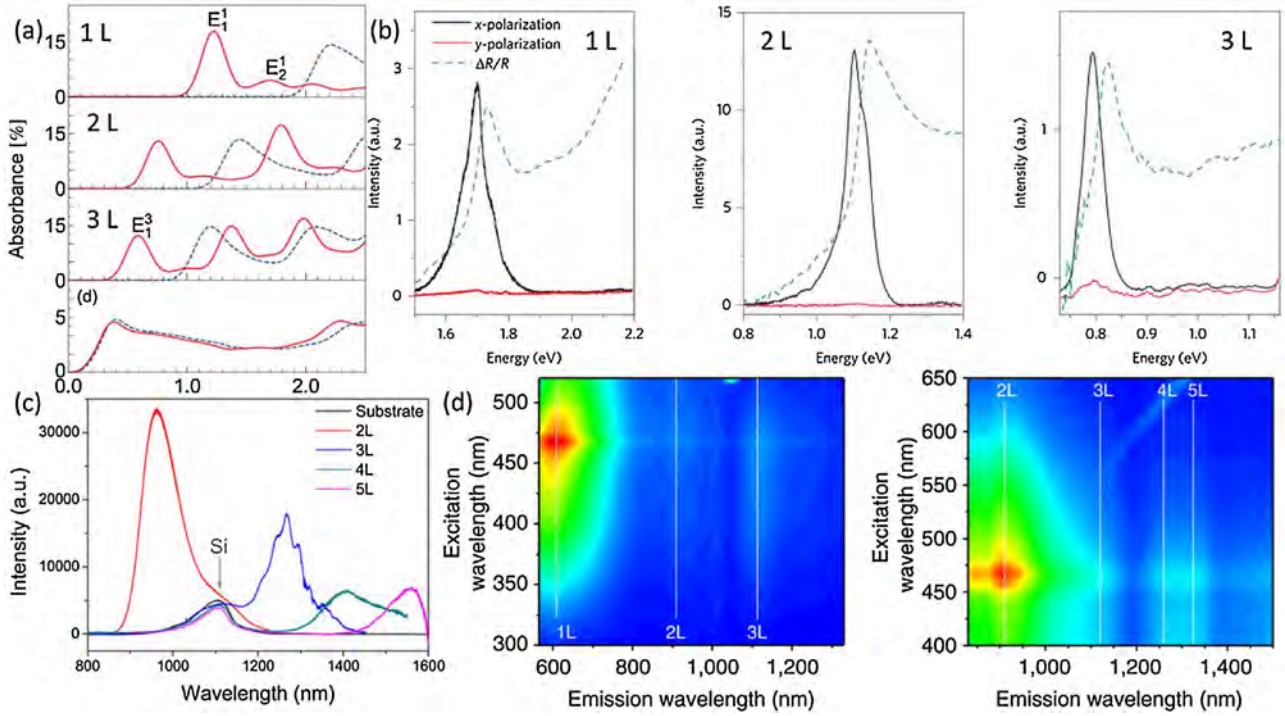

Fig. 9. Layer dependent excitonic bandgap of BP. (a) Optical absorption spectra of 1, 2, 3 L, and bulk BP for the incident light polarized along the AC direction using first-principle calculations. Reproduced with permission [22]. Copyright 2014, American Physical Society. (b) PL spectra of 1, 2 and 3 L at 77 K with 2.33 eV unpolarized excitation. PL signals along x-polarization (black curves) matches well with the absorption spectra (blue dashed curves), but along y-polarization (red curves) are absent. Reproduced with permission [101]. Copyright 2016, Nature Publishing Group. (c) PL spectra of 2, 3, 4 and 5 L BP measured at room temperature. Reproduced with permission [102]. Copyright 2014, American Chemical Society. (d) PL emission-excitation contour maps measured on size-selected BP dispersion in CHP exfoliated under inert gas conditions measured with a 550 nm (left) and 830 nm (right) cut-off filter in emission, respectively. Reproduced with permission [69]. Copyright 2015, Nature Publishing Group. (For interpretation of the references to colour in this figure legend, the reader is referred to the web version of this article.)

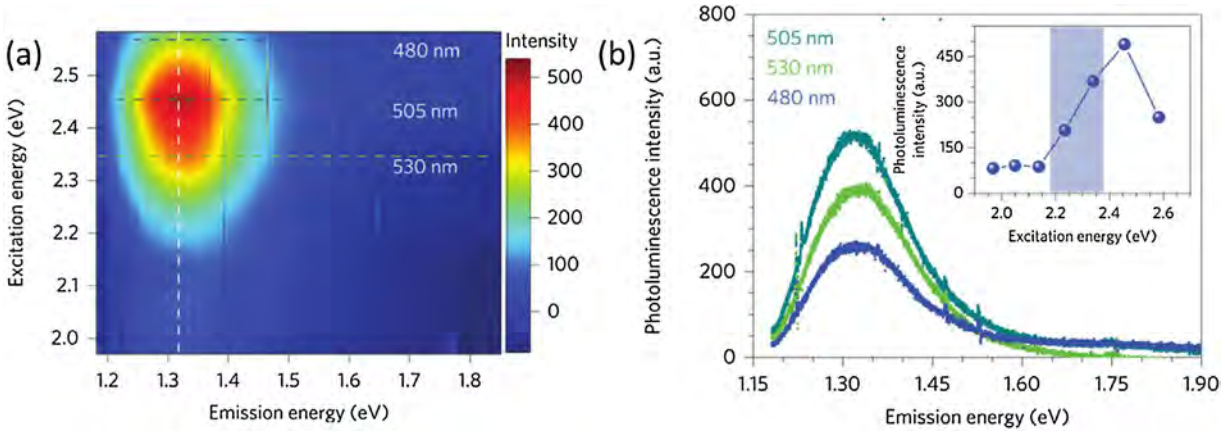

Fig. 10. Exciton binding energy in monolayer BP. (a) PLE intensity map as a function of both excitation and emission photon energies of monolayer BP. (b) Selected PL spectra along the three horizontal lines in (d), showing the PL is strongest under ~2.45 eV (505 nm) excitation. Inset: PL intensity at the emission peak of 1.32 eV as a function of excitation photon energy. The estimated quasiparticle band edge is indicated by the shaded region. (a-b) Reproduced with permission [34]. Copyright 2015, Nature Publishing Group.

(PLE) spectra of monolayer BP in Fig. 10a&b, PL shows the strongest intensity under 2.45 eV excitation and the quasiparticle band edge is extracted to be 2.26 ± 0.1 eV at the position with the largest PL peak intensity increasing rate (Fig. 10**a** inset). Meanwhile, the exciton emission peak is at 1.3 ± 0.02 eV indicating the ground-state exciton energy. Consequently, the exciton binding energy is 0.9 ± 0.12 eV, consistent with the theoretically predicted energy difference (~0.8 eV) between the quasi-particle and excitonic absorption peaks [34]. The large exciton binding energy is comparable to those of monolayered TMDs and 1D nanostructures primarily due to the reduced dimensionality and suppressed screening effect [22,97]. Moreover, dielectric screening such as that rendered by PMMA coverage [34] or BN encapsulation [101] reduces the exciton binding energy. For instance, for the BN capping layer, the exciton binding energy is only about 100 meV for monolayered BP and even smaller for multilayered BP [101]. With increasing thickness, the strong interlayer interactions reduce perpendicular quantum confinement reducing the excitonic effects and corresponding exciton binding energy. The simulation results estimate the upper limit of the exciton binding energy in bulk BP to be 30 meV that is similar to those of other bulk semiconductors [22].

4.2.3. Raman scattering spectra

4.2.3.1. Raman modes. The symmetry of BP bulk crystals can be described by the *Cmca* space group with 12 phonon modes [117] including three acoustic branches of the in-plane transverse acoustic mode (TA), longitudinal acoustic mode (LA), out-of-plane acoustic mode (ZA) as well as nine optical phonon branches including two IR-active modes (B_{1u} and B_{2u}), six Raman active modes (A_g^1, A_g^2, B_{1g}, B_{2g}, B_{3g}^1, and B_{3g}^2 as shown in Fig. 11a) and one silent mode (A_u). Among the six Raman active modes, only three of them, A_g^1, A_g^2 and B_{2g}, are detectable when the incident light is perpendicular to the sample plane (Fig. 11b). Unlike TMDs [118], the thickness-dependent Raman shift observed from mechanical exfoliated BP is not pronounced enough to accurately determine the number of layers [39]. Alternatively, the intensity ratio between the A_g^1 peak and silicon peak can be utilized to determine the thickness to 1–2 nm accuracy on the condition that the BP crystal orientation is aligned carefully to laser polarization (Fig. 11c) [39]. Guo et al. observed from solvent-exfoliated BP three Raman active modes with pronounced red-shifts as the thickness was increased. Among them, the A_g^2 mode is the most sensitive to the layer number with a shift from 467.6 to 465.0 cm^{-1} from 1 to 4 L (Fig. 11d) [70]. This prominent layer-dependent Raman shift can be attributed to the vdW interaction which is the dominant force along the out-of-plane direction and softens the vibrational energy. Moreover, since the influence of the vdW force becomes weak with increasing thickness, the largest red-shift occurs at the transition from mono-layer to bi-layer.

4.2.3.2. Temperature-dependent Raman spectra. Zhang et al. acquired temperature-dependent Raman spectra from 5 L BP flakes [102]. As the temperature decreases from 20 to −160 °C, the A_g^1, A_g^2, and B_{2g} modes show significant blue-shifts (Fig. 11e). The Raman mode frequency shift can be modeled by a linear relationship: $\omega = \omega_0 + \chi T$ (ω_0: mode frequency at 0 K; χ: first-order temperature coefficient). The χ values are −0.023, −0.023, and −0.018 for the A_g^1, A_g^2 and B_{2g} modes, respectively (Fig. 11f). These relatively large values (compared to those of bi-layer graphene and few-layer MoS_2) can be attributed to the superior mechanical flexibility of phosphene as a result of the unique puckered structure.

4.2.4. Anisotropic optical properties

4.2.4.1. Anisotropic absorption spectra. Fundamentally, the absorption spectra of few-layer BP exhibit strong in-plane anisotropy. The anisotropic infrared absorption properties of thin BP flakes (30 nm) were determined by Xia et al. by means of the polarization-resolved relative extinction spectra (Fig. 12a) [31]. The incident light propagates along the *z* direction and reaches the absorption maximum for *x*-polarized excitation (along AC). However, it is almost transparent to *y*-polarized light (along ZZ) [22]. The absorption coefficient for *x*-polarized excitation is about 10 times larger than that along the *y*-axis [104]. Li et al. obtained polarization-resolved reflection spectra from 1 to 3 L BP in the energy range between 0.75 and 2.5 eV and absorption peaks which marked the optical bandgap were observed for *x*-polarized excitation but disappeared for *y*-polarized illumination, as shown in Fig. 12b [101].

The strong anisotropic optical absorption stems from the symmetry-forbidden selection rule [25,31,34,101,105]. Specifically, the BP crystal structure possesses an inversion symmetry and mirror reflection symmetry (M_y) only along the *y*-axis. Electron states located at the high symmetry points such as the Γ point can be labeled by these two symmetries and accordingly, there are two optical selection rules: (1) Parity selection rule and (2) Polarization selection rule. The first rule requires that optical absorption only

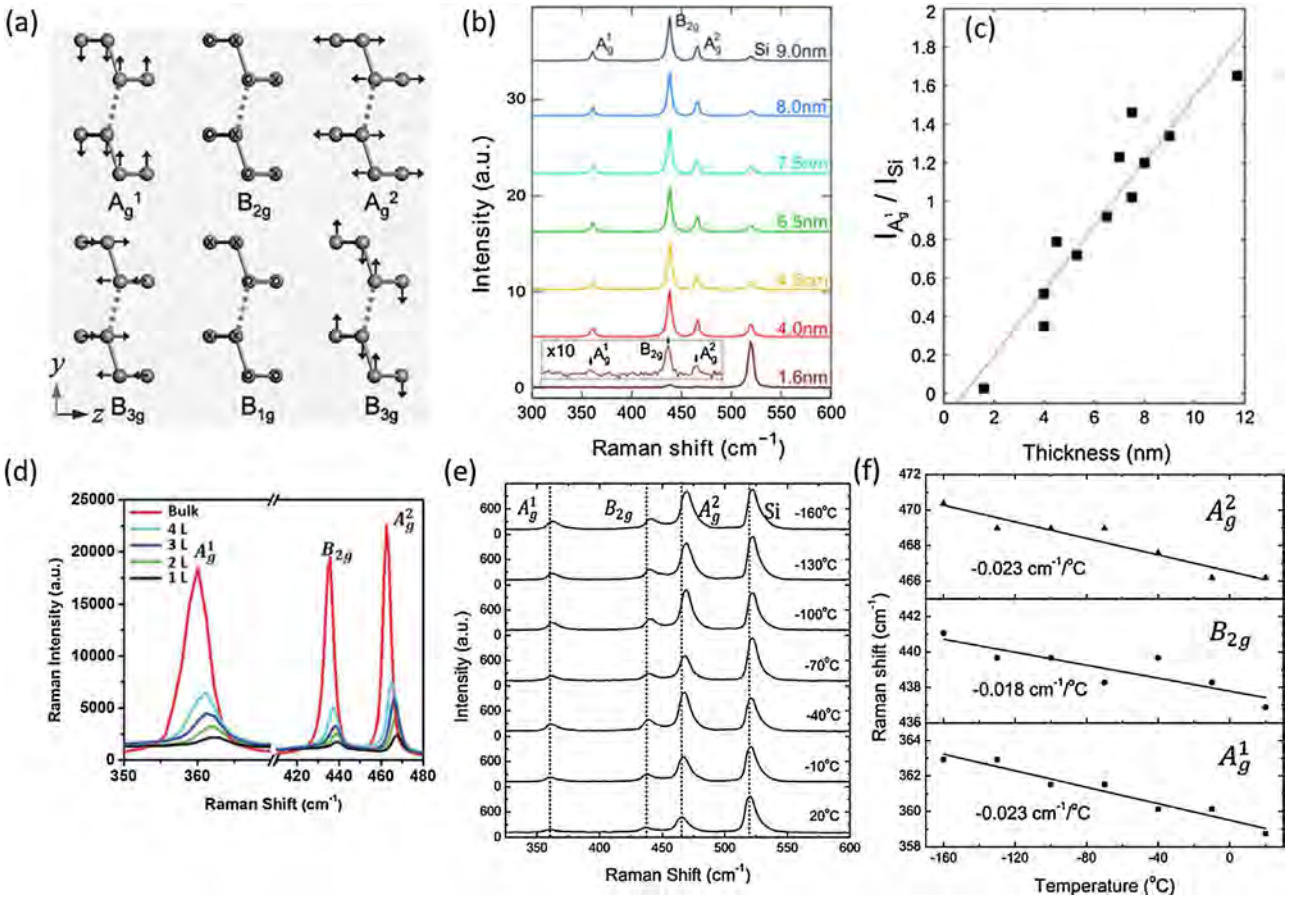

Fig. 11. Raman characteristics of BP. (a) Atomic displacements for Raman-active modes in BP. Reproduced with permission [119]. Copyright 2015, Wiley. (b) Typical Raman spectra for mechanical exfoliated few-layer BP under 514 nm excitation. (c) Thickness dependence of the intensity ratio between the A_g^1 and Si peaks. (b-c) Reproduced with permission [39]. Copyright 2014, IOP Publishing. (d) Raman spectra of bulk BP and solvent-exfoliated BP (1 to 4 L) under 633 nm excitation. Reproduced with permission [70]. Copyright 2015, Wiley. (e) Raman spectra of a 5 L BP at temperature ranging from 20 to −160 °C. (f) Temperature dependence of A_g^2, B_{2g} and A_g^1 Raman peak positions. (e–f) Reproduced with permission [102]. Copyright 2014, American Chemical Soceity.

occurs between bands with opposite parities because photons carry parity of −1. The second rule determines that only those bands having the same eigenvalue of M_y can undergo polarized absorption. In other words, the electromagnetic field of the normal incident light needs to remain sign-unchanged under mirror reflection. As a result, the optical transition polarized along the *y*-axis is prohibited because the electromagnetic field of *y*-polarized light switches signs under M_y operation. Theoretically, this polarization-dependent absorption covers a wide continuous range from 0.33 eV to 3.0 eV [105].

Li et al. observed remarkable above-bandgap absorption peaks from 2 to 5 L BP. They display a redshift trend as BP becomes thicker, namely, the first resonance peaks from 2, 3, 4, and 5 L located at 2.44, 1.93, 1.52, and 1.16 eV, respectively, and the second ones from 4 and 5 L are at 2.31 and 1.94 eV, respectively [101]. The high-energy resonances resemble the anisotropic polarization dependence of the lowest-energy transition. The higher subbands optical transitions result from the interband transitions between higher subbands and can be ascribed to the layer–layer interactions arising from perpendicular quantum confinement.

4.2.4.2. Anisotropic PL spectra. The anisotropic optical properties of BP are revealed by the PL spectra. A detailed polarization-resolved PL spectroscopic study of monolayered BP was conducted by Wang et al., who demonstrated nearly perfect linear dichroism due to the large quantum confinement effect [34]. The PL spectra shows a single peak with a full-width at half-maximum (FWHM) of 150 meV at 1.3 eV, which is strongly polarized along the *x*-axis regardless of excitation polarization indicating the excitonic nature of the emitted light (Fig. 12b&c). The peak PL intensity follows the $\cos^2\theta$ rule with polarization angle θ as shown in Fig. 12c. Because the carriers are more mobile along the lighter effective mass direction, that is, the AC direction along the *x*-axis, the isotropic Coulomb interaction tends to bind the excitons along the *y*-axis giving rise to the observed highly polarized light emission. Li et al. observed highly anisotropic PL spectra from 1 to 5 L BP attributable to the same symmetry cause as discussed for the absorption spectra [101].

4.2.4.3. Anisotropic Raman spectra. The Raman spectra of BP exhibit strong in-plane anisotropy [119–123] which can be utilized to determine the crystal orientation of BP thin films in an all-optical, rapid, and non-destructive way. The measurement configuration is illustrated in Fig. 12d [119]. The intensities of the three typical Raman modes, A_g^1, B_{2g} and A_g^2, are sensitive to both the polarization angle α and sample orientation angle θ [119]. Based on the anisotropic Raman spectra in Fig. 12e, the lattice orientation can be identified as follows. The B_{2g} mode can be filtered out in parallel (α = 0°/180°)/perpendicular (α = 90°/270°) polarization configurations when either the AC or ZZ direction is along the laser polarization one. To further distinguish these two directions, the A_g^2 intensity or A_g^2/A_g^1 ratio can be checked in the

parallel configuration, since the A_g^2 intensity is strongest when the AC direction is parallel to the scattered light polarization while the A_g^1 mode remains unchanged.

Excited by different laser energy, the B_{2g} mode shows the same polarization dependence but the A_g^1 and A_g^2 modes exhibit a different polarization behavior that depends on the excitation wavelengths. The unusual behavior of the Raman modes for angular and wavelength dependence can be interpreted by the complex elements of the Raman tensors, which may arise from the combination effects of the band structure, electron-radiation interaction, and electron-phonon coupling, with the last one still poorly understood and needing further exploration [121,122].

4.2.4.4. Anisotropic photocurrent. The anisotropic polarized light absorption also embodies in the photocurrent and photoconductivity properties. Hong et al. found that in BP FETs, the short-circuit photocurrent, I_{pc}, depends on polarization of the incident light. The maximum magnitude occurs at *x*-polarized excitation giving an anisotropy ratio $[(I_{pc}^{max} - I_{pc}^{min})/(I_{pc}^{max} + I_{pc}^{min})]$ of around 0.3 [106]. To avoid the geometric effect, Yuan et al. designed a ring-shaped electrode acting as the current collector as shown in Fig. 12f [105]. In contrast to a straight-edge metal electrode, the isotropic round photocurrent collector avoids linear polarization that may originate from a straight metal edge. The spatial map of the photocurrent at 1500 nm excitation shows larger photocurrent response under illumination along the *x*-axis (0°) than along the *y*-axis (90°) (Fig. 12f). The linear dichroic photocurrent is the direct result of polarization-dependent absorption that arises from the intrinsic anisotropy of BP. Moreover, the polarization-sensitive photo response covers a broad range from 400 nm to 1700 nm with a large contrast ratio (3.5) between the photoresponsivity along the two orthogonal polarizations. The photocarrier dynamics was studied by He et al. using the pump-probe method which identified that the diffusion coefficient, *D*, along the ZZ direction was about 16 times smaller than that along the AC direction and the carrier lifetime, τ, was

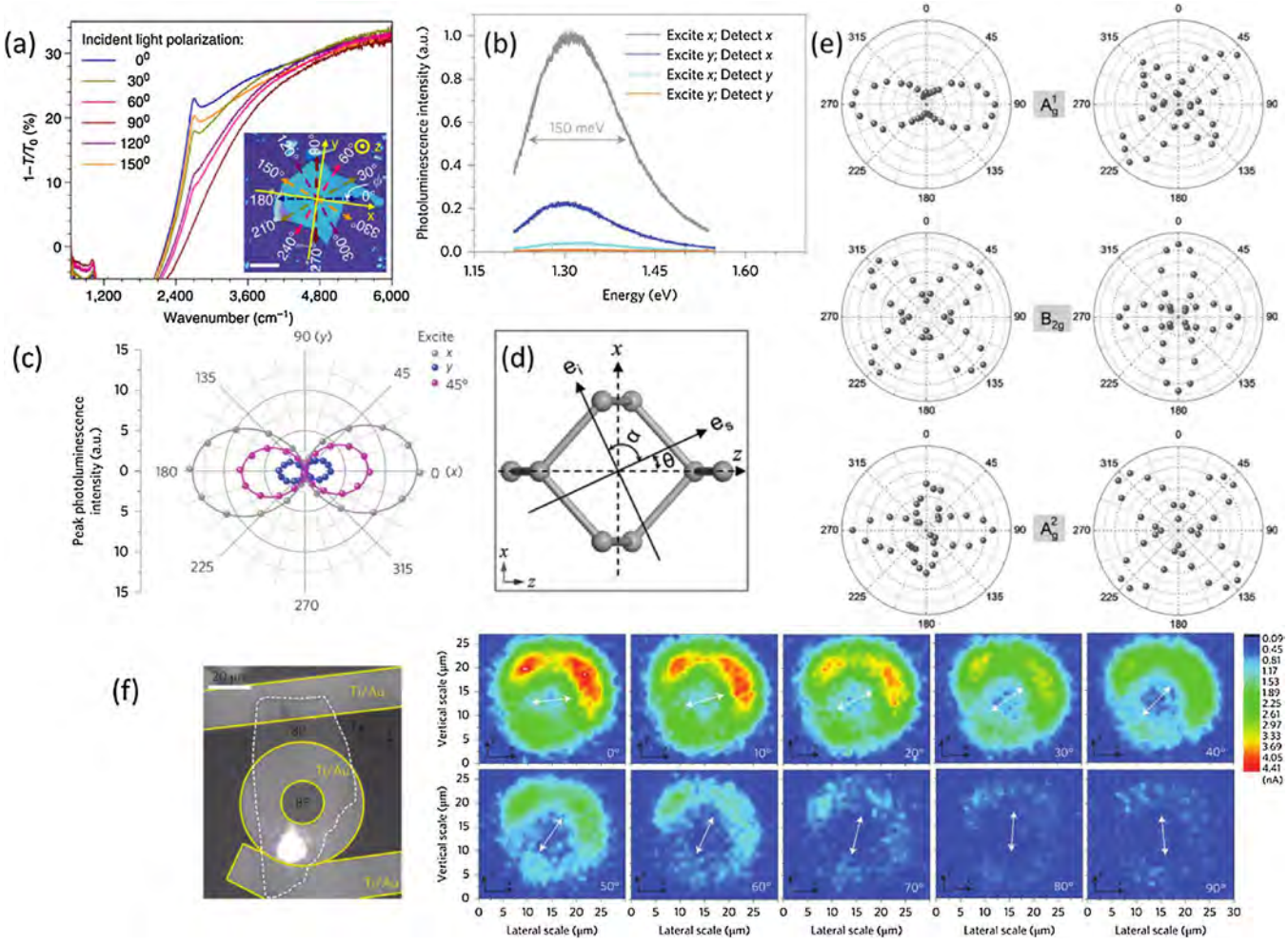

Fig. 12. Anisotropy of optical properties in BP. (a) Polarization-resolved infrared relative extinction spectra when light is polarized along the six directions as shown in the inset. Inset: optical image of a BP flake with a thickness of ~30 nm. Scale bar: 20 μm. Reproduced with permission [31]. Copyright 2014, Nature Publishing Group. (b) Polarization-resolved PL spectra of monolayer BP. The excitation 532 nm laser is linearly polarized along either x (gray) or y (blue) directions. On the detection side, either the x- or y-polarized PL emission are selected, leading to a total of four different combinations as shown. (c) PL peak intensity as a function of polarization detection angle for excitation laser polarized along x (grey), 45° (magenta) and y (blue) directions. Solid lines are fitted curves using a $\cos^2\theta$ function (θ denotes the angle between the x-axis and the polarization detection angle). (b–c) Reproduced with permission [34]. Copyright 2015, Nature Publishing Group. (d) Configuration of the angle-resolved polarized Raman measurements. e_i and e_s are the polarization vectors of incident and scattered light. (e) Polar plots of the fitted peak intensities of A_g^1, B_{2g} and A_g^2 Raman modes as a function of sample rotation angle (θ) under (left column) parallel and (right column) cross-polarization configurations. (d-e) Reproduced with permission [119]. Copyright 2015, Wiley. (f) Polarization-resolved photocurrent. (Left): optical image of a BP photodetector with a ring-shaped photocurrent collector. Areas indicating by yellow lines are Ti/Au electrodes and the area enclosed by a white line is the BP flake; (right): Photocurrent microscopy images of the BP inside the inner ring under illumination at 1500 nm with different light polarizations (white arrows). Reproduced with permission [105]. Copyright 2015, Nature Publishing Group. (For interpretation of the references to colour in this figure legend, the reader is referred to the web version of this article.)

around 100 ps thus yielding anisotropic diffusion lengths [$(D\tau)^{1/2}$] of about 1 and 4 μm along the ZZ and AC directions, respectively. Meanwhile, the relaxation rate of photocarriers was not affected by pump polarization indicating an isotropic carrier relaxation process [107].

4.3. Electric transport properties

4.3.1. Electrical conduction

The electrical properties of bulk BP have been investigated for decades [14,29] but electrical transport in atomically thin BP sheets has only been studied recently since the reports on BP FETs by Liu et al. and Li et al. in 2014 [20,21]. They reported a large hole mobility of ~987 $cm^2/V\,s$ from 10-nm-thick BP devices at room temperature and it is superior to those of TMDs and even silicon-based devices [60]. Meanwhile, the current on-off ratio exceeding 10^5 is four orders of magnitude larger than that of graphene (Fig. 13a). It is evident that BP bridges the gap between graphene and TMDs-based devices from the perspective of the mobility/on-off ratios [13] and the mobility and on-off ratios depend on the thickness [20,21,108]. As shown in Fig. 13a, the drain current modulation decreases monotonically with increasing thickness, whereas the mobility peaks at 10 nm and decreases slightly afterwards (197 and 55 $cm^2/V\,s$ for 8 and 5 nm samples, respectively). Liu et al. also reported that the 4–6 nm transistors showed the best trade-off between higher hole mobility and better switching behavior [20].

4.3.2. Carrier mobilities

In high-quality BP FETs, the temperature-dependent field-effect mobility (μ_{FE}) and Hall mobility (μ_H) display band-like transport features. The mobilities increase with decreasing T and are then saturated at low temperature as shown in Fig. 13b [83]. The initial increasing region indicates that the dominant scattering mechanism is electron-phonon scattering and obeys the inverse power law of $\mu \sim T^{-\gamma}$. γ is measured to be 0.57 and 0.69 for 8-nm- and 15-nm-thick BP, respectively, as shown in Fig. 13b. In contrast, in the saturation region, impurity scattering is the major limiting factor for the carrier mobility.

The charge transport properties are related to the anisotropic electronic band structure which confines particles to an effective 1D environment along the AC direction. The carrier mobility is proportional to m^* with the correlation $\mu = q\tau/m^*$, where q is the elementary electron charge and τ is the scattering time. Ultrafast infrared spectroscopy performed on thin BP flakes discloses that τ is almost isotropic for different scattering directions and so the anisotropic effective mass becomes the major factor that determines the carrier mobility [107]. Qiao et al. applied the phonon-limited model to simulate carrier mobilities along different directions in few-layer BP. The electron mobility (μ_e) and hole mobility (μ_h) along AC are near twice those along ZZ for holes and four times for electrons. The charge transport anisotropy was confirmed experimentally by Xia et al. using angle-resolved conductance (and Hall) measurements, which showed that carriers favored the lighter mass direction and consequently, the conductance σ (and μ_h) along AC was 1.5 (and 1.8) times larger than those along ZZ in 8–15 *nm* BP flakes [31]. Fig. 13c shows the angle-resolved Hall mobilities from 10 K to room temperature obtained from BP thin flakes with thicknesses of 8 and 15 nm. The hole concentration was fixed at $6.7 \times 10^{12}\ cm^{-1}$. With regard to the 15 nm (8 nm) BP flake, the hole mobility along the x-axis exceeds 600 $cm^2/V\,s$ (400 $cm^2/V\,s$) at room temperature and is above 1000 $cm^2/V\,s$ (600 $cm^2/V\,s$) at 120 K. However, for the monolayered system which has only been investigated theoretically, μ_e along the ZZ direction is about 13 times greater than that along the AC direction. In contrast, μ_h along ZZ is 16–38 times smaller than that along AC, making the AC direction more hole conductive despite the larger m_h^* [30].

4.3.3. Quantum oscillations

Quantum oscillation measurements are carried out for BN-BP heterostructures or BN-BP-BN encapsulation systems to confirm the high carrier mobilities and provide the platform for the observation of Shubnikov de Haas oscillations (SdHOs) from thin BP flakes (Fig. 13d&e) [83,109–113]. The oscillating longitudinal resistance ΔR_{xx} is described by the Lifshitz-Kosevich formula for 2D systems: $\frac{\Delta R_{xx}}{R_{xx}} \propto \frac{\Delta}{\sinh\lambda} \cdot e^{-\lambda_D} \cdot \cos(\phi)$, where $\lambda = \frac{2\pi^2 k_B T}{\hbar\omega_c}$, $\omega_c = \frac{eB}{m^*}$ is the cyclotron frequency, m^* the cyclotron mass, k_B the Boltzmann's constant, E_F the Fermi level and $\lambda_D = \frac{2\pi^2 k_B T_D}{\hbar\omega_c}$, T_D is the Dingle temperature given by $k_B T_D = \hbar/2\pi\tau$ where τ is the carrier lifetime, and ϕ is the phase difference between the spin-up and spin-down Landau levels (LLs) [110]. For simplicity, the amplitude can be decomposed into three decay factors, *i.e.*, $R(B, T) = R_T R_D R_S$, which contains substantial information about the carrier effective mass, carrier life time, and spin of the charge carriers. The first parameter, R_T, yields the cyclotron effective mass of holes $m_h^* = 0.34\,m_0$ ($V_g = -80$ V) and electrons, $m_e^* = 0.47\,m_0$ ($V_g = 100$ V) [110]. It is noted that the cyclotron masses obtained this way are different from different groups, but they are always considered to take the geometric mean of the values along the AC (x) and ZZ (y) directions, $m^* = (m_x^* m_y^*)^{1/2}$, which agrees well with theoretical calculation [83,109–113]. The analysis of the second factor, R_D, yields carrier lifetime of 0.12 ps and 0.11 ps for electrons and holes, respectively [110]. The last factor, R_S, originates from Zeeman spin splitting. Li et al. estimated the g-factor based on the global Berry phase extracted from the Landau fan diagram obtaining an upper bound for holes of 2.94 and lower bound for electrons of 2.13 [110]. Gillgren et al. observed two sets of the oscillation frequencies between 3 K and 4.5 K at 12 T. They ascribed the doubled oscillation frequency to Zeeman splitting and estimated the g-factor to be 1.8–2.7 using the simple relationship $g\mu_B B \sim k_B T$ [113]. Long et al. confirmed the spin splitting-induced doublet oscillation frequency by FFT analysis and revealed two oscillation frequencies of $f_1 = 87.6\,T$ and $f_2 = 175.4\,T$ [109]. Derivation of more precise values of the g-factors will be discussed in the following section.

4.3.4. Quantum hall effect

With local back gate tuning, Li et al. unraveled the 2D nature of the negatively-gated thin BP flakes with holes being confined in a 2-nm quantum well (~2 atomic layer) along the out-of-plane direction. This 2D BP system together with the exceptional carrier mobility enables observation of the quantum Hall (QH) effects in both the electron and hole-doped regimes [109,111]. Under a high magnetic field and low temperature, the energy levels are quantized to LLs. By shifting the Fermi level with fixed LLs or by tuning the LLs gap while the Fermi level remains unchanged, the Fermi level alternatively crosses the LLs and passes through the energy gap and then the Hall resistance R_{xy} exhibits the quantized plateaus at $(\upsilon e^2/h)^{-1}$ (where integer υ is the LL filling factor) accompanied by the vanishing longitudinal resistance R_{xx}, as shown in Fig. 13d [111]. Li et al. observed the QH effect from the lowest $\upsilon = 1$ QH states at the extreme quantum limit [111]. The QH states revealed at both even and odd υ indicates that the two-fold spin degeneracy is fully lifted.

The energy gaps of the QH states at odd and even υ are determined by the cyclotron energy $E_c = \hbar eB/m^*$ and Zeeman spin-splitting energy $E_z = g\mu_B B$, where $\mu_B = e\hbar/2m_0$, is the Bohr magneton. For the 2D hole gas (2DHG) of BP, the holes sequentially fill up the LLs with the odd υ associated with E_z and energy gap expressed

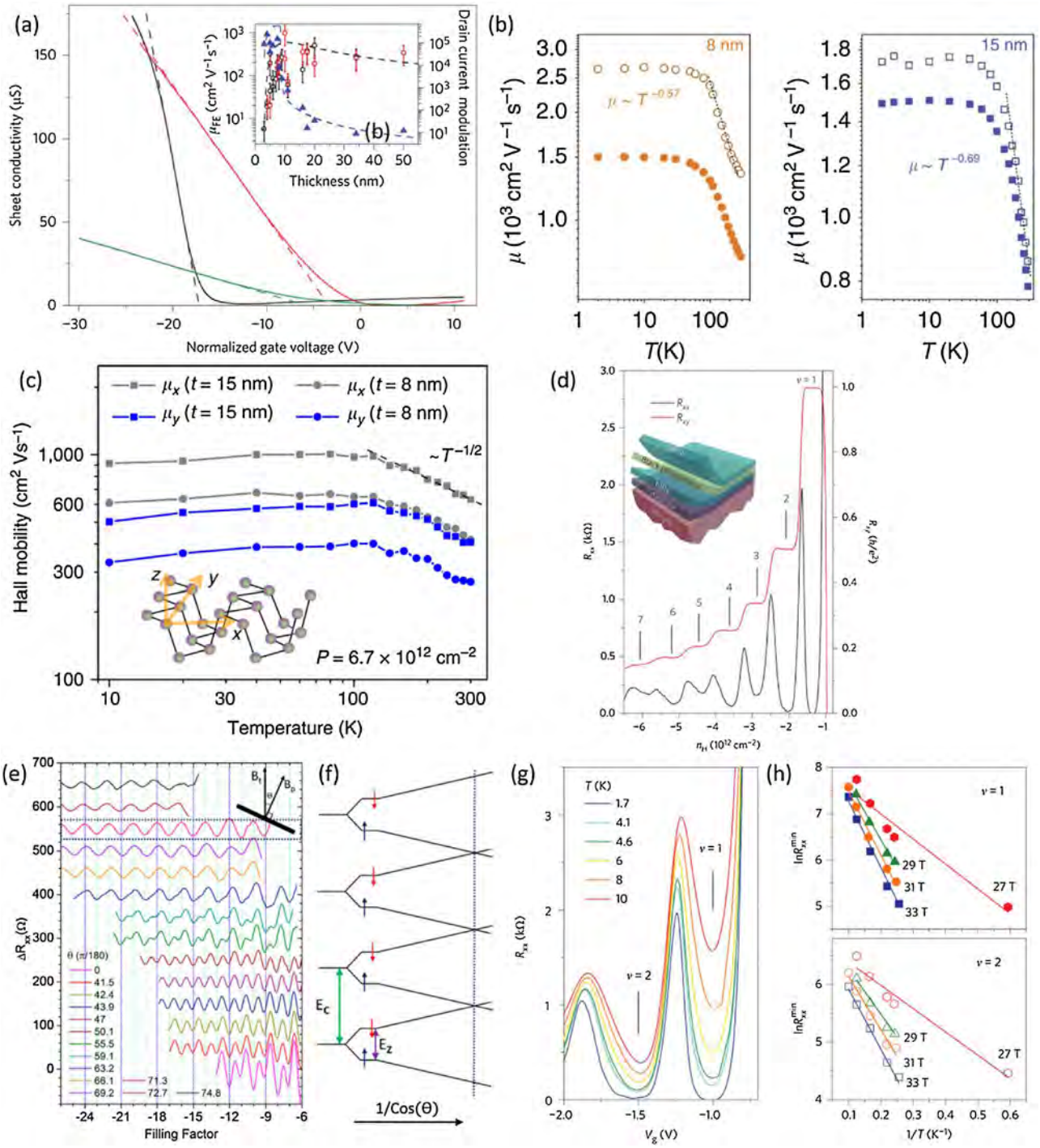

Fig. 13. Electrical transport characteristics of BP thin flakes. (a) Sheet conductivity measured as a function of gate voltages (V_g) for devices with different thickness: 10 nm (black), 8 nm (red) and 5 nm (green). Field-effect mobilities are extracted from the line fit of the linear region of the conductivity (dashed lines). Inset: Summary of drain current modulation (filled blue triangles) and carrier mobility (open circles) of BP FETs with varying thickness. Reproduced with permission [21]. Copyright 2014, Nature Publishing Group. (b) Temperature dependent field-effect mobility (open circles) and Hall mobility (solid dots) at −70 V V_g of 8 nm (left) and 15 nm (right) BP sample. Reproduced with permission [83]. Copyright 2014, Nature Publishing Group. (c) Hall mobilities measured at a constant hole doping centration along the x and y directions for BP thin flakes with a thickness of 8 and 15 nm, respectively. Inset: schematic view of a single layer BP showing the crystalline directions. Reproduced with permission [31]. Copyright 2014, Nature Publishing Group. (d) Hall resistance (black) and magnetoresistance (red) as a function of carrier density obtained at B = 33 T and T = 1.7 K in BP thin flakes sandwiched with BN layers. (e) SdHOs in BP thin flakes with varying tilt angles at B = 14 T. Dashed lines indicate the SdHOs at the LL coincidence event. (Inset): magnetic field alignment in the measurements. (f) Schematic fan diagram describes the LLs evolution in the tilted magnetic field. Green arrows: cyclotron energy $E_c = \hbar eB\cos\theta/m^*$. Purple arrows: Zeeman gap $E_z = g\mu_B B$. Blue and red arrows: up- and down-spin of the charge carriers, respectively. Dashed line: LL coincident event ($E_c = E_z$). (e–f) Reproduced with permission [109]. Copyright 2014, American Chemical Society. (g) R_{xx} measured as a function of gate voltage with various temperatures under 33 T. (h) The R_{xx}^{min} is plotted as a function of 1/T on a log scale, for low-υ QH states (υ = 1 and 2). (d,g,h) Reproduced with permission [111]. Copyright 2014, Nature Publishing Group. (For interpretation of the references to colour in this figure legend, the reader is referred to the web version of this article.)

as $\Delta E_{odd} = E_z - \Gamma$, where Γ is the thermal broadening of the LLs and the energy gap for even υ is $\Delta E_{even} = E_c - E_z - \Gamma$ [110]. Therefore, the more precise g-factor in the 2DHG BP systems can be determined by determining the energy gap. It is mainly conducted by two different experimental methods: (1) Gate-dependent R_{xx} minimum, R_{xx}^{min} and (2) Tilt-angle dependent SdHOs.

The first method is usually adopted to identify the g-factor of low-υ QH states under a large magnetic field (>30 T). The energy gap can be characterized by monitoring the amplitude of R_{xx}^{min} originating from thermal activation, $R_{xx}^{min} \sim exp(-\Delta E/k_B T)$, as shown in Fig. 13g&h. Li et al. obtained an exchange-interaction-enhanced $g \sim 4.2 \pm 1.5$ at the extreme quantum limit $\upsilon = 1$ and 2 and $g \sim 4$ at $\upsilon = 3$ and 4 from the Arrhenius plot illustrated in Fig. 13h [111]. Long et al. estimated the enhanced g-factors to be 2.7 ± 0.3 and 2.5 ± 0.3 for $\upsilon = 5$ and 7, respectively [114].

The second method takes the advantage that E_z scales with the total field B_t, while E_c depends solely on the perpendicular field component $B_\perp = B\cos\theta$, where θ represents the tilt angle with respect to the normal direction of the sample plane as shown in Fig. 13f [109]. The measurement is performed in two ways. Long et al. monitored the frequency component of the SdHOs, that is, by changing θ, and LLs reach coincidence $E_c = E_z$ with vanishing even-to-odd υ which is experimentally marked by the disappearance of one of the SdHO components (Fig. 13e). In this method, Long et al. reported a g-factor of 2.47 which was largely enhanced by the exchange interaction between the spin with opposite directions [109]. In contrast, Li et al. set the relative amplitude of the oscillations between odd and even υ, $\Delta R_{odd}/\Delta R_{even}$, as the indicator of the relative energy gaps, $\Delta E_{odd}/\Delta E_{even}$. The $\Delta R_{odd}/\Delta R_{even}$ crossing 1 happened when $\Delta E_{odd} = \Delta E_{even}$ at the proper θ. The resulting g-factors obtained are ~2 for $\upsilon = 5$ to 15 and in comparison to Long's work, suggest negligible exchange enhancement [111].

4.4. Thermal properties

4.4.1. Phonon dispersion

In contrast to electrons, phonon dispersions in BP exhibit an entirely opposite feature. For the optical modes, the phonon bands are more dispersive along the ZZ direction and accordingly faster transport of phonons than that along the AC direction [115] (Fig. 14a). For the acoustic phonon modes, the larger group velocity along the ZZ direction leads to anisotropic thermal transport since these modes typically carry most of the heat [115,116] (Fig. 14a). The orthogonal electrical and thermal anisotropy enables asymmetrical transport of electrons and phonons thus offering new opportunities and concepts for designing new devices.

4.4.2. Thermal conductivity

First-principles calculation predicts that the thermal conductivity in monolayered BP along the ZZ direction (110 $W m^{-1} K^{-1}$) is two or three times higher than that along the AC direction (36 $W m^{-1} K^{-1}$) [124–127]. In particular, the thermal transport is mainly accomplished by phonons since the electronic contribution is minor (3 $W m^{-1} K^{-1}$). Experimentally, the thermal conductivity of bulk polycrystalline BP is found to be 10 $W m^{-1} K^{-1}$ at room termperature with no anisotropic effects [128]. With respect to few-layer BP with defined symmetry axes, micro-Raman and time-domain thermoreflectance have been employed to determine the anisotropic in-plane thermal conductivity [33,116]. Luo et al. performed thermal conductivity measurements on freestanding few-layer BP by micro-Raman scattering [33] in which the laser served as a local heat source to soften the atomic bonds and cause non-harmonic phonon coupling to produce a change in the optical phonon frequency and red-shift of the Raman peaks. The temperature-dependent Raman shift can be utilized as a thermometer to monitor thermal conduction in BP (Fig. 14b) [33]. The

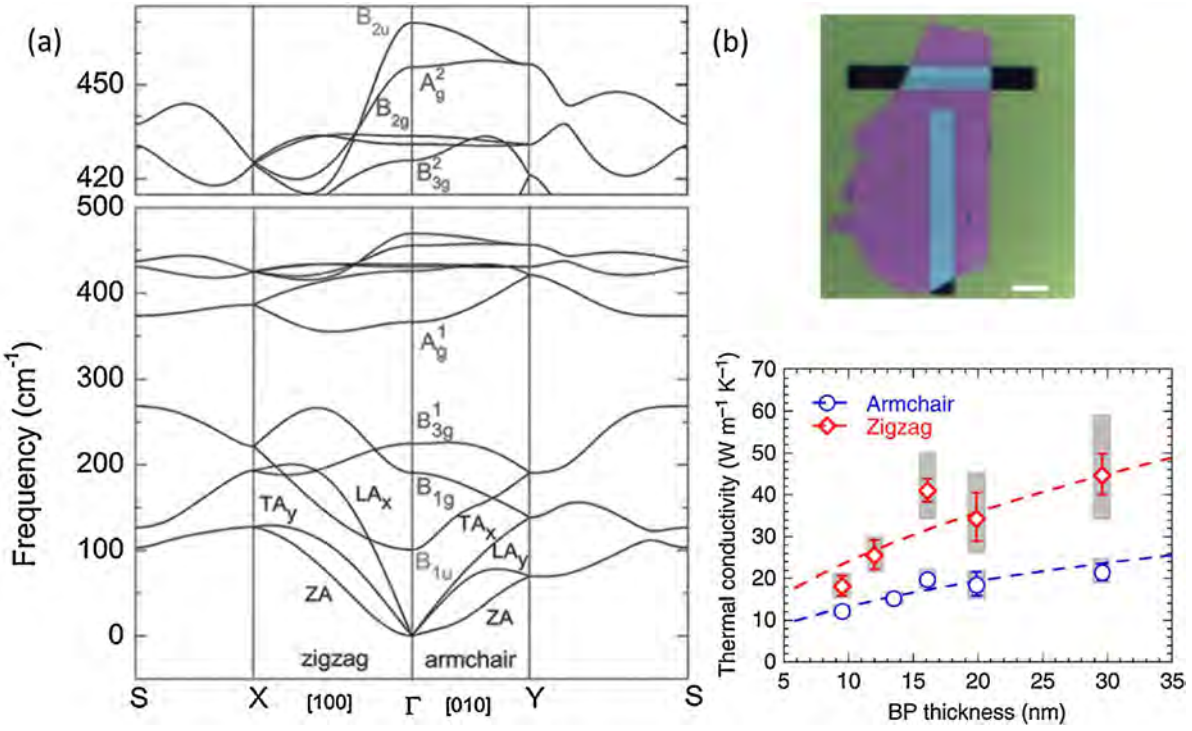

Fig. 14. Anisotropic thermal properties of BP. (a) Phonon dispersion of phosphorene. The suffix to the longitudinal acoustic (LA) and transverse acoustic (TA) branches denotes the polarization direction of the modes. ZA: out-of-plane acoustic mode. Reproduced with permission [115]. Copyright 2015, Wiley. (b) Thermal conductivity of BP measured with micro-Raman technique; (top) optical image of the ~16-nm-thick BP suspended on slits. Scale bars, 5 μm. (Bottom) AC (blue) and ZZ (red) thermal conductivities of multilayer BP films. Dashed lines are fitted results with theoretical modeling. Reproduced with permission [33]. Copyright 2015, Nature Publishing Group. (For interpretation of the references to colour in this figure legend, the reader is referred to the web version of this article.)

BP flakes are first transferred to the pre-defined slits and the excitation laser is focused to become a nearly 1D heat source to ensure that heat conduction is most sensitive to the thermal conductivity perpendicular to the slits. The pair of T-shape slits guarantee that both the ZZ and AC thermal transport can be individually investigated on the same BP. The thermal conductivities along the AC and ZZ directions for the thicker suspended BP membrane (>15 nm) are $20\,W\,m^{-1}\,K^{-1}$ and $40\,W\,m^{-1}\,K^{-1}$. They decrease sharper to $10\,W\,m^{-1}\,K^{-1}$ and $20\,W\,m^{-1}\,K^{-1}$, respectively, for thinner samples (~9.5 nm) due to strong surface phonon scattering.

The significant differences in the bandwidths and group velocities of low-frequency acoustic phonons (<4 terahertz (THz)) between the ZZ and AC directions are responsible for the strong anisotropy of thermal conductivity in BP. Moreover, the phonon lifetime and mean free path (MFP) of the acoustic phonons are shorter along the ZZ direction than AC direction and it is another factor for the significant anisotropy. In few-layer BP, diffusive surface scattering suppresses the contribution of long-MFP phonons resulting in a smaller anisotropy ratio between the two directions [33]. To avoid perturbations from the oxidized surface, Jang et al. determined the thermal transport properties of AlO_x-passivatied BP flakes using the time-domain thermoreflectance method [116]. They obtained higher in-plane thermal conductivities of 86 ± 8 and $34 \pm 4\,Wm^{-1}\,K^{-1}$ along the ZZ and AC directions, respectively, due to the overlying AlO_x layer that mitigated ambient deterioration. All in all, BP is useful in thermoelectric applications on account of the high electrical conductivity and low thermal conductivity especially along the AC direction.

4.5. Mechanical properties

The anisotropy of BP produces unique mechanical properties [35,129–131]. First-principles calculation shows that mono-layer BP can sustain strain up to 27% along the ZZ direction and 30% along the AC direction thereby demonstrating good mechanical flexibility [130]. These strain limits arise from the puckered structure which is effectively flattened under tensile strain along the AC direction, while the P–P bond lengths are negligibly extended. The Young's modulus of BP was experimentally determined to be 58.6 ± 11.7 GPa along the ZZ direction and 27.2 ± 4.1 GPa along the AC direction using the AFM bending method [35]. This trend is in good agreement with theoretical prediction [130]. The anisotropic Young's moduli also originate from the puckered structure of BP which unfolds under tension and folds under compression along the AC direction. Similarly, calculation shows that the elastic modulus is larger along the ZZ direction due to the easily changed bond angles. Besides, an intrinsic negative Poisson's ratio is predicted in the out-of-plane direction under uniaxial strain parallel to the pucker in monolayer BP by first-principles calculation [132]. Wang et al. studied the mechanical resonance in drumhead freestanding BP devices using analytical modeling and numerical simulation [133]. The thick sample (>100 nm) in the elastic plate regime exhibits pronounced mechanical anisotropy manifested as higher resonance modes through the mode shape and sequences.

4.6. Biocompatibility

BP possesses a distinct advantage in biocompatibility compared to other 2D materials. Phosphorus is an essential element making up about 1% of the total human body weight. BP being the most stable allotrope of phosphorus degrades naturally into to non-toxic phosphite, phosphate, and other P_xO_y species under physiological conditions [38]. The biodegradable and biocompatible characteristics have been exploited therapeutically.

Recent studies have provided solid evidence that BP with different sizes are biocompatible with various cell or animal models. In 2015, Pumera et al. assessed the toxicological profile of BP using human lung carcinoma epithelial cells (A549) as the model. This early study demonstrates that the cytotoxicity of BP is concentration dependent, and BP is less toxic than graphene oxide (GO) at the same concentration [134]. Fu et al. carried out a more thorough investigation on the cytotoxicity of BP with different sizes in human normal hepatocyte (LO2) and the samples showed excellent biocompatibility [135]. These preliminary findings suggest that BP has large potential in biomedical and therapeutic applications.

5. Applications

5.1. Transistors

Transistors are the fundamental components in modern electronic and integrated circuits. As a new member of 2D materials, BP not only inherits merits such as excellent flexibility, dangling bonds free, and immunity to short-channel effects at the scaling limit [11], but also have unique advantages make it promising in 2D nanoelectronics. Two of the parameters of BP FETs, mobility and on-off ratio, have been reported to be about $1000\,cm^2/V\,s$ and 10^5, respectively, at room temperature [21]. Unlike graphene without a bandgap, well-defined current saturation can be achieved from BP FETs due to the finite gap. These features are beneficial to the design and construction of transistors with low off-state power dissipation and high on-state power gain, which are crucial to the realization of high-speed logic circuits and high-frequency power amplifiers. BP possesses ambipolar transport properties, meaning that n- and p-type doping can be readily implemented to design CMOS FETs [26,28,136,137]. Moreover, the unique in-plane anisotropic transport properties foster the design of novel BP electronic devices [13].

5.1.1. Field-effect transistors

FETs based on 2D semiconductors with both high mobility and on-off ratios are in great demand for modern nanoscale electronic devices. Recent work on BP FETs focusing on the figures of merits is summarized in Table 1.

5.1.1.1. Dielectric screening. Since charge carriers in atomically BP films are weakly screened, the carrier mobility is sensitive to the interfaces on both sides of the semiconductors. This has inspired investigation of the role of the substrate and dielectric environment pertaining to electrical transport in BP transistors. For the top side of the flake, the surrounding high-κ dielectric layer can provide a large-energy barrier to confine electrons in the nanoscale semiconductor membrane [138]. Indeed, since BP is unstable at ambient atmosphere, air exposure increases the threshold voltage, degrades the on-off ratio and mobility, and causes hysteresis in output curves [40]. The performance deterioration may arise from surface oxidation or charge transfer to trapping sites in ambient adsorbates. Hence, conformal ALD growth of the HfO_2 or Al_2O_3 capping layer, which is commonly used in graphene or TMDs FETs, can protect both the edges and top surfaces from humidity, oxygen, and adsorbates to suppress the degradation process [88]. Moreover, these insulating layers can serve as the gate dielectrics. To monitor the influence of capping layers including Al_2O_3, HfO_2, BN, and so on, scanning microwave microscopy which measures the local conductivity of the buried BP layers with good spatial resolution has been applied [88,139]. The local resistance of the thin-cap BP

Table 1
BP based FETs and their performances. t: thickness; L: channel length; –: no related information. The mobilities were recorded at room temperature unless otherwise stated.

t (nm)	L (μm)	Gate dielectric	μ_{FE} (cm^2/V s)	On/off ratio	ref
10	**1.0**	SiO_2 (back)	$\mu_h \sim 286$	10^4	[20]
8	**1**	SiO_2 (back)	$\mu_h \sim 300$	10^4	[31]
2	**1**	SiO_2 (back)	$\mu_h \sim 50$	5×10^5	[31]
10	**–**	SiO_2 (back)	$\mu_h \sim 984$	10^5	[21]
8	**2.6**	SiO_2 (back)	$\mu_h \sim 197$	10^5	[21]
5	**4.5**	SiO_2 (back)	$\mu_h \sim 55$	10^5	[21]
15	**3**	HfO_2 (top)	$\mu_h \sim 413$	2×10^3	[141]
1.9	**2**	SiO_2 (back)/Al_2O_3 (top)	$\mu_h \sim 172$ $\mu_e \sim 38$	2.7×10^4 (h) 4.4×10^3 (e)	[26]
15	**2.7**	Polyimide (back)/Al_2O_3 (top)	$\mu_h \sim 310$, $\mu_e \sim 89$	10^3–10^4	[156]
13	**0.5**	Polyimide (back)/Al_2O_3 (top)	$\mu_h \sim 233$	10^2	[154]
<10	**0.02**	Al_2O_3 (top)	$\mu_h \sim 17$	$>10^2$	[150]
12		PMMA(top)/SiO_2 (back)	$\mu_h \sim 1150$	10^5	[21]
10	**2.4**	BN (back)/Cu adatoms	$\mu_h \sim 690$, 1780 (7 K) $\mu_e \sim 380$, 2140 (7 K)	–	[146]
5	**2**	SiO_2 (back)/Al adatoms/Al_2O_3 (top)	$\mu_h > 2150$ (120 K) $\mu_h > 1495$ (260 K)	$>10^5$ (120 K) $>10^3$ (260 K)	[147]
~43	**–**	PMMA/MMA(top)/SiO_2 (back)	$\mu_h \sim 900$ (0.3 K)	$> 10^5$ (180 K)	[112]
~5	**2**	SiO_2 (back)/ionic liquid (top)	$\mu_h \sim 510$	1.4×10^4	[28]
10.7 ± 0.8	**0.17–0.55**	HfO_2 (back)	$\mu_h \sim 44$	1.2×10^3	[142]
13	**–**	SiO_2 (back)	$\mu_h \sim 950$, $\mu_e \sim 950$	$>10^5$	[145]
5.6	**–**	graphite/BN (back)	$\mu_h \sim 400$, 3900(1.5 K) $\mu_e \sim 83$, 1600 (1.5 K)	–	[110]
~10	**–**	graphite/BN (back)/BN (top)	$\mu_h \sim 920$ $\mu_h \sim 7100$ (4 K)	–	[111]
~10	**–**	BN (back)/BP (top)	$\mu_h \sim 400$ $\mu_h \sim 4000$ (1.6 K)	10^5	[113]
~8	**10**	BN (back)/BP (top)	$\mu_h \sim 1350$, 2700 (1.7 K)	10^5 (300 K) $>10^8$ (1.7 K)	[83]
–	**–**	BN (back)/BP (top)	$\mu_h \sim 5200$, 45000 (2 K)	–	[109]

changes with time, indicating that it primarily suffers from electrical degradation initiated from the uncovered edges while the physical integrity is preserved [88]. In contrast, the thick-cap BP (10 nm HfO_2 or 25 nm Al_2O_3) shows better stability in a span of several weeks [88,139]. Kim et al. developed a double-layer passivation scheme by spin-casting a hydrophobic fluoropolymer flake on the thick-cap Al_2O_3 layer to get rid of moisture adsorption and diffusion to the BP layer achieving month-long stability in air [88]. Simple spin-coating of the PMMA/MMA superstrate can also eliminate the photo-oxidation and protect the BP sample during annealing at 170 °C [112].

If the high-κ dielectric layer is composed of ionic liquids or gels, the ultrahigh capacitance of the electrical double layer allows for a small operation voltage in the BP FETs. Wide-range tunability of the Fermi level offers the possibility to determine the bandgap of the 20 nm BP band gap to be 0.35 eV according to the transfer curve (Fig. 15a) [28]. The supercapacitance can also accumulate a large density of charge carriers up to 10^{14} cm^{-2} on the surface of the semiconductor [140]. The ultra-high carrier density provides a platform for fundamental studies on BP thin flakes, for instance, metal-insulator-transition and superconductivity. Saito et al. observed the transition of BP thin flakes from insulating to metallic for both electron and hole channels [28]. However, unlike TMDs [140], the superconductivity of BP thin flake has not yet been detected by ion-gating, probably due to insufficient accumulation of electrons or restriction that the superconductivity can only be induced in monolayered BP [28].

As the unstable nature of BP leads to easy oxidization during ALD, some groups have used mechanically exfoliated BN flakes as the capping layers to passivate BP thin flakes without a chemical precursor treatment. Doganov et al. first compared the charge transport properties of BN protected and exposed BP FET devices (Fig. 15b) [41]. AFM and Raman spectroscopy disclose the robust physical integrity of the passivated area with time as shown in the inset in Fig. 15b. The electron mobility is improved by 10 to 100 times with the BN protected channel and produces a symmetrical ambipolar behavior. It has also been pointed out that the charge traps at the interface between BP and SiO_2 is responsible for the hysteresis observed from both the exposed and covered regions.

For the bottom side, the high-κ HfO_2 and Al_2O_3 are used as back gate dielectrics in BP FETs apart from SiO_2 [141,142]. Back gated with the HfO_2 layer grown by a low-temperature CMOS process, the BP FETs exhibit a near ideal subthreshold swing of 69 mV/dec and high hole mobility exceeding 400 cm^2/V s at room temperature [141]. To further improve the device performance, ultra-flat BN is used as the substrate to provide the disorder-free interfaces on both sides. By adopting the all-dry and polymer-free vdW transfer technique that has been applied to graphene and TMDs [143,144], high-quality BN-BP-BN interfaces are formed and the typical device fabrication process is illustrated in Fig. 15c. This sandwiched structure reduces interface scattering from substrate phonons and charge traps and increases screening from impurities giving rise to a hole mobility of 5200 cm^2/V s at room temperature [109]. The encapsulated devices can be operated for more than 300 h under ambient conditions and tolerate high-temperature annealing at 500 °Cs to suppress the charge trap states, thereby eliminating the hysteresis effect in the transfer curves of the BP FETs [83,113].

5.1.1.2. Contact engineering. On account of the lack of controllable and sustainable doping schemes for 2D semiconductors, contact resistance management is problematic and to solve this issue, researchers have utilized contact metals with the appropriate work function to inject the desired types of carriers into the respective bands. In BP transistors, the Schottky barrier heights are associated with the work function of the contact metals stemming from Fermi level pinning at the metal/BP interface [27]. Hence, small-contact resistance p-type dominant FETs can be produced by using a metal with a large work function such as Pd and Cr [27,114,145] and n-

type ones can be formed with a metal with a small work function such as Ti, and Al [26,136,145]. The high/low-work-function metals can match the VBM/CBM to lower the Schottky barrier height, decrease the contact resistance, and facilitate injection of holes/electrons. As shown in Fig. 15d, the unipolar *n*-type BP FETs (3–5 layers) were fabricated by Perello et al. with Al as the metal contact and the unipolar nature turned into symmetrical ambipolar characteristics when the BP thickness was increased to 13 nm [145]. The *n*-type BP transport feature was realized by doping with metal adatoms (Cu, Al, . . .) [146,147]. The Schottky barrier height which was 200 meV in Ti/Au BP FETs could be reduced to less than 50 meV with TiO_2/Cu contacts and the proper gate voltage (V_g) [103]. However, if there was a strong Fermi-level-pinning effect in the BP thin flakes, even Sc contacts, the low-work function metal

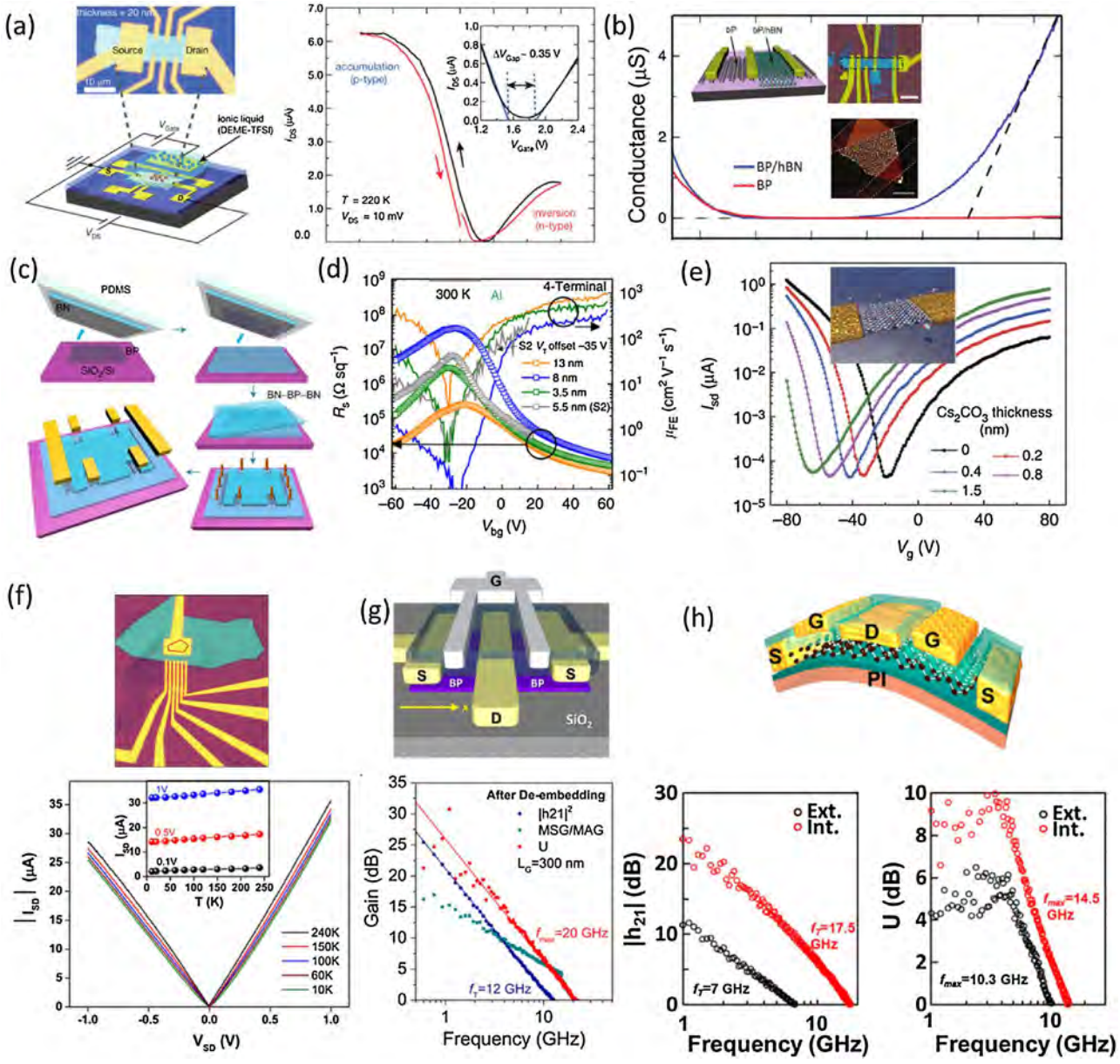

Fig. 15. BP transistors. (a) Optical image (left top), schematic view and the transfer curve of a BP FET with ionic liquid gate. The inset shows a magnified image of the threshold voltage to extract an energy gap of ~0.35 eV. Reproduced with permission [28]. Copyright 2015, American Chemical Society. (b) Four-terminal transfer curves of the BN-passivated and exposed BP FETs (~4.5-nm-thick). Dashed line is the linear fit of field-effect mobility. Inset: (top left) schematic drawing of the device geometry; (top right) optical image of a typical device with outlines of the BP film (black line) and passivating BN layer (blue line). Scale bar: 3 μm; (bottom) AFM image of partly graphene-covered BP after 24 h exposure to ambient conditions. Scale bar: 4 μm. Reproduced with permission [41]. Copyright 2015, Nature Publishing Group. (c) Schematic of the BN-BP-BN heterostructure device fabrication process. Reproduced with permission [83]. Copyright 2015, Nature Publishing Group. (d) Sheet resistance (open points) and field-effect mobilities (solid lines) for different thickness BP FETs. Reproduced with permission [145]. Copyright 2015, Nature Publishing Group. (e) Transfer curves of BP FET with varying Cs_2CO_3 coating thickness from 0 to 1.5 nm. Inset: schematic of BP device coated with Cs_2CO_3. Reproduced with permission [152]. Copyright 2015, Nature Publishing Group. (f) (Top) Optical image of the graphene-contacted (stripe area) BP (red polygon) FET covered with BN (green area). (Bottom) Temperature-dependent output characteristics of the graphene-contacted BP devices (~4.5-nm-thick). Inset: temperature dependence of the bias current at different source-drain biases. Reproduced with permission [82]. Copyright 2015, American Chemical Society. (g) (Top) Schematic of the BP radio-frequency transistor structure. (Bottom) The short-circuit current gain h_{21}, maximum stable gain (MSG)/maximum available gain (MAG), and unilateral power gain U of the 300-nm channel length device after de-embedding. Reproduced with permission [153]. Copyright 2014, American Chemical Society. (h) Schematic of flexible BP THz transistor structure. (Bottom) Intrinsic (extrinsic) cutoff frequency f_T and maximum oscillation frequency extracted after (before) de-embedding. Reproduced with permission [154]. Copyright 2016, American Chemical Society. (For interpretation of the references to colour in this figure legend, the reader is referred to the web version of this article.)

with the Fermi level above the CBM of BP gave rise to a pronounced *p*-type feature because the Fermi level was pinned close to the VB [148]. On the heels of successful creation of barrier-free contacts with graphene electrodes in TMDs [149], Avsar et al. transferred this technique to BP FETs with Ohmic contacts by taking advantage of the tunable work function of graphene and good compatibility between different 2D materials [82]. The pre-patterned graphene stripes transferred to BP flakes served as the source/drain electrodes and a layer of BN covered the top for protection as shown in Fig. 15f [82]. The nearly temperature insensitive source-drain current observed from the graphene-contacted BP FETs suggests Ohmic charge injection. In the devices, the Schottky barrier heights are negative (ranging from −17 to −2.5 meV) implying a transparent interface for current injection from the graphene electrodes to BP thin flakes.

5.1.1.3. Ambipolar behavior. Although the p-type characteristic and corresponding hole transport have been extensively studied, BP transistors possess intrinsic ambipolar characteristics depending on top dielectric layer capping [83,], channel length scaling [27,150], high temperature annealing [83,113], ionic-liquid gating [28,151], and contact engineering [26,145]. The ambipolar behavior is always asymmetrical with relatively lower mobility and concentration of electrons, which may originate from the higher activation energy for electrons than holes. To balance the *n*- and *p*-type transport feature, the surface decorated with low work function materials such as $CsCO_3$ and MoO_3 were used to tune the doping level in BP to enhance electron transport. By controlling the thickness of Cs_2CO_3, the symmetrical ambipolar behavior was observed as shown in Fig. 15e [152].

5.1.1.4. High-frequency performance. The good current saturation properties of BP FETs offer advantages over graphene in terms of voltage and power gain, thereby making BP a desirable candidate in radio-frequency (RF) nanosystems. Wang et al. demonstrated the operation of BP FETs on SiO_2 in the gigahertz frequency range (Fig. 15g) [153]. The standard calibration and de-embedding processes were carried out to yield a unity current gain cutoff frequency f_T of 12 GHz and maximum oscillation frequency f_{max} of 20 GHz in the 300 nm channel-length device. The BP RF FETs prepared on a on flexible polyimide substrate show f_T of 17.5 GHz and f_{max} of 14.5 GHz for a channel length of 500 nm (Fig. 15h). The flexible RF FETs are mechanically robust and can tolerate tensile strain up to 1.5% without deterioration of the device performance [154].

5.1.2. Functional circuit blocks

Device merits such as the high mobility, strong current saturation, and moderate on-off ratio have spurred research interests in BP with regard to digital and analog nanoelectronics. Realization of some basic and essential functional circuits such as the logic inverter, analog amplifier, and frequency doubler, which are building blocks for large-scale integration, appeals to the modern semiconductor industry.

5.1.2.1. CMOS inverter. During the early investigation of BP transistors, it was found that the excellent *p*-type transport behavior should complement *n*-type semiconductors in CMOS logic circuits. Liu et al. constructed a CMOS inverter with 5 nm thick MoS_2 as NMOS and 5 nm thick BP as PMOS [20]. The mobility difference between MoS_2 and BP are balanced by choosing the appropriate channel lengths to control the length/width ratio of the NMOS and PMOS. This CMOS inverter which is operated at 1 V (V_{DD}) shows obvious voltage transfer characteristics from V_{DD} to 0 (V_{in}: −10 to 2 V) with a maximum gain of 1.4. Similar CMOS inverters combining BP and MoS_2 but with a buried HfO_2 back gate have been demonstrated and show a maximum gain of 3.5 at 2.5 V V_{DD} and consistent operation over a wide temperature range at frequencies up to 100 kHz [155]. The ambipolar behavior of BP transistors enables implementation of an all-BP-based CMOS inverter [26]. Here, Ti is the contact metal in the ambipolar BP FETs and two splitting gate electrodes are applied onto the Al_2O_3 capping layer to produce *n*- and *p*-type doping in the BP layer. The combined BP NMOS and BP PMOS forms a fully complementary logic inverter with a maximum gain of about 8 and an almost ideal noise margin of 2.5 V for V_{DD} = 5.0 V. As shown in Fig. 16a, the CMOS inverter can also be constructed by selectively implementing *n*-doping in a part of the BP thin flakes by addition of Cu adatoms and it does not require different contact metals or local electrostatic gating [146]. The inverter exhibits a gain of 46 and noise margin exceeding 30% of V_{DD} and it can be further optimized by introducing other metal adatoms like Au adatoms for *p*-doping.

5.1.2.2. Analog amplifier. The ability of operating at gigahertz frequencies enables BP FETs to be analog signal amplifiers. Zhu et al. fabricated inverting (common-source) and non-inverting (common-gate) voltage amplifiers on a flexible polyimide substrate [156]. For both configurations, the small-signal gain is |8.7| with opposite polarity arising from the almost symmetrical ambipolar characteristics of the BP FETs. By virtue of the large capacitance of ionic liquids, Das et al. constructed a small-signal analog amplifier based on a single BP flake serving as both the load resistor and switching FET, in which the transistor region was locally ion-gated (Fig. 16b). The gain of the amplifier was 9 without output distortion for input frequencies up to 15 kHz [151].

5.1.2.3. Amplitude-modulated demodulator. The ambipolar charge transport characteristics of BP FETs offer the opportunity for the fabrication of BP amplitude-modulated (AM) demodulators. Zhu et al. developed a flexible BP AM demodulator in which the baseband audio signal (5 kHz) was amplitude-modulated onto a carrier frequency (55 kHz) as input to the gate terminal as shown in Fig. 16c. The demodulated output shows an expected square-law quadratic dependence on the input signal as shown in Fig. 16d [156]. Although the conversion gain is lower than that of graphene, the BP AM demodulators show lower DC power dissipation due to the smaller off-current.

5.1.2.4. Esaki diodes. In conventional FETs, the thermionic limited subthreshold swing requires at least 60 mV to increase the current by one order of magnitude at 300 K [157]. The idea of tunneling FET avoids this limit by utilizing the band-to-band-tunnelling mechanism to reduce the leakage current and power supply voltage without performance loss. The Esaki diode, which is the heart of a tunneling FET, was realized with the vdW heterostructures by vertical stacking of BP and $SnSe_2$ thin flakes and these two layered semiconductors possessed a broken-gap energy band alignment (Fig. 16e) [158]. A robust negative differential resistance (NDR) under forward bias was observed at room temperature with a peak-to-valley ratio of 1.8 at 300 K and 2.8 at 80 K as shown in Fig. 16f. The weak temperature-dependent NDR indicates that electron tunneling dominates the current transport in agreement with theoretical modeling. Fabrication of the Esaki diode suggests that the 2D vdW heterostructure is promising in tunnelling-based devices.

5.1.3. Flexible devices

Another important application of 2D BP is flexible devices. Flexible BP FETs and the circuit blocks based on them have been realized on polyimide substrates with two layers of Al_2O_3 serving as the bottom gate dielectrics and top encapsulation. The BP devices show a maximum carrier mobility of 310 cm^2/V s [156] that

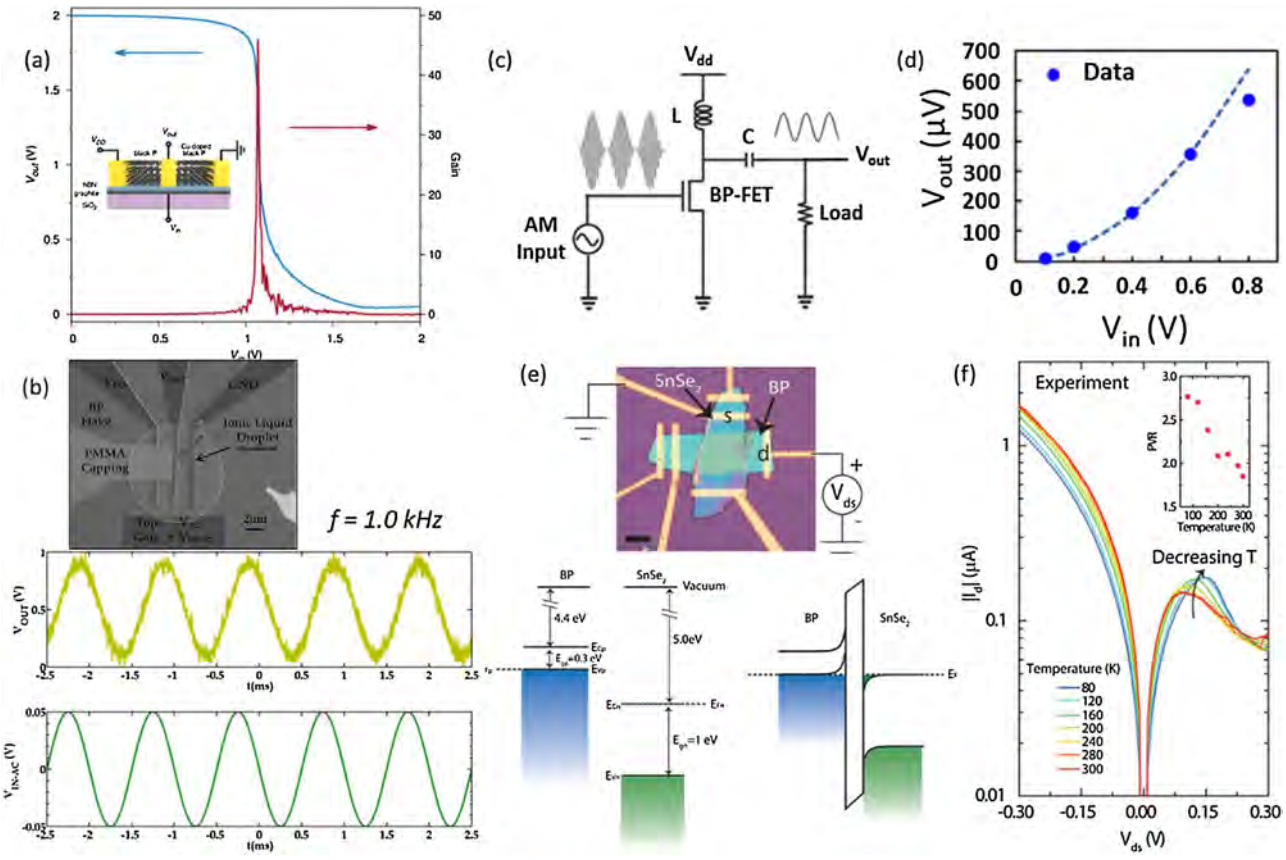

Fig. 16. Functional circuit blocks based on BP transistors. (a) Output voltage, V_{out}, versus the input voltage, V_{in} (V_{DD} = 2 V), of the CMOS inverter based on a single 7-nm BP. The right axis shows the inverter gain. Inset: schematic of the BP CMOS inverter fabricated using an untreated PMOS and a Cu-doped NMOS. The graphite/BN bottom gate serve as V_{in}. Reproduced with permission [26]. Copyright 2014, American Chemical Society. (b) (Top) False color image of a small signal amplifier based on few layer BP with ionic liquid gating. (Bottom) Signal amplification at 1.0 kHz of the small signal amplifier. Reproduced with permission [151]. Copyright 2014, IEEE. (c) Schematic of an ideal AM demodulator based on BP FET operating at ambipolar point. (d) Dependence of demodulated baseband output (5 kHz sinusoid) on the input carrier signal (55 kHz sinusoid). The symbols are the measured results, consistent with the square-law quadratic relation indicated by the dashed line. (c-d) Reproduced with permission [156]. Copyright 2015, American Chemical Society. (e) (Top) Optical image of an Esaki diode based on the BP-$SnSe_2$ vdW heterostructure. (Bottom) Energy band alignment of BP-$SnSe_2$ junction before and after contacting each other. (f) Temperature dependent current-voltage characteristics of the BP-$SnSe_2$ Esaki diode. Inset: Peak-to-valley ratio as a function of temperature. (e–f) Reproduced with permission [158]. Copyright 2015, American Chemical Society.

is more than five times larger than that achieved with flexible TMD transistors [156]. These devices also feature mechanical robustness and the mobility, on-off ratio, and hysteresis are only slightly affected at uniaxial tensile strain up to 2%. The mechanical robustness can be further improved with flexible gate dielectric layers such as BN and organic insulators. Additionally, both the BP transistors and functional circuit blocks exhibit excellent device endurance under repetitive apply-and-release processes for 5000 bending cycles [156,154].

5.1.4. Chemical sensors

2D BP is promising for gas sensing due to the large surface-to-volume ratio and high sensitivity to the surroundings [159–164]. Adsorption of gas molecules and subsequent charge transfer between BP increase the conductance which can be utilized to monitor gas exposure. First-principles calculation shows that BP is more sensitive to nitrogen-based toxic gases such as NO and NO_2 due to stronger binding to these gas molecules [162]. Exposure to NO_2 has been studied using *p*-doped BP similar to TMDs [165]. Abbas et al. observed a conductance change of 2.9% from the BP transistors when exposing to 5 ppb NO_2 and they are more sensitive than MoS_2 devices [160]. The conductance increases monotonically and follows the Langmuir isotherm as the NO_2 concentration is increased from 5 to 40 ppb. Cui et al. revealed that the sensitivity depended on the thickness and the optimal BP thickness for NO_2 detection was 4.8 nm in agreement with the theoretically predicted values between 4.3 and >10 nm [162]. By means of electrochemical impedance spectroscopy, BP thin films have been shown to detect methanol vapor in the presence of interferences such as toluene, acetone, chloroform, dichloromethane, ethanol, isopropanol, and water. The detection limit is 28 ppm which is far below the approved exposure limit of 200 ppm [163]. A humidity sensor capable of selective detection of water vapor based on liquid exfoliated BP flakes has been developed by Yasaei et al. [164]. When the relative humidity is varied from 10% to 85%, the drain current of the BP sensor increases by about 4 orders of magnitude. The sensitivity is superior to other reported values for humidity detection. These sensors are also very stable and do not show performance degradation after 3 months under ambient conditions.

5.2. Optoelectronic devices

Boasting thickness-dependent direct bandgaps spanning the visible to near-infrared (NIR) range, large exciton binding energy, and strong light-matter interaction, 2D BP is promising in optoelectronics. In this section, we review recent BP optoelectronic applications and compared the performance with that of other 2D materials.

5.2.1. Photodetectors

A photodetector is a key component in optoelectronics to convert light information to electrical signals that can be readily processed by standard electronic systems. In 2014, Buscema et al. characterized the photo-response of ultrathin (3–8 nm) BP FETs [166]. The device shows optical response from the visible region up to 940 nm with a cutoff wavelength of 997 nm and rise time of 1 ms. These are superior to those reported from photodetectors based on MoS_2 [167], WS_2 [168], GaSe [169], and GaS [170], suggesting that BP is more suitable for broadband and fast photodetection. Huang et al. improved the responsivity in a broadband range from 400 to 900 nm to 7×10^6 A/W at 20 K and 4.3×10^6 A/W at 300 K by shrinking the channel length to 100 nm [171]. The BP FETs also show good ability in mid-infrared photodetection [105,172], in which the external responsivity is as large as 82 A/W at 3.39 μm and it is capable of performing low power detection in the picowatts range (Fig. 17c) [172]. Wu et al. demonstrated the capability of BP in an ultraviolet (UV) photodetector with high responsivity and specific detectivity up to 9×10^4 A/W and 3×10^{13}, respectively [173]. The UV photoresponse is attributed to the resonant-interband transition between two specially nested valence and conduction bands giving rise to a large density of states and efficient ultraviolet absorption (Fig. 17b).

The photocurrent generation mechanisms of BP-based photodetectors are mainly classified into three categories: photothermally induced photothermoelectric effect (PTE) and bolometric effect, photovoltaic effect (PVE), and photogating effect (PGE).

5.2.1.1. Photothermally driven effects based. Low et al. systematically studied the origin of the photo-response of thick (>20 nm) BP phototransistors [174]. The photocurrent is dominated by the photothermally driven thermoelectric and bolometric processes, both of which produce photocurrents with the same polarity opposite to the PVE induced current as shown in Fig. 17a. In PTE process, local laser illumination produces the temperature gradient between the metal electrodes and BP channel to form effective thermocouples at the metal-BP junction. The PTE is the major cause of photo-response at zero and low drain bias [106,174,175], which generates current extends to micrometers away from the metal contacts suggesting a long thermal decay length in the BP device channel [174]. In the high drain bias cases, the PTE is overwhelmed by the bolometric effect. That is, laser heating affects the carrier mobility or density that modifies the electrical conductivity. Engel et al. built a bolometric effect based BP photodetector (~120-nm-thick) to record diffraction-limited images with high-visibility in both the visible (532 nm) and NIR (1550 nm) range (Fig. 17e) [176]. The resolution is 270 nm and 720 nm for 532 nm and 1550 nm illumination, respectively, being consistent with the modeled values with the point spread functions.

5.2.1.2. Photovoltaic effect based. The photocurrent generated by PVE arises from separation of the photo-generated e-h pairs by the built-in electric fields at the Schottky or PN junctions or external electric fields by applying a drain-source bias (V_{ds}). Hong et al. performed scanning photocurrent microscopy on an 8-nm BP FET and revealed that in the on-state, the photocurrent was mainly attributed to PTE but in the off-state is PVE [106], PVE was dominant at low doping concentrations [174,175]. In the thin BP devices, the reduced screening effect offers the opportunity to tune the doping level and photocurrent generation mechanism in BP phototransistors. Besides, there are several other device strategies employing PVE in photodetection, for example, the photodiode structure based on a PN junction.

Building on the ambipolar properties of BP, Buscema et al. constructed an artificial PN junction with two splitting electrostatic gates [177]. As shown in Fig. 17f, different parts of the single BP flake are separately modulated to opposite doping regimes by the splitting gate voltage. This BP channel can be defined as a PN junction showing the PVE response with the short-circuit current/open-circuit voltage and rectifying I_{ds}–V_{ds} behavior (Fig. 17f). A large signal-to-noise ratio is ensured due to the small dark current and the responsivity reaches the maximum value of 28 mA/W under 532 nm light excitation. Employing the ionic gel as the gate dielectrics, Yuan et al. constructed a vertical PN junction by inducing and confining electrons at the surface of BP while holes were distributed in the deeper bulk regime [105]. The vertical built-in electric field dissociates the photo-induced charge carriers leading to a maximum responsivity of 1.5 mA/W under 1700 nm light excitation. Apart from the physical method, Lu et al. developed a chemical method to create a functional junction *in situ* on the device to improve the device performance [178]. The BP flake is selectively and partially oxidized with a scanning focused laser beam. Owing to the "photovoltaic-like" effect, the photocurrent is largely enhanced at the BP/oxidized BP junction giving rise to a responsivity of 3.4×10^3 A/W.

Integration of BP with other 2D materials enables the assembly of vdW PN junctions for optoelectronic applications. Deng et al. constructed PN diodes by vertically stacking the CVD grown monolayered MoS_2 and mechanically exfoliated BP thin flakes [179]. The photodiodes exhibit strong gate-tunable rectifying I_{ds}-V_{ds} characteristics and photovoltaic energy conversion ability with a peak EQE of 0.3%. As a photodetector, this *p-n* diode exhibits responsivity up to 3.54 and 418 mA/W under forward and reverse biases, respectively, which are superior to those of BP phototransistors. Ye et al. vertically stacked mechanical exfoliated MoS_2 and BP thin flakes to build a vdW PN photodetector showing responsivity (specific detectivity) of 22.3 A/W (3.1×10^{11}) at 532 nm and 153.4 mA/W (2.13×10^9) at 1550 nm for a rapid response time of 5 μs, thus demonstrating the good photodetection capability in both the visible and NIR regions (Fig. 17g) [180]. Chen et al. fabricated the WSe_2-BP heterostructure to tune the PP or NN junction with the gate voltage [181]. The current rectification ratio is 2.5×10^3 for the PP junction but decreases to a negligible value of 1 for the NN case. Moreover, the EQE of the WSe_2-BP junction is improved showing 2.7% and 3.1% for the PP and NN configurations, respectively.

5.2.1.3. Photogating effect based. In nanostructured materials like 2D semiconducting BP, the PGE prevails due to the large surface and reduced screening [182]. In PGE, if the photo-generated electrons/holes are trapped by the local states, they act as a local gate to modulate the conductivity of the BP channel. In this scenario, the photocarrier lifetime is only limited by recombination of the trapping states and the saturation threshold power can be determined by the density of trapping centers. Although a longer photocarrier lifetime introduces a larger photo gain and responsivity, the operation speed is compromised [182]. The instability of BP leads to the formation of a native oxide layer on the surface under ambient conditions and it is naturally full of mid-gap trapping states that dominate the photo-response of BP phototransistors under low power excitation [172]. In BP heterostructures, the PGE can be performed by the charge transfer process at the interface between BP and other materials. Liu et al. produced a BP phototransistor on $SrTiO_3$ substrate with a responsivity of 10^5 A/W at 50 K [183]. This structure provides the foundation for the construction of memory devices by the photoconductivity under visible light excitation and it can be erased with pulsed UV light illumination. The key mechanism of the memory device lies in the different penetration lengths of

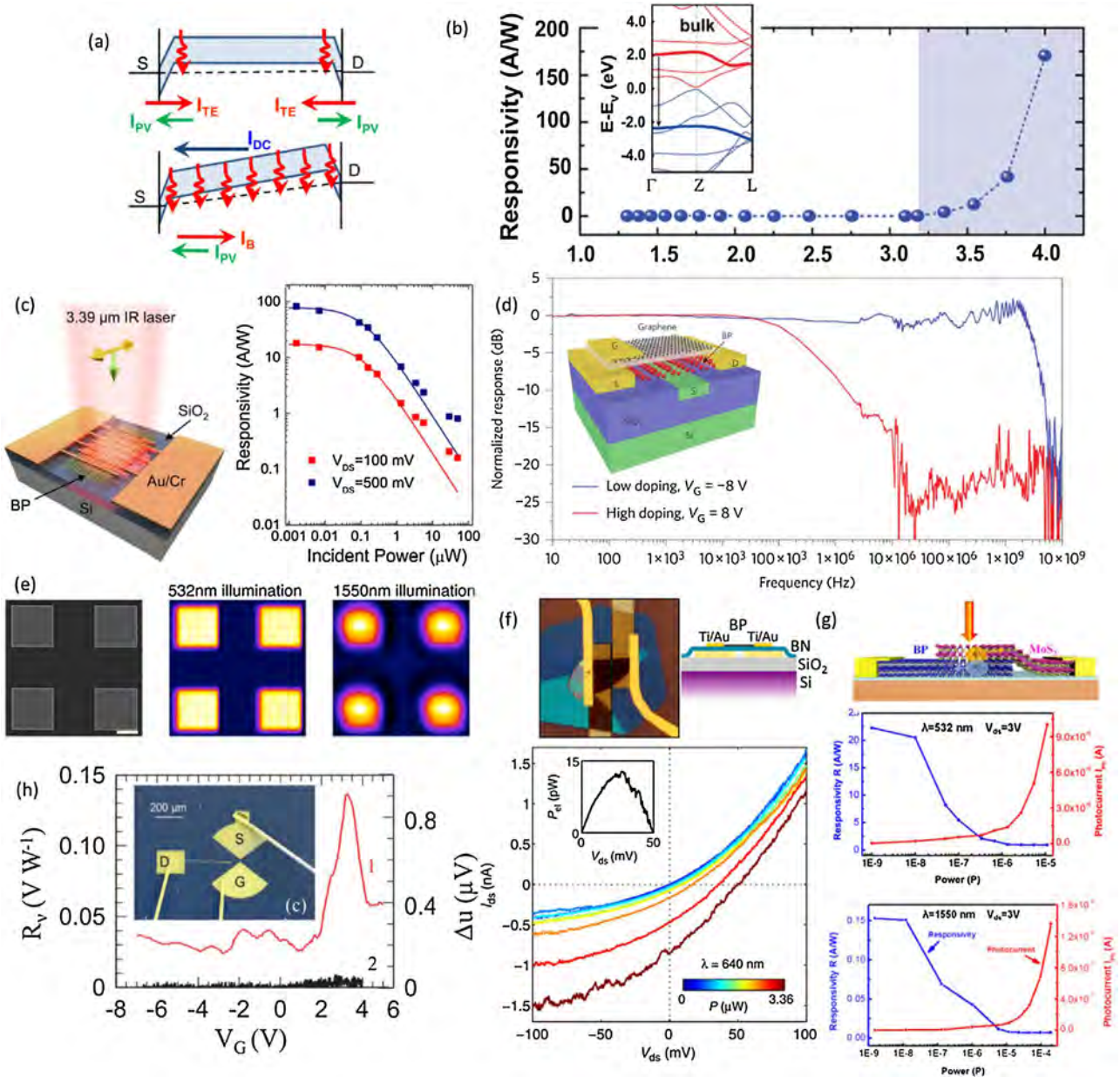

Fig. 17. BP photodetectors. (a) Illustration of photocurrent generation by PTE (I_{TE}), PVE (I_{PV}) and bolometric (I_B) mechanism at (top) zero and (bottom) finite drain bias in BP phototransistor. I_{DC} is the drain-source current following from drain (D) to source (S). Reproduced with permission [174]. Copyright 2014, American Physical Society. (b) Photoresponsivity of BP phototransistor within the energy range 1–4 eV. Inset: BP band structure obtained from first-principle calculations. The arrow indicates the band nesting responsible for the absorption edge in the UV (3–4 eV). Reproduced with permission [173]. Copyright 2015, American Chemical Society. (c) (Left) Illustration of the BP photodetector operating at 3.39 μm. The polarization and the incident directed are indicated by the yellow and green arrows, respectively; (right) power dependent responsivity with (red) 100 mV and (blue) 500 mV drain bias (V_{DS}). Reproduced with permission [215]. Copyright 2016, American Chemical Society. (d) The response of the waveguided-integrated BP photodetector gated at low (blue) and high (red) doping regime. Inset: schematic illustration of the device configuration. Reproduced with permission [175]. Copyright 2015, Nature Publishing Group. (e) (Left) SEM image of the micrograph. These images are acquired with a step of 50 nm at wavelength of 532 nm (middle) and 1550 nm (right). Scale bar, 2 μm. Reproduced with permission [216]. Copyright 2014, American Chemical Society. (f) (Top) Optical image (left) and schematic view (right) of BP PN junction defined by local electrostatic gating; (bottom) Output characteristics in the PN configuration as a function of the incident power (λ = 640 nm). Inset: the electrical power that can be harvested at the maximum employed illumination power. Reproduced with permission [177]. Copyright 2015, Nature Publishing Group. (g) (Top) Schematic of the vdW BP-MoS_2 photodetector under illumination (arrow). The photocurrent (I_{ph}) and photoresponsivity (R) of the BP-MoS_2 heterojunction under optical irradiation of 532 nm (middle) and 1550 nm (bottom) with a series of incident intensities. Reproduced with permission [180]. Copyright 2016, American Chemical Society. (h) Gate dependence of plasma-wave photovoltage (Δu)/responsivity (R_v) (red line) with 0.298 THz irradiation impinging on the BP surface. Black line shows the Δu signals measured while the THz beam was obscuring with an absorber for reference. Reproduced with permission [184]. Copyright 2015, Wiley. (For interpretation of the references to colour in this figure legend, the reader is referred to the web version of this article.)

visible and UV photons. The former penetrates deeply into $SrTiO_3$ and the induced photocarriers can break the built-in electric field at the BP/$SrTiO_3$ interface leading to a larger hole density and conductivity. The PGE with long-term persistence is ensured by the high-energy barrier at the BP/STO interface. In contrast, UV light can only excite the BP/STO interface and it recovers the device to the initial state.

5.2.1.4. High-speed communication. Youngblood et al. integrated the BP FET with a silicon waveguide with few-layer graphene as the

top-gate operating at the NIR telecom band and showing intrinsic responsivity of 135 and 657 mA/W for the 11.5 and 100 nm thick devices, respectively [175]. When gated to the lightly-doped regime, the photocurrent is generated by the PVE with a high response bandwidth exceeding 3 GHz, whereas in the highly *n*-doped regime with the bolometric dominate photocurrent, the cut-off frequency decreases (0.2 MHz) as shown in Fig. 17d. Besides optical communication devices, THz light with deep penetration lengths allows the detection of objects behind opaque barriers with a relatively high spatial resolution [25]. Viti et al. demonstrated a high-speed photodetector operating at 0.298 THz (Fig. 17g). The responsivity and noise equivalent power were 0.15 V/W and 40 nW $Hz^{-1/2}$, respectively [184]. Later, the same group developed a BN encapsulated THz BP photodetector with good air stability and improved responsivity of 0.25 V/W [185].

5.2.2. Ultrafast pulse lasers

By employing BP flakes or BPQDs as the optical saturable absorber (SA) to turn the continuous wave output of the laser into a periodic train of optical pulses, the ultrafast pulse fiber lasers in the main telecommunication band 1.55 μm were produced [186–190]. The output pulse is generated by two methods: Q-switching and mode-locking. The erbium-doped fiber is usually used as the gain medium that is pumped by a laser diode *via* a wavelength division multiplexer.

Li et al. obtained Q-switched pulse output from the fiber laser immediately after inserting the mechanically exfoliated BP SA into the cavity with a length of 11 m (Fig. 18a) [187]. They found the 1100 nm thick BP delivered better performance attaining a stable Q-switching peak at 1532.5 nm at a pumping power 23 mW. When the pumping power was increased from 23 to 55 mW, the pulse repetition rate increased from 26 to 40 kHz and pulse duration was reduced from 9.5 to 3.1 μs because of easier saturation of BP SA with a larger gain provided by the higher pumping power. The pulse energy varied linearly with the pumping power with a maximum value of 18.6 nJ. Chen et al. measured a maximum pulse energy of ~94.3 nJ with a high pumping power of 195 mW [190]. However, they found that the pulse output became unstable when the pumping power exceeded 180 mW and totally disappeared when it was bigger than 195 mW.

With a longer fiber cavity length and generally higher threshold pumping power, the stable mode-locked ultrafast pulse can be self-started by introducing a disturbance [75,187–190]. The soliton-like pulse shape originates from the interplay of group velocity dispersion and self-phase modulation. The output mode-locked pulse at 1558.7 nm with an ultrashort pulse duration of 786 fs has been achieved [187]. Besides the mechanical exfoliated BP flakes, Xu et al. reported that the solvent-prepared BPQDs SA was also suitable for the mode-locked fiber laser (Fig. 18b) [75]. The as-prepared BPQDs dispersion was mixed with the polyvinylidene fluoride (PVdF) and cast on an Al foil. After evaporating at 80 °C for 6 h, the PVdF-BPQDs composites were transferred between two fiber connectors inside the fiber cavity as SA. With a 50 mW pumping power, the BPQDs-mode-locked laser pulse was located at 1567.5 nm with a pulse duration of 1.67 ps, suggesting a real pulse duration of 1.08 ps by fitting the $sech^2$-pulse profile.

5.3. Battery anodes

BP has been a very promising anode material in the Li-ion batteries even before the extensive research on 2D BP crystals [191–194]. Phosphorus is low-cost and abundant in nature. It can react with Li or Na to form Li_3P or Na_3P compounds with a high theoretical specific capacity of 2596 mAh/g at the discharge potential range of 0.4–1.2 V. Therefore, as the most stable allotrope of phosphorous, the crystalline and semiconducting BP is suitable for anode materials in batteries. First-principles calculation shows that the energy barrier (0.08 eV) for Li atoms migrating to monolayered BP sheets along the ZZ direction is smaller than those of graphene and MoS_2, resulting in an ultrafast and directional lithium diffusion into monolayered BP [192]. A

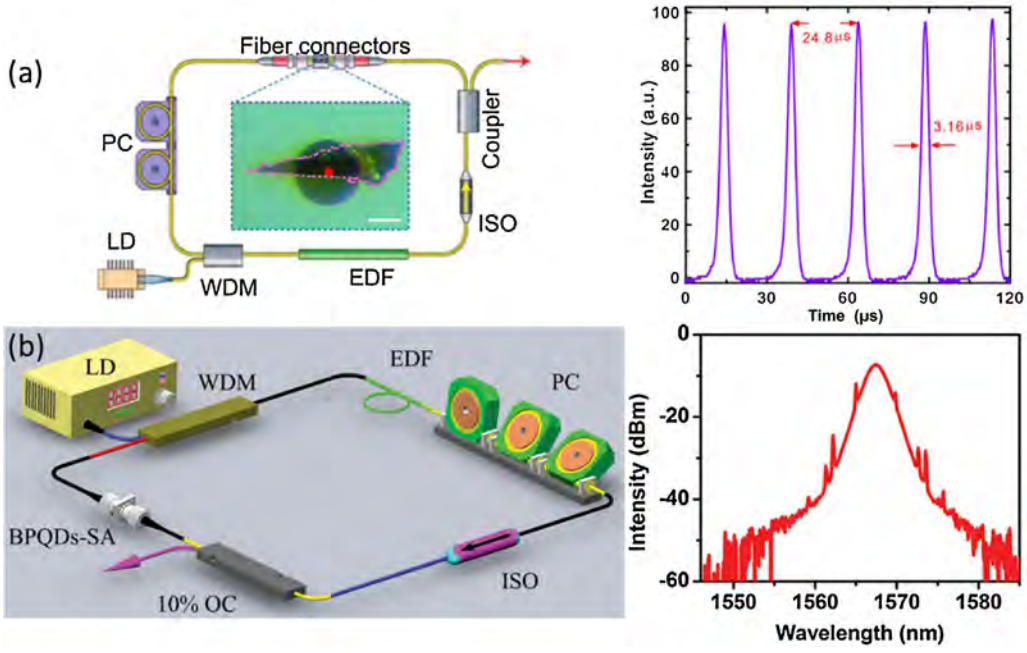

Fig. 18. BP ultrafast laser applications. (a) BP Q-switched fiber laser; (left) schematic of the setup. PC: polarization controller. LD: laser diode. WDM: wavelength division multiplexer. EDF: Erbium-doped fiber. ISO: isolator. Inset: transfer BP flake on the optical fiber end. Scale bar, 60 μm; (right) output pulse train. Reproduced with permission [187]. Copyright 2015, Nature Publishing Group. (b) BP mode-locker fiber laser; (left) schematic of the setup; (right) output spectrum. Reproduced with permission [75]. Copyright 2016, Wiley.

semiconducting to metallic transition can be induced by Li intercalation of BP thin flakes leading to high electrical conductivity.

Using the simple high energy mechanical milling method, the amorphous RP with low electron conductivity can be transformed into small BP particles (100 nm). Park et al. observed from conducting BP anodes high first charging and discharging capacities of 2010 and 1814 mAh/g, respectively [191]. However, the capacity faded rapidly due to the loss of electrical contact caused by the large volume expansion (~300%) upon lithiation. To improve the cycling stability while accessing the full capacity, Sun et al. fabricated BP-graphite composites by high-energy mechanical milling to serve as anodes in Li-ion batteries (Fig. 19a) [193]. This process produces stable P-C (phosphorus-carbon) covalent bonds during the Li insertion/extraction and maintains the good electrical contact between BP and C. These composites deliver high capacity (2785 mAh/g) and excellent cycle life of 100 cycles with 80% capacity retention. Among the carbon materials studied including graphite, graphite oxide, carbon black, and fullerene, graphite is found to be the best choice to achieve a long cycle life and high-rate capability (Fig. 19b) resulting from the contact between BP and carbon particles.

BP nanosheets are a good anode candidate in Na-ion batteries [196–199]. Using first-principles calculation, Kulish et al. showed that the ultrahigh Na diffusivity on BP thin sheets due to the low energy barrier was only 0.04 eV [197]. Similar to Li-ion batteries, a large concentration of Na atoms transforms the semiconducting BP to the metallic phase with increased electrical conductivity thus favoring the charging/discharging process. By mixing the liquid dispersions of BP flakes and graphene, the BP-graphene composites serve as an anode in Na-ion batteries which show a high capacity of 2440 mAh/g and good cyclability with 83% capacity retention after 100 cycles [198]. Dabbi et al. showed that by adding carbonate or vinylene carbonate to the BP-Na cells, the solid electrolyte interface could be stabilized to attain a longer cycling life and higher reversibility with respect to desodiation/sodiation of the BP electrode [199].

In addition to Li/Na ion batteries, nanoscale BP is suitable for electrode materials in solar cells. Yang et al. developed bifacial *n*-type dye-sensitized solar cells (DSSCs) by incorporating ultrasmall BPQDs into a polyaniline (PANI) film to serve as the photocathode [195]. The BPQDs absorb NIR light and facilitate charge transfer, while the dye N719 in the photoanode absorbs visible light. The composite provides wideband light absorption and improved charge transport in the DSSCs (Fig. 19b). The bifacial structure enhances light harvesting producing better photovoltaic performance than traditional front-illuminated DSSCs. The power conversion efficiency of the BPQDs based DSSCs reaches 6.85%

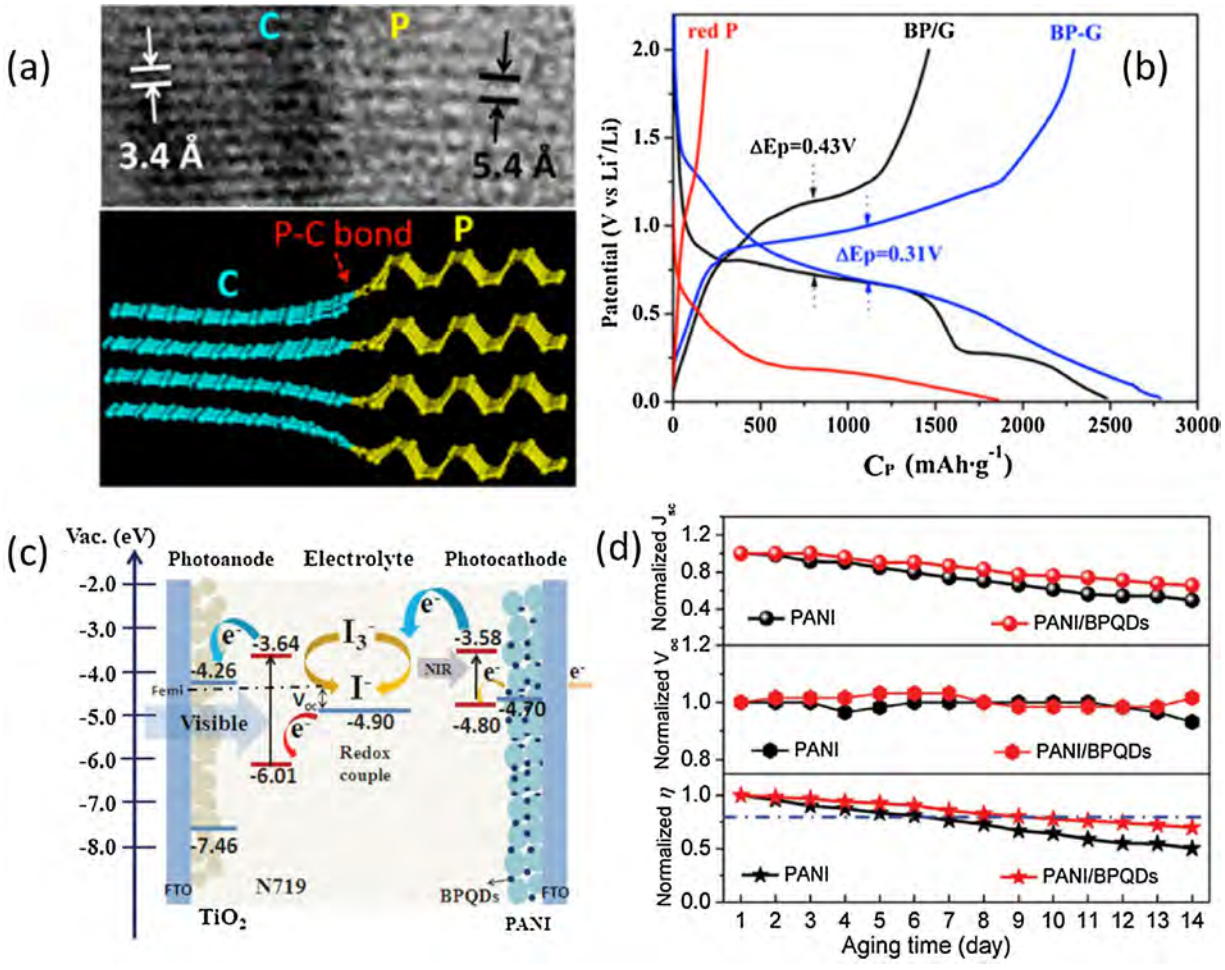

Fig. 19. BP applications in batteries. (a) The HRTEM (top) and schematic (bottom) image of BP-graphene composite. (b) The charge-discharge profiles of BP-fullerene, BP-graphene oxide, BP-carbon black and BP-graphene electrodes at the first cycle between 0.01–2.0 V with a current density of 0.2C. (a-b) Reproduced with permission [193]. Copyright 2014, American Chemical Society. (c) Energy level diagram of the bifacial DSSCs showing light absorption by both the N719 and BPQDs based photocathodes. (d) Stability of J_{sc}, V_{oc} and η with time for the bifacial *n*-type DSSCs based on the PANI and PANI/BPQDs photocathodes under illumination of 100 mW cm^{-2}. Reproduced with permission [195]. Copyright 2016, Wiley.

which outperforms the PANI cathode (5.82%) by almost 20%. The BPQDs/PANI devices also exhibit improved stability after 14 days without sealing (Fig. 19d). In fact, BP is more suitable for cathodes in DSSCs than graphene (5.59%) due to semiconducting nature and enhanced NIR absorption.

5.4. Mechanical resonators

BP possesses attractive mechanical properties such as very large strain limit [130], large Young's modulus [35], and negative Poisson's ratio [132], thereby fostering research of nanoelectromechanical systems to couple high-speed mechanical motion to the electronic and optoelectronic properties [129,133,200]. Wang et al. fabricated drumhead nanoelectromechanical resonators with suspended BP using the dry transfer technique [133] and strong mechanical resonances were observed by optical, electrical as well as the fundamental thermomechanical vibratory measurements from a wide range of geometries (rectangular and circular cavity), lateral sizes, and thicknesses. When the BP thickness is reduced from 120 to 20 nm, the operation regime shows a clear transition from the plate to the membrane limit with the resonance frequency dependence varying from elastic modulus to both the elastic modulus and initial tension. The nanoelectromechanical devices shed light on applications to actuators, sensors, and transducers that leverage mechanical degrees of freedom of semiconducting BP.

5.5. Biomedical applications

5.5.1. Biosensors

The fast development of BP-based sensors for gases/small molecules and their superior sensing performance have inspired application to biomolecule detection. Chen et al. fabricated a few-layer BP-based FET biosensor for antigen-antibody interaction detection with sensitivity in the nanogram range [201]. In this biosensor, mechanically exfoliated few-layer BP passivated with Al_2O_3 constitutes the sensing/conducting channel in the FET which is further modified with antibody-conjugated gold nanoparticles (Fig. 20a). Binding of antigen to the BP surface creates a negative gate potential and changes the conductivity of the BP-FET biosensor, which makes it as a stable and rapid immunoglobin G (IgG) diagnostic tool offering a detection limit of 10 ng/mL.

Besides the electrical properties, the electrochemical properties have been exploited in BP-based IgG biosensors. Mayorga-Martinez et al. developed a label-free IgG biosensor using BP nanosheets as protein labels [202]. Compared to macroparticles, exfoliated BP nanosheets exhibit a less negative overpotential, reduced charge transfer resistance, and more catalytic edge sites for the hydrogen evolution reaction (HER). Thus, a bipolar electrochemical exfoliation approach has been adopted to fabricate BP nanosheets with enhanced HER activities in solutions. In the competitive magneto immunoassay, IgG-antibody functionalized magnetic beads co-precipitate BP nanosheets labeled IgG complexes which are subsequently denatured and transferred to an electrode. The concentration of IgG is indirectly measured *via* the HER activities of BP nanosheets co-precipitated on the electrode (Fig. 20b). This IgG biosensor has a dynamic range between 2 and 100 ng/mL, detection limit of 0.98 ng/mL, as well as good reproducibility. However, the selectivity and specificity of both IgG biosensors have only been evaluated in solutions supplemented with non-target proteins rather than in real serum samples. Hence, the diagnostic potential needs further clarification.

Sabherwal et al. reported a highly selective BPNSs-based biosensor for a cardiac biomarker, myoglobin (Mb), by measuring direct electron transfer from the redox active Mb in clinical samples [203]. Stable BP nanosheets are exfoliated in an aqueous environment by the surfactant-mediated method as an electrode and further modified with cationic polymer poly-L-lysine (PLL) by incubation to provide anchoring sites for Mb-specific DNA aptamer

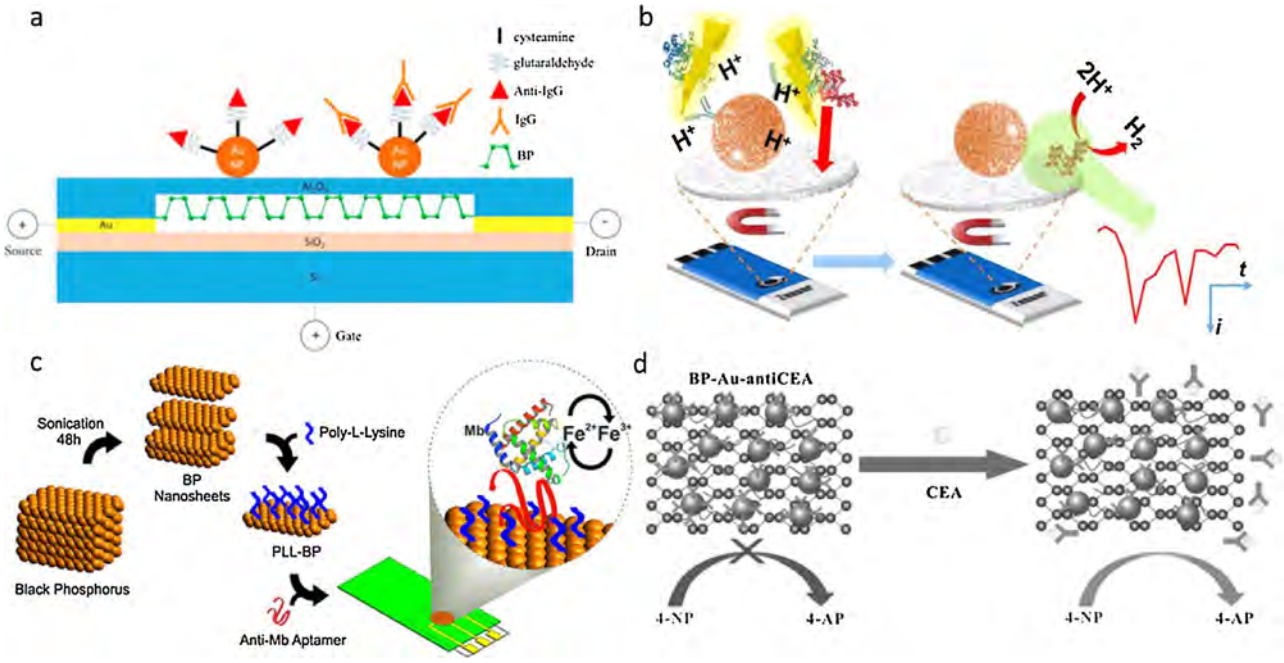

Fig. 20. BP-based biosensors. (a) Schematic representation of the BP-based FET biosensor for IgG detection. Reproduced with permission [201]. Copyright 2017, Elsevier. (b) Schematic representation of the label-free IgG biosensor using BP nanosheets as protein labels in magneto immunoassay. Reproduced with permission [202]. Copyright 2016, American Chemical Society. (c) Schematic representation of the BP-based biosensor for Mb detection. Reproduced with permission [203]. Copyright 2016, American Chemical Society. (d) Schematic representation of the BP-Au-antiCEA-based colorimetric biosensor for CEA diagnosis. The CEA-Anti CEA interaction induces desorption of the complex from the biosensor, and restores the BP's catalytic activity to convert yellow 4-NP to colorless 4-AP. Reprinted with permission [204]. Copyright 2016, Wiley. (For interpretation of the references to colour in this figure legend, the reader is referred to the web version of this article.)

through coulombic interactions. When bound to the DNA aptamer, the heme group of Mb undergoes the iron(II)/(III) redox reaction by the one-electron transfer mechanism to give a free electron which increases the current of the underlying BP electrode (Fig. 20c). This PLL-Apt-BP biosensor outperforms the rGO counterparts and exhibits high sensitivity (detection limit of 0.524 pg/mL) and specificity towards Mb with a wide dynamic response (1 pg/mL ~ 16 μg/mL) in clinical serum samples.

The carcinoembryonic antigen (CEA) colorimetric biosensor was prepared by Peng et al. by utilizing the instability of few-layer BP nanosheets [204]. Instability of BP has long been regarded as a major drawback but the authors take advantage of reducing 4-nitrophenol (4-NP) to give colorimetric outputs in the system. Specifically, gold nanoparticles are grown on BP nanosheets under optimal conditions and conjugated with CEA antibodies. The BP-Au-Anti CEA shows inhibited catalytic activity to reduce yellowish 4-NP to colorless 4-aminophenol (4-AP), while CEA-Anti CEA interaction induces desorption of the complex from the sensor and restores the BP's catalytic activity (Fig. 20d). This biosensor has a wide detection range, high sensitivity, and good specificity in both solution and serum samples. Preliminary data demonstrate that the diagnostic results obtained from the biosensor are consistent with those determined by ELISA, suggesting the instability-related limitation of BP could be used preferentially in biomolecular detection.

These examples represent two groups of BP-based biosensors with different application potentials. The first group is based on the fabrication of a relatively stable BP-biosensor by surface modification or passivation. These biosensors good for diagnostics take advantage of the superior electrical and electrochemical properties of BP. The second group, on the other hand, exploits the instability of BP and catalytic activity in redox reactions for the development of rapid, low-cost, and disposable point-of-care testing devices.

5.5.2. Phototherapy

With a thickness-dependent bandgap ranging from 0.3 to 2.0 eV, BP has broad absorption spanning the UV to NIR regions and possesses interesting photophysical properties such as photothermal and photodynamic effects. Because of the high efficiency and minimal invasiveness, NIR-light induced photothermal therapy undergoes fast development as an important supplement to traditional cancer therapy. The potential of BP as an antitumor photothermal therapy agent stems from its biocompatibility, strong extinction coefficient, and high photothermal conversion efficiency. By combining probe and bath sonication, an efficient method to prepare BPQDs has been proposed, followed by modification with PEG to improve the stability in the PBS buffer (Fig. 21a&b) [36]. The BPQDs rapidly and efficiently convert NIR irradiation into thermal energy (Fig. 21c) with a photothermal conversion efficiency of 28.4% at 808 nm, which is much higher than those of commercialized Au nanoshells and Au nanorods. Subsequent *in vitro* studies verify the good biocompatibility for different cell types (Fig. 21d) as well as the excellent photothermal therapy efficiency in promoting cancerous cell death under NIR irradiation (Fig. 21**e**). This study establishes the foundation for the application of BP to photothermal cancer therapy.

To improve its therapeutic efficacy and accomplish controllable biodegradation, PLGA coated BPQDs nanospheres (BPQDs/PLGA NSs) were fabricated by an oil-in-water emulsion solvent evaporation protocol [37]. The BPQDs/PLGA NSs exhibit not only reduced cytotoxicity and enhanced stability, but also tunable degradation rates by simply optimizing the chemical composition of the PLGA shells (Fig. 22a&b). The *in vivo* studies demonstrate the advantages of BPQDs/PLGA NSs as a biodegradable/biocompatible photothermal agent in cancer therapy including the minimal toxicity, prolonged blood circulation, good tumor targeting ability, strong NIR photothermal efficiency, and excellent tumor inhibitory effects (Fig. 22c). Fu et al. investigated the photothermal efficiency of BP nanosheets with different sizes [135]. Compared with small BPQDs which possess good NIR photothermal efficiency, large BP nanosheets show higher efficiency in photothermal conversion. However, photothermal applications of BP are still in the infancy and further development and optimization involving surface modification, exfoliation, and size control are needed.

Considering the unique electronic structure of BP, it may be a metal-free semiconductor to generate singlet oxygen which can be exploited in photodynamic applications. Wang et al. observed the photodynamic ability from ultrathin BP nanosheets [205]. Liquid exfoliated ultrathin BP nanosheets (average height of 2.0 nm) are used as the photosensitizer and $^1O_2$ generation is evaluated in ethanol. The singlet oxygen generation quantum yield of 0.91 is larger than that of most well-developed photosensitizers. Upconversion nanoparticles (UCNPs, NaGd-F4:Yb,Er@Yb@Nd@Yb) integrated with BP nanosheets constitute a stable and effective photosensitizer [206] and *in vivo* studies demonstrate specific tumor targeting and inhibitory effects induced by ROS generation of the nanocomposites.

5.5.3. Bioimaging

In combination with the phototherapeutic ability, BPQDs have been applied to photoacoustic imaging *in vivo*. Under irradiation with a short laser pulse, light-absorbing materials generate transient thermoelastic expansion and the pressure change can be detected by photoacoustic imaging [207]. As an emerging bioimaging technique, photoacoustic imaging can overcome the shortcomings of conventional imaging techniques such as speckle artifacts in ultrasound imaging, and limited penetration depth in optical imaging [208,209]. Sun et al. reported the application of the PEGylated BPQDs as an agent for *in vivo* photoacoustic imaging and photothermal therapy of cancer [210]. The BPQDs are prepared by solventless high energy mechanical milling and then PEGylated for enhanced water-solubility and stability. In addition to the high photothermal conversion efficiency, good biocompatibility, and strong photothermal ablation ability towards cancerous cells, this agent will specifically accumulate in tumors due to the enhanced permeability retention (EPR) effects thereby making them suitable for photoacoustic imaging and phototherapy for cancer. Sun et al. produced BPQDs coordinated with TiL_4 (TiL_4@BPQDs) as an efficient photoacoustic imaging agent [211]. Since the lone-pair electrons of BP are occupied by the electrophilic TiL_4, oxidation and degradation of the BPQDs are prevented. The TiL_4@BPQDs show a good extinction coefficient at 680 nm (22.2 $L\,g^{-1}\,cm^{-1}$) in the solution and it is better than those of Au nanorods under the same concentration. Subsequent *in vitro* and *in vivo* experiments illustrate the high sensitivity and spatial resolution in tumor diagnosis mediated by PA imaging.

5.5.4. Combined theranostic applications

Owing to the atomically thin 2D structure and large surface area, the drug delivery ability of BP, in combination with their photothermal and photodynamic effects, has been investigated as a novel theranostic approach in cancer therapy. Tao et al. produced PEGylated BP nanosheets as an efficient theranostic delivery platform *in vitro* and *in vivo* [212] and showed a high capacity towards doxorubicin (DOX) loading (loading capacity of 108% w/w) and release could be tuned by NIR-laser induced hyperthermia stimuli. *In vitro* studies reveal caveolae-dependent and a micropinocytosis-mediated endocytosis of the BP nanosheets which eventually degrade through the autophage-lysosome pathway in HeLa cells. The *in vivo* studies demonstrate impressive tumor ablation ability of the drug delivery platform based on the "triple-response combined strategy", namely photothermal,

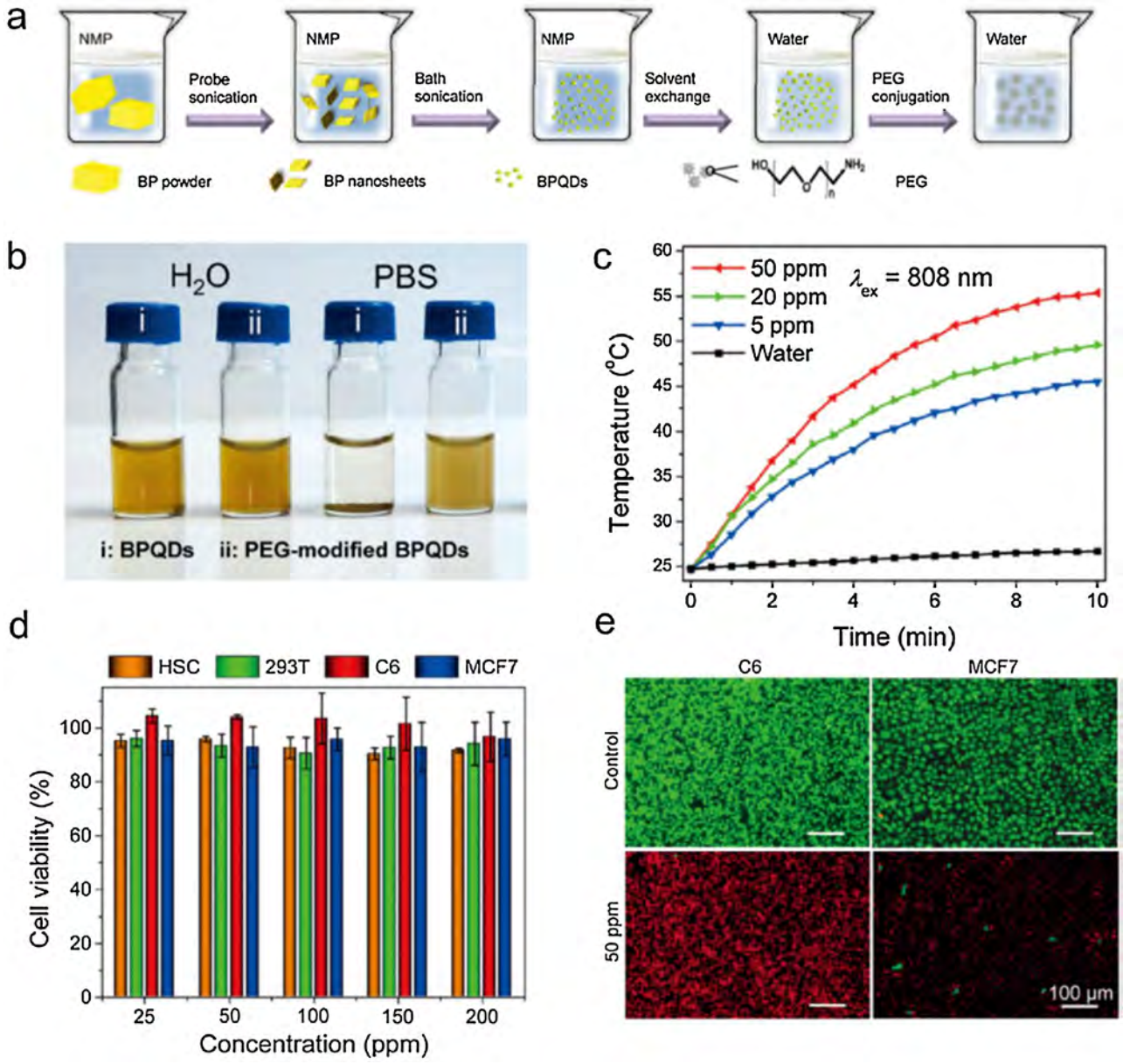

Fig. 21. in vitro application of PEGylated ultrasmall BPQDs in anti-cancer photothermal therapy. (a) Schematic representation of the synthesis and surface PEGylation of BPQDs. (b) Pictures of bare BPQDs (i) and the PEGylated BPQDs (ii) in H_2O and PBS. (c) Photothermal heating curves of water and the PEGylated BPQDs suspended in water at different concentrations when irradiated by 808 nm laser (1.0 W cm^{-2}). (d) Cytotoxicity of the PEGylated BPQDs in different cell types after 48 h' incubation. (e) Destruction of C6 and MCF-7 cells induced by the PEGylated BPQDs when irradiated by 808 nm laser (1.0 W cm^{-2}). Live cells were stained with calcein AM (green fluorescence), while dead cells were stained with PI (red fluorescence). (a-e) Reproduced with permission [36]. Copyright 2015, Wiley. (For interpretation of the references to colour in this figure legend, the reader is referred to the web version of this article.)

chemotherapeutic, and biological responses induced, respectively, by the BP nanosheets delivered DOX, and co-injected chloroquine. Chen et al. proposed a similar DOX delivery system based on unmodified BP nanosheets for cancer therapy by combining the photodynamic, photothermal, and chemotherapeutic effects [213]. The DOX loading capacity of the unmodified BP nanosheets is 950% in weight. Recently, Yang et al. reported a multifunctional BP@Au@Fe_3O_4 nanocomposite as a promising theranostic carrier in cancer therapy. The nanoparticles show reduced cytotoxicity, enhanced stability, good photothermal and dual-photodynamic properties, and impressive tumor ablation ability *in vitro* and *in vivo* [214].

6. Summary and prospective

This review summarizes recent research on atomically thin BP systems. The common synthesis methods, modification schemes, properties, and applications are discussed. Phosphorus, as a vital element has been studied for centuries but commercial applications such as fertilizers, feed additives, napalm bombs, and propellants [17]. The emergence of 2D BP with fascinating properties has aroused interests pertaining to nanoelectronics, optoelectronics, energy, and biomedicine. Inspired by other types of 2D materials such as graphene and TMDs, there has been tremendous development with respect to BP [2] and opportunities come with challenges.

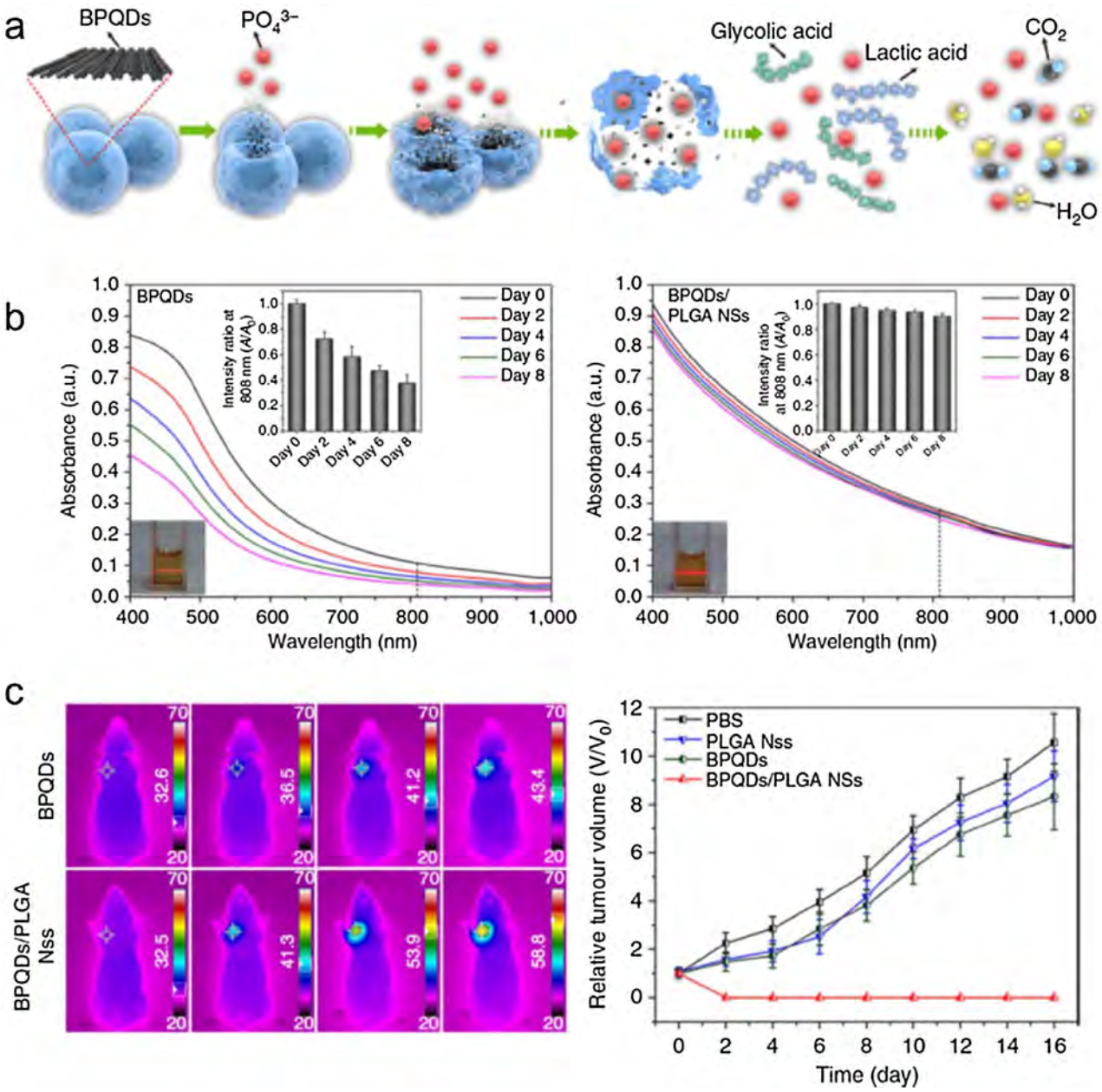

Fig. 22. In vivo application of BPQDs/PLGA NSs in anti-cancer photothermal therapy. (a) Schematic representation of the degradation progresses of the synthesized BPQDs/PLGA NSs under physiological conditions. (b) Tyndall effect and variation of the absorption ratios at 808 nm to represent enhanced stability of BPQDs/PLGA NSs under physiological conditions. (c) Infrared thermographic maps (left) and growth curves (right) of MCF-7 breast tumor in different groups of nude mice treated with PBS, PLGA NSs, bare BPQDs, and BPQDs/PLGA NSs with NIR laser irradiation. (a–c) Reproduced with permission [37]. Copyright 2016, Nature Publishing Group.

The first obstacle is the lack of reliable and scalable production techniques for wafer-scale and high-quality BP thin films. Bottom-up synthesis approaches for high-quality BP thin films such as direct chemical growth are still rare probably due to the chemical reactivity of BP and the absence of suitable substrates [17]. The liquid-exfoliation method provides a facile and low-cost way to produce large-scale few-layer BP nanosheets but the quality may not be high enough for some device applications. More research in this area is required to take BP from the laboratory to commercial application.

Since almost all the current electronic and optoelectronic devices rely on the quality of BP, the environmental instability of BP degrades the device performance and hinders more extensive applications. Passivation schemes such as ALD growth of protection layers [88], decoration with organic ligands [85], and vdW capping with BN [82] have been developed. So far, the highest mobility of BP FETs is observed from the BN-BP-BN sandwiched structure fabricated by the all-dry transfer technique in vacuum [109]. However, this approach is time consuming and not readily scalable. To produce commercial BP devices, a more convenient and reproducible passivation method to preserve the quality of BP and device performance is imperative. On the other hand, the instability of BP can be harnessed in some applications to produce environmentally harmless byproducts after degradation.

The unique properties distinguishing BP from other 2D materials such as the strong in-plane anisotropy and negative Poisson's ratio [15,132] render BP attractive in fundamental research and practical applications. In this respect, theoretical studies have outpaced experimental verification. With more experimental data, theory and experiments can in combination

offer more insightful understanding and expand research opportunities. For example, to build devices exploiting the anisotropy of BP, a facile and reliable approach to align to the desired direction on a large scale is indispensable.

Since BP offers a tunable bandgap in the range between 0.3 and 2.0 eV which enables broad light absorption from the visible to NIR regions, BP can theoretically serve as a metal-free and environmentally friendly photocatalyst in water splitting [217]. The electronic band structure of BP depends on the layer number and the stand-alone monolayered or few-layered BP is an excellent catalyst. For example, Zhu et al. reported visible light photocatalytic H_2 evolution of ball-milled (BM) exfoliated BP nanosheets and the H_2 evolution activity of the BM-BP nanosheets was 18 times higher than that of the bulk BP [218]. In addition, when combined with other semiconductors, the bulk or multilayered BP is a co-catalyst to extend light absorption and improve the catalytic ability [89,219,220]. For instance, H. Uk Lee et al. [89] and M. Zhu et al. [219] combined BP nanosheets with TiO_2 and $Au/La_2Ti_2O_7$ nanostructures to sensitize light absorption in the visible and NIR regions, respectively and J. Ran et al. designed a phosphorene/metal sulfide photocatalytic system [220]. Owing to the pronounced electronic coupling and excellent charge carrier mobility between these two components, the H_2-production activity was enhanced to 11192 mmol h^{-1} g^{-1}.

Development of biomedical application is also quite rapid. The excellent biocompatibility and natural degradability make BP attractive in many biological applications. The bandgap can be tuned to tailor the efficiency in photoacoustic imaging and photothermal/photodynamic therapies. Another remarkable but still underexplored feature of BP is the potential as a carrier for biological and biomedical molecules. Because of its puckered honeycomb structure of adjacent phosphorus atoms, BP has a larger surface-to-volume ratio than other 2D nanomaterials. For example, PEGylated and bare BP nanosheets are efficient DOX carriers with loading capacities of 108% and 950% (w/w), respectively [212,213]. Last but not least, the chemical instability which is unwanted in many applications can be exploited in biomedical and environmental applications. For example, a sensitive CEA biosensor based on active degradation of BP nanosheets has been produced [204]. In fact, degradation of BP *in vitro* and *in vivo* depends on many factors such as its size, light exposure, reactive oxygen species, and so on. These complicated but interesting issues offer opportunities to tailor the degradation rate of BP to suit particular applications.

In summary, BP as an emerging 2D material is being extensively studied and there are many opportunities from both the theoretical and practical aspects. Future research and breakthroughs require collaboration of scientists from different fields including materials, science, physics, chemistry, and biology.

Conflict of interest

The authors declare no competing financial interest.

Acknowledgments

This work was jointly supported by the National Natural Science Fund of China No. 51672305, Frontier Research Key Project of the Chinese Academy of Sciences No. QYZDBSSW-SLH034, Shenzhen Science and Technology Research Funding No. JCYJ201602293000503, Leading Talents of Guangdong Province Program No. 00201520, Hong Kong Research Grants Council (RGC) General Research Funds (GRF) No. CityU 11301215, as well as City University of Hong Kong Applied Research Grant (ARG) No. 9667144.

REFERENCESs

[1] K.S. Novoselov, D. Jiang, F. Schedin, T.J. Booth, V.V. Khotkevich, S.V. Morozov, A.K. Geim, Proc. Natl. Acad. Sci. U. S. A. 102 (2005) 10451–10453.
[2] C. Tan, X. Cao, X.-J. Wu, Q. He, J. Yang, X. Zhang, J. Chen, W. Zhao, S. Han, G.-H. Nam, M. Sindoro, H. Zhang, Chem. Rev. 117 (2017) 6225–6331.
[3] F. Xia, H. Wang, D. Xiao, M. Dubey, A. Ramasubramaniam, Nat. Photonics 8 (2014) 899–907.
[4] D. Akinwande, N. Petrone, J. Hone, Nat. Commun. 5 (2014) 5678.
[5] A.K. Geim, I.V. Grigorieva, Nature 499 (2014) 419–425.
[6] A.K. Geim, K.S. Novoselov, Nat. Mater. 6 (2007) 183–191.
[7] A.K. Geim, Science 324 (2009) 1530–1534.
[8] F. Bonaccorso, Z. Sun, T. Hasan, A.C. Ferrari, Nat. Photonics 4 (2010) 611–622.
[9] M. Xu, T. Liang, M. Shi, H. Chen, Chem. Rev. 113 (2013) 3766–3798.
[10] Q.H. Wang, K. Kalantar-Zadeh, A. Kis, J.N. Coleman, M.S. Strano, Nat. Nanotechnol. 7 (2012) 699–712.
[11] D. Jariwala, V.K. Sangwan, L.J. Lauhon, T.J. Marks, M.C. Hersam, ACS Nano 8 (2014) 1102–1120.
[12] Q. Tang, Z. Zhou, Prog. Mater. Sci. 58 (2013) 1244–1315.
[13] X. Ling, H. Wang, S. Huang, F. Xia, M.S. Dresselhaus, J. Lau, Proc. Natl. Acad. Sci. 112 (2015) 4523.
[14] H. Liu, Y. Du, Y. Deng, P.D. Ye, Chem. Soc. Rev. 44 (2015) 2732–2743.
[15] V. Eswaraiah, Q. Zeng, Y. Long, Z. Liu, Small 12 (2016) 3480–3502.
[16] A. Castellanos-Gomez, J. Phys. Chem. Lett. 6 (2015) 4280–4291.
[17] L. Kou, C. Chen, S.C. Smith, J. Phys. Chem. Lett. 6 (2015) 2794–2805.
[18] V. Sorkin, Y. Cai, Z. Ong, G. Zhang, Y.W. Zhang, Taylor Francis 0 (2016) 1–82.
[19] P.W. Bridgman, J. Am. Chem. Soc. 36 (1914) 1344–1363.
[20] H. Liu, A.T. Neal, Z. Zhu, Z. Luo, X. Xu, D. Tomanek, P.D. Ye, ACS Nano 8 (2014) 4033–4041.
[21] L. Li, Y. Yu, G.J. Ye, Q. Ge, X. Ou, H. Wu, D. Feng, Nat. Nanotechnol. 9 (2014) 372–377.
[22] V. Tran, R. Soklaski, Y. Liang, L. Yang, Phys. Rev. B Condens. Matter Mater. Phys. 89 (2014) 235319.
[23] A.S. Rodin, A. Carvalho, A.H. Castro Neto, Phys. Rev. Lett. 112 (2014) 176801.
[24] C.R. Ryder, J.D. Wood, S.A. Wells, M.C. Hersam, ACS Nano 10 (2016) 3900–3917.
[25] X. Wang, S. Lan, Adv. Opt. Photonics 8 (2016) 618.
[26] S. Das, M. Demarteau, A. Roelofs, N. Material, H.E. Physics, U. States, ACS Nano 8 (2014) 11730–11738.
[27] Y. Du, H. Liu, Y. Deng, P.D. Ye, ACS Nano 8 (2014) 10035–10042.
[28] Y. Saito, Y. Iwasa, ACS Nano 9 (2015) 3192–3198.
[29] A. Morita, Appl. Phys. A Solids Surf. 39 (1986) 227–242.
[30] J. Qiao, X. Kong, Z.-X. Hu, F. Yang, W. Ji, Nat. Commun. 5 (2014) 4475.
[31] F. Xia, H. Wang, Y. Jia, Nat. Commun. 5 (2014) 4458.
[32] S. Lan, X. Wang, S. Rodrigues, L. Wang, Y. Cui, H. Wang, F. Xia, W. Cai, ACS Photonics 3 (2016) 1176–1181.
[33] Z. Luo, J. Maassen, Y. Deng, Y. Du, M.S. Lundstrom, P.D. Ye, X. Xu, Nat. Commun. 6 (2015) 8572.
[34] X. Wang, A.M. Jones, K.L. Seyler, V. Tran, Y. Jia, H. Zhao, H. Wang, L. Yang, X. Xu, F. Xia, Nat. Nanotechnol. 10 (2015) 517–521.
[35] J. Tao, W. Shen, S. Wu, L. Liu, Z. Feng, C. Wang, C. Hu, P. Yao, H. Zhang, W. Pang, X. Duan, J. Liu, C. Zhou, D. Zhang, ACS Nano 9 (2015) 11362–11370.
[36] Z. Sun, H. Xie, S. Tang, X.F. Yu, Z. Guo, J. Shao, H. Zhang, H. Huang, H. Wang, P.K. Chu, Angew. Chem. Int. Ed. 54 (2015) 11526–11530.
[37] J. Shao, H. Xie, H. Huang, Z. Li, Z. Sun, Y. Xu, Q. Xiao, X.-F. Yu, Y. Zhao, H. Zhang, H. Wang, P.K. Chu, Nat. Commun. 7 (2016) 12967.
[38] Q. Zhou, Q. Chen, Y. Tong, J. Wang, Angew. Chem. Int. Ed. 55 (2016) 11437–11441.
[39] A. Castellanos-Gomez, L. Vicarelli, E. Prada, J.O. Island, K.L. Narasimha-Acharya, S.I. Blanter, D.J. Groenendijk, M. Buscema, G.a. Steele, J.V. Alvarez, H. W. Zandbergen, J.J. Palacios, H.S.J. van der Zant, 2D Mater. 1 (2014) 25001.
[40] J.D. Wood, S.A. Wells, D. Jariwala, K.-S.S. Chen, E. Cho, V.K. Sangwan, X. Liu, L.J. Lauhon, T.J. Marks, M.C. Hersam, Nano Lett. 14 (2014) 6964–6970.
[41] R.A. Doganov, E.C.T. O'Farrell, S.P. Koenig, Y. Yeo, A. Ziletti, A. Carvalho, D.K. Campbell, D.F. Coker, K. Watanabe, T. Taniguchi, A.H. Castro Neto, B. Özyilmaz, Nat. Commun. 6 (2015) 6647.
[42] P.W. Bridgman, Phys. Rev. 48 (1935) 893.
[43] P.W. Bridgman, Proc. Am. Acad. Arts Sci. 71 (1937) 387–460.
[44] I. Shirotani, Mol. Cryst. Liq. Cryst. 82 (1982) 203–211.
[45] S. Endo, Y. Akahama, S. Terada, S. Narita, J. Appl. Phys. 21 (1982) L482–L484.
[46] E.N. Rissi, E. Soignard, K.A. McKiernan, C.J. Benmore, J.L. Yarger, Solid State Commun. 152 (2012) 390–394.
[47] V.H. Krebs, H. Weitz, K.H. Worms, J. Inorg. Chem. 280 (1955) 119–133.
[48] A. Brown, S. Rundqvist, Acta Cryst. 19 (1965) 684.
[49] S. Lange, P. Schmidt, T. Nilges, Inorg. Chem. 46 (2007) 4028–4035.
[50] T. Nilges, M. Kersting, T. Pfeifer, J. Solid State Chem. 181 (2008) 1707–1711.
[51] M. Kopf, N. Eckstein, D. Pfister, C. Grotz, I. Kruger, M. Greiwe, T. Hansen, H. Kohlmann, T. Nilges, J. Cryst. Growth 405 (2014) 6–10.
[52] W. Lu, H. Nan, J. Hong, Y. Chen, C. Zhu, Z. Liang, X. Ma, Z. Ni, C. Jin, Z. Zhang, Nano Res. 7 (2014) 853–859.
[53] J. Jia, S.K. Jang, S. Lai, J. Xu, Y.J. Choi, J. Park, ACS Nano 9 (2015) 8729–8736.
[54] J. Pei, X. Gai, J. Yang, X. Wang, Z. Yu, D.-Y. Choi, B. Luther-Davies, Y. Lu, Nat. Commun. 7 (2016) 10450.
[55] G.H. Han, S.J. Chae, E.S. Kim, F. Güneş, I.H. Lee, S.W. Lee, S.Y. Lee, S.C. Lim, H.K. Jeong, M.S. Jeong, Y.H. Lee, ACS Nano 5 (2011) 263–268.

[56] Y. Liu, H. Nan, X. Wu, W. Pan, W. Wang, J. Bai, W. Zhao, L. Sun, X. Wang, Z. Ni, ACS Nano 7 (2013) 4202–4209.
[57] X. Liu, K.S. Chen, S.A. Wells, I. Balla, J. Zhu, J.D. Wood, M.C. Hersam, Adv. Mater. 29 (2016) 1604121.
[58] X. Zhu, T. Zhang, Z. Sun, H. Chen, J. Guan, X. Chen, H. Ji, P. Du, S. Yang, Adv. Mater. 29 (2017) 1605776.
[59] X. Li, B. Deng, X. Wang, S. Chen, M. Vaisman, S. Karato, G. Pan, M.L. Lee, J. Cha, H. Wang, et al., 2D Mater. 2 (2015) 31002.
[60] H. Du, X. Lin, Z. Xu, D. Chu, J. Mater. Chem. C 3 (2015) 8760–8775.
[61] J.B. Smith, D. Hagaman, H.-F. Ji, Nanotechnology 27 (2016) 215602.
[62] Z. Yang, J. Hao, S. Yuan, S. Lin, H.M. Yau, J. Dai, Adv. Mater. 27 (2015) 3748–3754.
[63] Q. Jiang, L. Xu, N. Chen, H. Zhang, L. Dai, S. Wang, Angew. Chem. Int. Ed. 55 (2016) 13849–13853.
[64] J. Yu, J. Li, W. Zhang, H. Chang, Chem. Sci. 6 (2015) 6705–6716.
[65] J.N. Coleman, M. Lotya, A. O'Neill, S.D. Bergin, P.J. King, U. Khan, K. Young, A. Gaucher, S. De, R.J. Smith, et al., Science 331 (2011) 568–571.
[66] J.R. Brent, N. Savjani, E.A. Lewis, S.J. Haigh, J. Lewis, P.O. Brien, Chem. Commun. 50 (2014) 13338–13341.
[67] J. Kang, J.D. Wood, S.A. Wells, J.H. Lee, X. Liu, K.S. Chen, M.C. Hersam, ACS Nano 9 (2015) 3596–3604.
[68] P. Yasaei, B. Kumar, T. Foroozan, C. Wang, M. Asadi, D. Tuschel, J.E. Indacochea, R.F. Klie, A. Salehi-khojin, Adv. Mater. 27 (2015) 1887–1892.
[69] D. Hanlon, C. Backes, E. Doherty, C.S. Cucinotta, N.C. Berner, C. Boland, K. Lee, A. Harvey, P. Lynch, Z. Gholamvand, S. Zhang, K. Wang, G. Moynihan, A. Pokle, Q.M. Ramasse, N. McEvoy, W.J. Blau, J. Wang, G. Abellan, F. Hauke, A. Hirsch, S. Sanvito, D.D. O'Regan, G.S. Duesberg, V. Nicolosi, J.N. Coleman, Nat. Commun. 6 (2015) 8563.
[70] Z. Guo, H. Zhang, S. Lu, Z. Wang, S. Tang, J. Shao, Z. Sun, H. Xie, H. Wang, X.F. Yu, P.K. Chu, Adv. Funct. Mater. 25 (2015) 6996–7002.
[71] W. Zhao, Z. Xue, J. Wang, J. Jiang, X. Zhao, T. Mu, ACS Appl. Mater. Interfaces 7 (2015) 27608–27612.
[72] A.H. Woomer, T.W. Farnsworth, J. Hu, R.A. Wells, C.L. Donley, S.C. Warren, ACS Nano 9 (2015) 8869–8884.
[73] F. Xu, B. Ge, J. Chen, A. Nathan, L.L. Xin, H. Ma, H. Min, C. Zhu, W. Xia, Z. Li, K. Li, L. Wu, Y. Cui, L. Sun, Y. Zhu, 2D Mater. 3 (2016) 25005.
[74] X. Zhang, H. Xie, Z. Liu, C. Tan, Z. Luo, H. Li, J. Lin, L. Sun, W. Chen, Z. Xu, L. Xie, W. Huang, H. Zhang, Angew. Chem. Int. Ed. 54 (2015) 3653–3657.
[75] Y. Xu, Z. Wang, Z. Guo, H. Huang, Q. Xiao, H. Zhang, X.F. Yu, Adv. Opt. Mater. 4 (2016) 1223–1229.
[76] J.O. Island, G.A. Steele, H.S.J. van der Zant, A. Castellanos-Gomez, 2D Mater. 2 (2015) 11002.
[77] Y. Huang, J. Qiao, K. He, S. Bliznakov, E. Sutter, X. Chen, D. Luo, F. Meng, D. Su, J. Decker, Chem. Mater. 28 (2016) 8330–8339.
[78] A. Favron, E. Gaufrès, F. Fossard, A.-L. Phaneuf-L'Heureux, N.Y.W. Tang, P.L. Lévesque, A. Loiseau, R. Leonelli, S. Francoeur, R. Martel, Nat. Mater. 14 (2015) 826–832.
[79] Q. Zhou, Q. Chen, Y. Tong, J. Wang, Angew. Chem. Int. Ed. 55 (2016) 11437–11441.
[80] J.S. Kim, P.J. Jeon, J. Lee, K. Choi, H.S. Lee, Y. Cho, Y.T. Lee, D.K. Hwang, S. Im, Nano Lett. 15 (2015) 5778–5783.
[81] Y. Lee, J. Kwon, E. Hwang, C.H. Ra, W.J. Yoo, J.H. Ahn, J.H. Park, J.H. Cho, Adv. Mater. 27 (2015) 41–46.
[82] A. Avsar, I.J. Vera-Marun, J.Y. Tan, K. Watanabe, T. Taniguchi, A.H. Castro Neto, B. Özyilmaz, ACS Nano 9 (2015) 4138–4145.
[83] X. Chen, Y. Wu, Z. Wu, Y. Han, S. Xu, L. Wang, W. Ye, T. Han, Y. He, Y. Cai, N. Wang, Nat. Commun. 6 (2015) 7315.
[84] Y. Zhao, Q. Zhou, Q. Li, X. Yao, J. Wang, Adv. Mater. 29 (2017) 1603990.
[85] Y. Zhao, H. Wang, H. Huang, Q. Xiao, Y. Xu, Z. Guo, H. Xie, J. Shao, Z. Sun, W. Han, X.F. Yu, P. Li, P.K. Chu, Angew. Chem. Int. Ed. 55 (2016) 5003–5007.
[86] G. Abellán, V. Lloret, U. Mundloch, M. Marcia, C. Neiss, A. Görling, M. Varela, F. Hauke, A. Hirsch, Angew. Chem. Int. Ed. 128 (2016) 14777–14782.
[87] B. Yang, B. Wan, Q. Zhou, Y. Wang, W. Hu, W. Lv, Q. Chen, Z. Zeng, F. Wen, J. Xiang, S. Yuan, J. Wang, B. Zhang, W. Wang, J. Zhang, B. Xu, Z. Zhao, Y. Tian, Z. Liu, Adv. Mater. 28 (2016) 9408–9415.
[88] J.-S. Kim, Y. Liu, W. Zhu, S. Kim, D. Wu, L. Tao, A. Dodabalapur, K. Lai, D. Akinwande, Sci. Rep. 5 (2015) 8989.
[89] H.U. Lee, S.C. Lee, J. Won, B.-C. Son, S. Choi, Y. Kim, S.Y. Park, H.-S. Kim, Y.-C. Lee, J. Lee, Sci. Rep. 5 (2015) 8691.
[90] C.R. Ryder, J.D. Wood, S.A. Wells, Y. Yang, D. Jariwala, T.J. Marks, G.C. Schatz, M. C. Hersam, Nat. Chem. (2016).
[91] R. Hultgren, N.S. Gingrich, B.E. Warren, J. Chem. Phys. 3 (1935) 351.
[92] R.J. Wu, M. Topsakal, T. Low, M.C. Robbins, N. Haratipour, J.S. Jeong, R.M. Wentzcovitch, S.J. Koester, K.A. Mkhoyan, J. Vac. Sci. Technol. A 33 (2015) 60604.
[93] C.D. Zhang, J.C. Lian, W. Yi, Y.H. Jiang, L.W. Liu, H. Hu, W.D. Xiao, S.X. Du, L.L. Sun, H.J. Gao, J. Phys. Chem. C 113 (2009) 18823–18826.
[94] J.C. Jamieson, Science 139 (1963) 1291.
[95] Y. Takao, H. Asahina, A. Morita, J. Phys. Soc. Jpn. 50 (1981) 3362–3369.
[96] H. Asahina, a. Morita, J. Phys. C Solid State Phys. 17 (2000) 1839–1852.
[97] T. Low, A.S. Rodin, A. Carvalho, Y. Jiang, H. Wang, F. Xia, A.H.C. Neto, Phys. Rev. B 90 (2014) 75434.
[98] Y. Cai, G. Zhang, Y.-W. Zhang, Sci. Rep. 4 (2014) 6677.
[99] L. Liang, J. Wang, W. Lin, B.G. Sumpter, V. Meunier, M. Pan, Nano Lett. 14 (2014) 6400–6406.
[100] R. Fei, L. Yang, Nano Lett. 14 (2014) 2884–2889.
[101] L. Li, J. Kim, C. Jin, G.J. Ye, D.Y. Qiu, F.H. da Jornada, Z. Shi, L. Chen, Z. Zhang, F. Yang, K. Watanabe, T. Taniguchi, W. Ren, S.G. Louie, X.H. Chen, Y. Zhang, F. Wang, Nat. Nanotechnol. 12 (2016) 21–25.
[102] S. Zhang, J. Yang, R. Xu, F. Wang, W. Li, M. Ghufran, Y.W. Zhang, Z. Yu, G. Zhang, Q. Qin, Y. Lu, ACS Nano 8 (2014) 9590–9596.
[103] M. Venkata Kamalakar, B.N. Madhushankar, A. Dankert, S.P. Dash, Small 11 (2015) 2209–2216.
[104] J. He, D. He, Y. Wang, Q. Cui, M.Z. Bellus, H.Y. Chiu, H. Zhao, ACS Nano 9 (2015) 6436–6442.
[105] H. Yuan, X. Liu, F. Afshinmanesh, W. Li, G. Xu, J. Sun, B. Lian, A.G. Curto, G. Ye, Y. Hikita, Z. Shen, S.-C. Zhang, X. Chen, M. Brongersma, H.Y. Hwang, Y. Cui, Nat. Nanotechnol. 10 (2015) 707–714.
[106] T. Hong, B. Chamlagain, W. Lin, H. Chuang, M. Pan, Nanoscale 6 (2014) 8978–8983.
[107] S. Ge, C. Li, Z. Zhang, C. Zhang, Y. Zhang, J. Qiu, Q. Wang, J. Liu, S. Jia, J. Feng, D. Sun, Nano Lett. 15 (2015) 4650–4656.
[108] S. Das, W. Zhang, M. Demarteau, A. Hoffmann, M. Dubey, A. Roelofs, Nano Lett. 16 (2016) 2122–2122.
[109] G. Long, D. Maryenko, J. Shen, S. Xu, J. Hou, Z. Wu, W.K. Wong, T. Han, J. Lin, Y. Cai, R. Lortz, N. Wang, Nano Lett. 16 (2016) 7768–7773.
[110] L. Li, G.J. Ye, V. Tran, R. Fei, G. Chen, H. Wang, J. Wang, K. Watanabe, T. Taniguchi, L. Yang, X.H. Chen, Y. Zhang, Nat. Nanotechnol. 10 (2015) 608–613.
[111] L. Li, F. Yang, G.J. Ye, Z. Zhang, Z. Zhu, W. Lou, X. Zhou, L. Li, K. Watanabe, T. Taniguchi, K. Chang, Y. Wang, X.H. Chen, Y. Zhang, Nat. Nanotechnol. 11 (2016) 593–597.
[112] V. Tayari, N. Hemsworth, I. Fakih, A. Favron, E. Gaufre, R. Martel, T. Szkopek, Nat. Commun. 7 (2015) 7702.
[113] N. Gillgren, D. Wickramaratne, Y. Shi, T. Espiritu, J. Yang, J. Hu, J. Wei, X. Liu, Z. Mao, K. Watanabe, T. Taniguchi, M. Bockrath, Y. Barlas, R.K. Lake, C.N. Lau, 2D Mater. 2 (2015) 11001.
[114] G. Long, D. Maryenko, S. Pezzini, S. Xu, Z. Wu, T. Han, J. Lin, Y. Wang, L. An, Y. Cai, U. Zeitler, N. Wang, Arxiv 1703 (2017) 5177.
[115] Y. Cai, Q. Ke, G. Zhang, Y.P. Feng, V.B. Shenoy, Y.W. Zhang, Adv. Funct. Mater. 25 (2015) 2230–2236.
[116] H. Jang, J.D. Wood, C.R. Ryder, M.C. Hersam, D.G. Cahill, Adv. Mater. 27 (2015) 8017–8022.
[117] Y. Wang, C. Cong, R. Fei, W. Yang, Y. Chen, B. Cao, L. Yang, T. Yu, Nano Res. 8 (2015) 3944–3953.
[118] X. Zhang, X.-F. Qiao, W. Shi, J.-B. Wu, D.-S. Jiang, P.-H. Tan, Chem. Soc. Rev. 44 (2015) 2757–2785.
[119] J. Wu, N. Mao, L. Xie, H. Xu, J. Zhang, Angew. Chem. Int. Ed. 54 (2015) 2366–2369.
[120] A.-L. Phaneuf-L'Heureux, A. Favron, J.-F. Germain, P. Lavoie, P. Desjardins, R. Leonelli, R. Martel, S. Francoeur, Nano Lett. 16 (2016) 7761–7767.
[121] H.B. Ribeiro, M.A. Pimenta, C.J.S. De Matos, R.L. Moreira, A.S. Rodin, J.D. Zapata, E.A.T. De Souza, A.H. Castro Neto, ACS Nano 9 (2015) 4270–4276.
[122] J. Kim, J.-U. Lee, J. Lee, H.J. Park, Z. Lee, C. Lee, H. Cheong, Nanoscale 7 (2015) 18708–18715.
[123] Y. Li, Z. Hu, S. Lin, S.K. Lai, W. Ji, S.P. Lau, Adv. Funct. Mater. 27 (2016) 1600986.
[124] A. Jain, A.J.H. Mcgaughey, Sci. Rep. 5 (2015) 8501.
[125] G. Qin, Q. Yan, Z. Qin, S. Yue, M.H. De, Phys. Chem. Chem. Phys. 17 (2015) 4854–4858.
[126] L. Zhu, G. Zhang, B. Li, Phys. Rev. B 90 (2014) 214302.
[127] T.-H. Liu, C.-C. Chang, Nanoscale 7 (2015) 10648–10654.
[128] G.A. Slack, Phys. Rev. 139 (1965) A507.
[129] C.X. Wang, C. Zhang, J.W. Jiang, H.S. Park, T. Rabczuk, Nanoscale 8 (2016) 901–905.
[130] Q. Wei, X. Peng, Appl. Phys. Lett. 104 (2014).
[131] J.-W. Jiang, H.S. Park, J. Phys. D Appl. Phys. 47 (2014) 385304.
[132] J.-W. Jiang, H.S. Park, Nat. Commun. 5 (2014) 4727.
[133] Z. Wang, H. Jia, X. Zheng, R. Yang, Z. Wang, G.J. Ye, X.H. Chen, J. Shan, P.X.-L. Feng, Nanoscale 7 (2015) 877–884.
[134] N.M. Latiff, W.Z. Teo, Z. Sofer, A.C. Fisher, M. Pumera, Chemistry (Easton) 21 (2015) 13991–13995.
[135] H.D. Fu, Z.B. Li, H.H. Xie, Z.B. Sun, B.K. Wang, H. Huang, G.L. Han, H.Y. Wang, P. K. Chu, X.F. Yu, RSC Adv. 7 (2017) 14618–14624.
[136] N. Haratipour, S.J. Koester, IEEE Electron Dev. Lett. 37 (2016) 103–106.
[137] D. Yue, D. Lee, Y.D. Jang, M.S. Choi, H.J. Nam, D.-Y. Jung, W.J. Yoo, Nanoscale 8 (2016) 12773–12779.
[138] D. Jena, A. Konar, Phys. Rev. Lett. 98 (2007).
[139] P.J. de Visser, R. Chua, J.O. Island, M. Finkel, A.J. Katan, H. Thierschmann, H.S.J. van der Zant, T.M. Klapwijk, 2D Mater. 3 (2016) 21002.
[140] J.T. Ye, Y.J. Zhang, R. Akashi, M.S. Bahramy, R. Arita, Y. Iwasa, Science 338 (2012) 1193–1196.
[141] X.K. Liu, K.W. Ang, W.J. Yu, J.Z. He, X.W. Feng, Q. Liu, H. Jiang, D. Tang, J. Wen, Y. M. Lu, W.J. Liu, P.J. Cao, S. Han, J. Wu, W.J. Liu, X. Wang, D.L. Zhu, Z.B. He, Sci. Rep. 6 (2016) 24920.
[142] N. Haratipour, M.C. Robbins, S.J. Koester, 36, 2015, 411–413.
[143] X. Cui, G.-H. Lee, Y.D. Kim, G. Arefe, P.Y. Huang, C.-H. Lee, D.A. Chenet, X. Zhang, L. Wang, F. Ye, et al., Nat. Nanotechnol. 10 (2015) 534–540.
[144] L. Wang, I. Meric, P.Y. Huang, Q. Gao, Y. Gao, H. Tran, T. Taniguchi, K. Watanabe, L.M. Campos, D.A. Muller, et al., Science 342 (2013) 614–617.
[145] D.J. Perello, S.H. Chae, S. Song, Y.H. Lee, Nat. Commun. 6 (2015) 7809.
[146] S.P. Koenig, R.A. Doganov, L. Seixas, A. Carvalho, J.Y. Tan, K. Watanabe, T. Taniguchi, N. Yakovlev, A.H. Castro Neto, B. Ozyilmaz, Nano Lett. 16 (2016) 2145–2151.
[147] A. Prakash, Y. Cai, G. Zhang, Y.-W. Zhang, K.-W. Ang, Small 13 (2016) 1602909.

[148] L. Li, M. Engel, D.B. Farmer, S.J. Han, H.S.P. Wong, ACS Nano 10 (2016) 4672–4677.
[149] Y. Liu, H. Wu, H.-C. Cheng, S. Yang, E. Zhu, Q. He, M. Ding, D. Li, J. Guo, N.O. Weiss, et al., Nano Lett. 15 (2015) 3030–3034.
[150] J. Miao, S. Zhang, L. Cai, M. Scherr, C. Wang, ACS Nano 9 (2015) 9236–9243.
[151] S. Das, W. Zhang, L.R. Thoutam, Z. Xiao, A. Hoffmann, M. Demarteau, A. Roelofs, IEEE Electron Device Lett. 36 (2015) 621–623.
[152] D. Xiang, C. Han, J. Wu, S. Zhong, Y. Liu, J. Lin, X.-A. Zhang, W. Ping Hu, B. Özyilmaz, a H.C. Neto, A.T.S. Wee, W. Chen, Nat. Commun. 6 (2015) 6485.
[153] H. Wang, X. Wang, F. Xia, L. Wang, H. Jiang, Q. Xia, M.L. Chin, M. Dubey, S.J. Han, Nano Lett. 14 (2014) 6424–6429.
[154] W. Zhu, S. Park, M.N. Yogeesh, K.M. McNicholas, S.R. Bank, D. Akinwande, Nano Lett. 16 (2016) 2301–2306.
[155] Y. Su, C.U. Kshirsagar, M.C. Robbins, N. Haratipour, S.J. Koester, 2D Mater. 3 (2016) 11006.
[156] W. Zhu, M.N. Yogeesh, S. Yang, S.H. Aldave, J.-S. Kim, S. Sonde, L. Tao, N. Lu, D. Akinwande, Nano Lett. 15 (2015) 1883–1890.
[157] S.M. Sze, K.K. Ng, Physics of Semiconductor Devices, John wiley & sons, 2006.
[158] R. Yan, S. Fathipour, Y. Han, B. Song, S. Xiao, M. Li, N. Ma, V. Protasenko, D.A. Muller, D. Jena, H.G. Xing, Nano Lett. 15 (2015) 5791–5798.
[159] W. Yang, L. Gan, H. Li, T. Zhai, Inorg. Chem. Front. 3 (2016) 433–451.
[160] A.N. Abbas, B. Liu, L. Chen, Y. Ma, S. Cong, N. Aroonyadet, M. Köpf, T. Nilges, C. Zhou, ACS Nano 9 (2015) 5618–5624.
[161] L. Kou, T. Frauenheim, C. Chen, J. Phys. Chem. Lett. 5 (2014) 2675–2681.
[162] S. Cui, H. Pu, S.A. Wells, Z. Wen, S. Mao, J. Chang, M.C. Hersam, J. Chen, Nat. Commun. 6 (2015) 8632.
[163] C.C. Mayorga-Martinez, Z. Sofer, M. Pumera, Angew. Chem. Int. Ed. 54 (2015) 14317–14320.
[164] P. Yasaei, A. Behranginia, T. Foroozan, M. Asadi, K. Kim, F. Khalili-Araghi, A. Salehi-Khojin, ACS Nano 9 (2015) 9898–9905.
[165] H. Fang, S. Chuang, T.C. Chang, K. Takei, T. Takahashi, A. Javey, Nano Lett. 12 (2012) 3788–3792.
[166] M. Buscema, D.J. Groenendijk, S.I. Blanter, G.A. Steele, H.S.J. Van Der Zant, A. Castellanos-Gomez, Nano Lett. 14 (2014) 3347–3352.
[167] O. Lopez-Sanchez, D. Lembke, M. Kayci, A. Radenovic, A. Kis, Nat. Nanotechnol. 8 (2013) 497–501.
[168] N. Perea-López, A.L. Elías, A. Berkdemir, A. Castro-Beltran, H.R. Gutiérrez, S. Feng, R. Lv, T. Hayashi, F. López-Urías, S. Ghosh, B. Muchharla, S. Talapatra, H. Terrones, M. Terrones, Adv. Funct. Mater. 23 (2013) 5511–5517.
[169] P. Hu, Z. Wen, L. Wang, P. Tan, K. Xiao, ACS Nano 6 (2012) 5988–5994.
[170] P. Hu, L. Wang, M. Yoon, J. Zhang, W. Feng, X. Wang, Z. Wen, J.C. Idrobo, Y. Miyamoto, D.B. Geohegan, et al., Nano Lett. 13 (2013) 1649–1654.
[171] M. Huang, M. Wang, C. Chen, Z. Ma, X. Li, J. Han, Y. Wu, Adv. Mater. 28 (2016) 3481–3485.
[172] Q. Guo, A. Pospischil, M. Bhuiyan, H. Jiang, H. Tian, D. Farmer, B. Deng, C. Li, S.-J. Han, H. Wang, Q. Xia, T.-P. Ma, T. Mueller, F. Xia, Nano Lett. 16 (2016) 4648–4655.
[173] J. Wu, G.K.W. Koon, D. Xiang, C. Han, C.T. Toh, E.S. Kulkarni, I. Verzhbitskiy, A. Carvalho, A.S. Rodin, S.P. Koenig, G. Eda, W. Chen, A.H.C. Neto, B. Ozyilmaz, ACS Nano 9 (2015) 8070–8077.
[174] T. Low, M. Engel, M. Steiner, P. Avouris, Phys. Rev. B – C Condens. Matter Mater. Phys. 90 (2014) 81408.
[175] N. Youngblood, C. Chen, S.J. Koester, M. Li, Nat. Photonics 9 (2015) 249–252.
[176] M. Engel, M. Steiner, P. Avouris, Nano Lett. 14 (2014) 6414–6417.
[177] M. Buscema, D.J. Groenendijk, G. a Steele, H.S.J. van der Zant, A. Castellanos-Gomez, Nat. Commun. 5 (2014) 4651.
[178] J. Lu, A. Carvalho, J. Wu, H. Liu, E.S. Tok, A.H.C. Neto, B. Özyilmaz, C.H. Sow, Adv. Mater. 28 (2016) 4090–4096.
[179] Y. Deng, Z. Luo, N.J. Conrad, H. Liu, Y. Gong, S. Najmaei, P.M. Ajayan, J. Lou, X. Xu, P.D. Ye, ACS Nano 8 (2014) 8292–8299.
[180] L. Ye, H. Li, Z. Chen, J. Xu, ACS Nano 3 (2016) 692–699.
[181] P. Chen, T.T. Zhang, J. Zhang, J. Xiang, H. Yu, S. Wu, X. Lu, G. Wang, F. Wen, Z. Liu, R. Yang, D. Shi, G. Zhang, Nanoscale 8 (2016) 3254–3258.
[182] M. Buscema, J.O. Island, D.J. Groenendijk, S.I. Blanter, G.A. Steele, H.S. van der Zant, A. Castellanos-Gomez, Chem. Soc. Rev. 44 (2015) 3691–3718.
[183] F. Liu, C. Zhu, L. You, S.J. Liang, S. Zheng, J. Zhou, Q. Fu, Y. He, Q. Zeng, H.J. Fan, L. K. Ang, J. Wang, Z. Liu, Adv. Mater. 28 (2016) 7768–7773.
[184] L. Viti, J. Hu, D. Coquillat, W. Knap, A. Tredicucci, A. Politano, M.S. Vitiello, Adv. Mater. 27 (2015) 5567–5572.
[185] L. Viti, J. Hu, D. Coquillat, A. Politano, C. Consejo, W. Knap, M.S. Vitiello, Adv. Mater. 28 (2016) 7390–7396.
[186] J. Kang, D. Jariwala, C.R. Ryder, S.A. Wells, Y. Choi, E. Hwang, J.H. Cho, T.J. Marks, M.C. Hersam, Nano Lett. 16 (2016) 2580–2585.
[187] D. Li, H. Jussila, L. Karvonen, G. Ye, H. Lipsanen, X. Chen, Z. Sun, Sci. Rep. 5 (2015) 15899.
[188] J. Sotor, G. Sobon, W. Macherzynski, P. Paletko, K.M. Abramski, Appl. Phys. Lett. 107 (2015) 51108.
[189] S.B. Lu, L.L. Miao, Z.N. Guo, X. Qi, C.J. Zhao, H. Zhang, S.C. Wen, D.Y. Tang, D.Y. Fan, Opt. Express 23 (2015) 11183–11194.
[190] Y. Chen, G. Jiang, S. Chen, Z. Guo, X. Yu, C. Zhao, H. Zhang, Q. Bao, S. Wen, D. Tang, D. Fan, Opt. Express 23 (2015) 12823–12833.
[191] C.-M. Park, H.-J. Sohn, Adv. Mater. 19 (2007) 2465–2468.
[192] W. Li, Y. Yang, G. Zhang, Y. Zhang, Nano Lett. 15 (2015) 1691–1697.
[193] J. Sun, G. Zheng, H.W. Lee, N. Liu, H. Wang, H. Yao, W. Yang, Y. Cui, Nano Lett. 14 (2014) 4573–4580.
[194] C. Chowdhury, S. Karmakar, A. Datta, ACS Energy Lett. 1 (2016) 253–259.
[195] Y. Yang, J. Gao, Z. Zhang, S. Xiao, H.H. Xie, Z.B. Sun, J.H. Wang, C.H. Zhou, Y.W. Wang, X.Y. Guo, P.K. Chu, X.F. Yu, Adv. Mater. 28 (2016) 8937–8944.
[196] G. Guo, X. Wei, Q. Zhang, H. Liu, W. Lau, L. Liu, J. Phys. Chem. Lett. 6 (2015) 5002–5008.
[197] V.V. Kulish, O.I. Malyi, P. Wu, Phys. Chem. Chem. Phys. 17 (2015) 13921–13928.
[198] J. Sun, H.-W. Lee, M. Pasta, H. Yuan, G. Zheng, Y. Sun, Y. Li, Y. Cui, Nat. Nanotechnol. 10 (2015) 980–985.
[199] M. Dahbi, N. Yabuuchi, M. Fukunishi, K. Kubota, K. Chihara, K. Tokiwa, X.F. Yu, H. Ushiyama, K. Yamashita, J.Y. Son, Y.T. Cui, H. Oji, S. Komaba, Chem. Mater. 28 (2016) 1625–1635.
[200] Z. Wang, P.X.-L. Feng, 2D Mater. 2 (2015) 21001.
[201] Y. Chen, R. Ren, H. Pu, J. Chang, S. Mao, J. Chen, Biosens. Bioelectron. 89 (2017) 505–510.
[202] C.C. Mayorga-Martinez, N. Mohamad Latiff, A.Y. Eng, Z. Sofer, M. Pumera, Anal. Chem. 88 (2016) 10074–10079.
[203] V. Kumar, J.R. Brent, M. Shorie, H. Kaur, G. Chadha, A.G. Thomas, E.A. Lewis, A.P. Rooney, L. Nguyen, X.L. Zhong, M.G. Burke, S.J. Haigh, A. Walton, P.D. McNaughter, A.A. Tedstone, N. Savjani, C.A. Muryn, P. O'Brien, A.K. Ganguli, D.J. Lewis, P. Sabherwal, ACS Appl. Mater. Interfaces 8 (2016) 22860–22868.
[204] J. Peng, Y. Lai, Y. Chen, J. Xu, L. Sun, J. Weng, Small 13 (2017) 1603589.
[205] H. Wang, X. Yang, W. Shao, S. Chen, J. Xie, X. Zhang, J. Wang, Y. Xie, J. Am. Chem. Soc. 137 (2015) 11376–11382.
[206] R.C. Lv, D. Yang, P.P. Yang, J.T. Xu, F. He, S.L. Gai, C.X. Li, Y.L. Dai, G.X. Yang, J. Lin, Chem. Mater. 28 (2016) 4724–4734.
[207] G. Ku, X. Wang, G. Stoica, L.V. Wang, Phys. Med. Biol. 49 (2004) 1329–1338.
[208] L.V. Wang, S. Hu, Science 335 (2012) 1458–1462.
[209] J. Zeng, M. Cheng, Y. Wang, L. Wen, L. Chen, Z. Li, Y. Wu, M. Gao, Z. Chai, Adv. Healthc. Mater. 5 (2016) 772–780.
[210] C. Sun, L. Wen, J. Zeng, Y. Wang, Q. Sun, L. Deng, C. Zhao, Z. Li, Biomaterials 91 (2016) 81–89.
[211] Z. Sun, Y. Zhao, Z. Li, H. Cui, Y. Zhou, W. Li, W. Tao, H. Zhang, H. Wang, P.K. Chu, X.-F. Yu, Small (2017) 1602896.
[212] W. Tao, X. Zhu, X. Yu, X. Zeng, Q. Xiao, X. Zhang, X. Ji, X. Wang, J. Shi, H. Zhang, L. Mei, Adv. Mater. 29 (2017).
[213] W. Chen, J. Ouyang, H. Liu, M. Chen, K. Zeng, J. Sheng, Z. Liu, Y. Han, L. Wang, J. Li, L. Deng, Y.N. Liu, S. Guo, Adv. Mater. 29 (2017) 1603864.
[214] D. Yang, G. Yang, P. Yang, R. Lv, S. Gai, C. Li, F. He, J. Lin, Adv. Funct. Mater. 27 (2017) 1700371.
[215] Q. Guo, A. Pospischil, M. Bhuiyan, H. Jiang, H. Tian, D. Farmer, B. Deng, C. Li, S.J. Han, H. Wang, Q. Xia, T.P. Ma, T. Mueller, F. Xia, Nano Lett. 16 (2016) 4648–4655.
[216] M. Engel, M. Steiner, P. Avouris, Nano Lett. 14 (2014) 6414–6417.
[217] M.Z. Rahman, C.W. Kwong, K. Daveya, S.Z. Qiao, Energy Environ. Sci 9 (2016) 709–728.
[218] X. Zhu, T. Zhang, Z. Sun, H. Chen, J. Guan, X. Chen, H. Ji, P. Du, S. Yang, Adv. Mater. (2017) 1605776.
[219] M. Zhu, X. Cai, M. Fujitsuka, J. Zhang, T. Majima, Angew. Chem. Int. Ed. 56 (2017) 2064–2068.
[220] J. Ran, B. Zhu, S.-Z. Qiao, Angew. Chem. Int. Ed. (2017), doi:http://dx.doi.org/10.1002/anie.201703827.

Dr. Ya Yi received her PhD in condensed matter physics from The Hong Kong University of Science and Technology in 2016. She is a postdoctoral fellow at the Shenzhen Institutes of Advanced Technology, Chinese Academy of Sciences. Her current research focuses on 2D semiconducting materials, nano-optoelectronic devices, and perovskite solar cells.

Dr. Wenhua Zhou received his PhD in biomedical research from Imperial College London, UK, in 2012 and is a research associate in the Shenzhen Institutes of Advanced Technology, Chinese Academy of Sciences. His current research interests are modification and biological applications of 2D nanomaterials.

Dr. Jia-Hong Wang received his PhD in Physics from Wuhan University, China in 2016 and is a postdoctoral fellow in the Shenzhen Institutes of Advanced Technology, Chinese Academy of Sciences. His research focuses on the fabrication of black phosphorus and corresponding nanocomposites.

Dr. Xuefeng Yu received his PhD in physics from Wuhan University, China in 2008. He is currently a Professor and Director of Center for Biomedical Materials and Interfaces at Shenzhen Institutes of Advanced Technology, Chinese Academy of Sciences. His research focuses on the synthesis, optical properties and biomedical applications of low-dimensional nanomaterials such as 2D black phosphorus, gold nanostructures, etc. He has coauthored more than 60 papers in SCI-indexed journals with over 2 000 citations.

Prof. Paul K Chu received his BS in mathematics from The Ohio State University in 1977 and MS and PhD in chemistry from Cornell University in 1979 and 1982, respectively. His research covers quite a broad scope, encompassing plasma surface engineering, materials science and engineering, as well as surface science. He is Chair Professor of Materials Engineering in the Department of Physics and Department of Materials Science and Engineering at City University of Hong Kong. He is Fellow of the APS, AVS, IEEE, MRS, HKAES, and HKIE and a highly cited researcher according to Thomson Reuters.